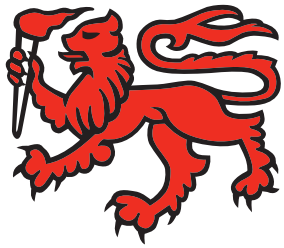

UNIVERSITY *of*
TASMANIA
AUSTRALIA

THIS PAGE INTENTIONALLY LEFT BLANK

Exoplanet Mass Measurement: Adaptive Optics Follow-up of Microlensing Events

By
Joshua William Blackman

B.A. / B.Sc. (Hons)
University of Adelaide, 2004

A Thesis submitted in partial fulfilment
of the requirements for the degree of
requirements for the degree of

Doctor of Philosophy
in the
School of Natural Sciences
at the
University of Tasmania
Hobart, Australia

Supervisors:

Associate Professor Andrew Cole
&
Professor Jean-Philippe Beaulieu

November 2020

Authority of Access

This thesis is not to be made available for loan or copying for one year following the date this statement was signed. Following that time, the thesis may be made available for loan and limited copying and communication in accordance with the Copyright Act 1968.

Signed:

Joshua William Blackman
Tuesday 17th November, 2020

Statement regarding Published Work contained in Thesis

The publishers of the papers comprising Chapters 3 to 5 hold the copyright for that content and access to the material should be sought from the respective journals. The remaining non published content of the thesis may be made available for loan and limited copying and communication in accordance with the Copyright Act 1968.

Signed:

Joshua William Blackman
Tuesday 17th November, 2020

Declaration of Originality

This thesis contains no material which has been accepted for a degree or diploma by the University or any other institution, except by way of background information and duly acknowledged in this thesis, and to the best of the my knowledge and belief no material previously published or written by another person except where due acknowledgment is made in the text of the thesis, nor does the thesis contain any material that infringes copyright.

Signed:

Joshua William Blackman
Tuesday 17th November, 2020

Statement of Co-Authorship

The following people and institutions contributed to the publication of work undertaken as part of this thesis:

Candidate: Joshua Blackman, School of Natural Sciences
Author 1: Jean-Philippe Beaulieu, UTAS / Institut d'Astrophysique de Paris
Author 2: Andrew Cole, University of Tasmania
Author 3: David P. Bennett, NASA Goddard
Author 4: Aikaterini Vandorou, University of Tasmania
Author 5: Camilla Danielski, Institut d'Astrophysique de Paris
Author 6: Clément Ranc, Institut d'Astrophysique de Paris
Author 7: Aparna Bhattacharya, NASA Goddard
Author 8: Etienne Bachelet, Las Cumbres Observatory
Author 9: Christophe Alard, Institut d'Astrophysique de Paris
Author 10: Naoki Koshimoto, NASA Goddard
Author 11: Jean-Baptiste Marquette, Laboratoire d'Astrophysique de Bordeaux / Institut d'Astrophysique de Paris

Contribution of work by co-authors for each paper:

Paper 1: Located in Chapter 3

Blackman, J. W.; Beaulieu, J.P., Cole, A.A.; Vandorou, A. et al. (2020), *Confirmation of the Stellar Binary Microlensing Event, Macho 97-BLG-28*, ApJ, 890:1

Candidate was the primary author and contributed 85% to the planning execution and preparation of the research project and subsequent paper.
Authors 1 and 2 advised on the methodology and critically assessed the paper before submission. Author 8 advised on the light curve modelling. Author 10 performed the Bayesian analysis shown in Figure 4.

Paper 2: Located in Chapter 4

Blackman, J. W.; Beaulieu, J.P., Cole, A.A.; Vandorou, A. et al. (2020), *Confirmation of the cold Super-Earth Planet in the microlensing event OGLE-2017-BLG-1434 using Keck Adaptive Optics* (to be submitted to the Astrophysical Journal)

Candidate was the primary author and contributed 90% to the planning execution and preparation of the research project and subsequent paper.
Authors 1 and 2 advised on the methodology and critically assessed the paper before submission. The candidate, author 1, 3, 4 and 7 partook in the observations at the Keck observatory.

Paper 3: Located in Chapter 5

Blackman, J. W.; Beaulieu, J.P., Bennett, D.P., Danielski, C. et al. (2020), *A Planetary Survivor of Its Host Star's Demise* (submitted to Nature)

Candidate was the primary author and contributed 80% to the planning execution and preparation of the research project and subsequent paper.
Authors 1, 2, 3 and 5 advised on the methodology and critically assessed the paper before submission. Author 6 calculated the lens prediction contours in Figure 1. Author 9 performed PSF fitting routines. The candidate, author 1, 3, and 7 partook in the observations at the Keck observatory.

We, the undersigned, endorse the above stated contribution of work undertaken for each of the published (or soon to be submitted) peer-reviewed manuscripts contributing to this thesis:

Signed: _____ Date: 19/5/2020

Joshua Blackman
Candidate
School of Natural Sciences
University of Tasmania

Signed: _____ Date: 19/5/2020

Associate Professor Andrew Cole
Primary Supervisor
School of Natural Sciences
University of Tasmania

Signed: _____ Date: 21/5/2020

Professor Simon Ellingsen
Head of School
School of Natural Sciences
University of Tasmania

Exoplanet Mass Measurement: Adaptive Optics Follow-up of Microlensing Events

Abstract

Microlensing is a powerful tool that can be used to search for cold exoplanets in the disk and bulge of the Milky Way. Over the past 16 years ~100 planets have been discovered using this method, but moving from modelled parameters to physical properties is difficult. I refine and apply a method of using high-angular resolution near-infrared observations from large ground based observatories to find more precise constraints on the mass and distances of these exoplanets and their stellar hosts.

Microlensing events rely on the chance alignment of source and lens stars along our line of sight towards dense star fields, usually the galactic bulge at the centre of our galaxy. The relative proper motion of these two stars is such that adaptive optics (AO) observations on 8-10m class telescopes can be used measure the lens flux, or even entirely resolve them when observed at later epochs. In this thesis I present three studies of microlensing events augmented with AO photometry obtained from the Keck observatory.

The first is a reanalysis of the microlensing event MACHO-97-BLG-28. Suspected to be a case where the source and lens stars could be resolved with photometry from Keck, I showed it was not. I revise estimates of the lens mass and distance by re-modelling the event light curve using additional data from the Mt. Stromlo 74" telescope, model estimates of stellar limb darkening, and fitting of the blend separately for each telescope and passband. This slightly favours the conclusion that the event is a stellar M-dwarf binary.

I then use Keck photometry to constrain the mass-distance of OGLE-2017-BLG-

1434, which is a cold super-Earth planet and the eighth microlensing planet discovered with a planet-host star mass ratio $q < 1 \times 10^{-4}$. This planet confirms the turnover in the cold-planet mass ratio function. I obtained 60 mas images of the event and by comparing measured near-IR magnitudes with the predicted source magnitude from the light curve model we reduce the error in the lens mass and distances by more than 50%. This confirms the event as a close super-Earth at a distance of $860 \pm 50\,\mathrm{pc}$.

Finally, I present the first detection of a white dwarf hosting a gas giant planet. This detection was made in event MOA-2010-BLG-477 using Keck H-band images taken at two epochs after the time of maximum magnification when the proper motion was such that the lens and source should be resolved. A non-detection of a main-sequence lens well above the detection limit of the Keck photometry indicates the event to be a 0.58 solar mass white dwarf orbited by a 1.3 Jupiter mass planet.

These three studies contribute to the measurement of the cold planet mass function. The super-Earth OGLE-2017-BLG-1434 lies near the break of this function, while MOA-2010-BLG-477 is the first solid detection of a single white dwarf with a planetary companion. These studies and the methods herein are a pathfinder for the Nancy Grace Roman Space Telescope and the mass measurement method which will be used for 80%+ of the microlensing targets it will observe.

Contents

List of Figures and Tables

Acknowledgments

This thesis is 15 years in the making.

When I started a PhD in astronomy back in 2005, I certainly do not predict I would be submitting an entirely different thesis, on a different topic, in Tasmania, more than a decade later. And yet I'm glad it's happened this way. Thanks to all the people I've met during my travels these past few years have been a joy – tricky, weird and at times frustrating – but a joy nonetheless.

Firstly I must thank my supervisors Andrew Cole and JP Beaulieu for their guidance, good humour, overseas adventures and their vast wealth of knowledge. I am not quite sure what possessed Andrew and the selection committee to accept a 33 year old who had not done physics for 10 years into their program, but I'm glad they did as my project ended up being a perfect fit for my my science interests. Also the connections I have made with a good proportion of the microlensing community, thanks in no small part to JP's encouragement and connections, should place me in good stead for the future.

Thank you to the huge list of people who I have met and talked science with at various conferences and observing runs, including but not limited to Etienne, Geoff, Clément, Dave, Aparna, Naoki, Matthew P., Yiannis, Markus, Lukasz, Radek and Martin D. Also

the younger generation for their friendship, PhD commiserations and New Zealand and New York adventures and shenanigans including but not limited to Kasia, Calen, Maria & Amber.

Thanks to my parents for their support, and thanks to Camilla for being awesome and fun and making my stay at IAP and working on 477 more enjoyable. And finally thankyou to the UTAS crew for your friendship, game nights, gossip and general good times. In particular Katie for endless chat, moral support, Parisian adventures and for being a partner in crime in this crazy exoplanet adventure, but also Eloise, Jonny, Gabor, Patrice, Lucas, Tiege, Andy and the rest of the Coffee Club™. I love you all, and this thesis would not have happened without you.

Finally I thank my now dearly departed cat, Athena, because JP said I could.

1

Introduction

The study of exoplanets is one of the most exciting topics in science. While the existence of planets outside our solar system has been long suspected, it was not until the seminal discovery of two super-Earth planets around the millisecond pulsar PSR1257+12 that one had been found orbiting a stellar body other than our Sun (Wolszczan & Frail 1992). Since then there has been an explosion in the number of planets found, with over 4,000 planets confirmed as of May 2020[1]. Even though only ~10% of the planets found

[1] NASA Exoplanet Archive, https://exoplanetarchive.ipac.caltech.edu

are terrestrial-sized, the prospect of finding Earth-like planets in the habitable zone of other stars has generated substantial attention from the media and the general public.

As the number of planets detected has grown, so has our understanding of their demographics and mechanisms of their formation. Up until the dawn of the exoplanet era, our knowledge of solar system formation was based on a sample size of one: our own (Lissauer 1995). The prevailing theory of planet formation that came to be accepted was a "bottom-up" scenario in which micron-sized ice and dust grains left over from star-formation processes condense and coagulate in a cooling protoplanetary disk. These clumps of matter eventually reach the size of 0.01-100 km planetesimals, with a composition that depends on their distance from the host star. At small distances the hot gas tends to facilitate the condensation of elements such as silicon and magnesium, leading to the formation of rocky cores such as those of our terrestrial planets, while at the snow-line and beyond – the distance from a host star at which ice forms ($\sim$2.7 AU for a solar mass star) – there is a sharp increase in the surface density of solid particles (Kennedy & Kenyon 2008). The abundance of Helium and Hydrogen and the long formation timescales available at these larger distances facilitates the forming of the gas giants (D'Angelo et al. 2014).

This is what has come to be known as the core-accretion theory of planet formation and conveniently accounts for the formation of the four terrestrial planets and four gas giants of our own solar system (Safronov 1972; Lissauer 1993; Pollack et al. 1996). Unfortunately, not all detected planetary systems have the same demographics as our own; in fact, beginning with the "Hot Jupiter" orbiting 51 Peg at 0.05 AU, most do not (Fischer & Valenti 2005; Santos et al. 2004). Concepts such as migration, where large planets form at wide orbits and transition inwards, are now included in the models to better explain this diversity (Ida & Lin 2004). Competing theories such as disk instability (Cameron 1978; Boss 1997), which describes the breakdown of the protoplanetary disk into clumps due to its own gravity, have also emerged. Even then there are some massive planets at large

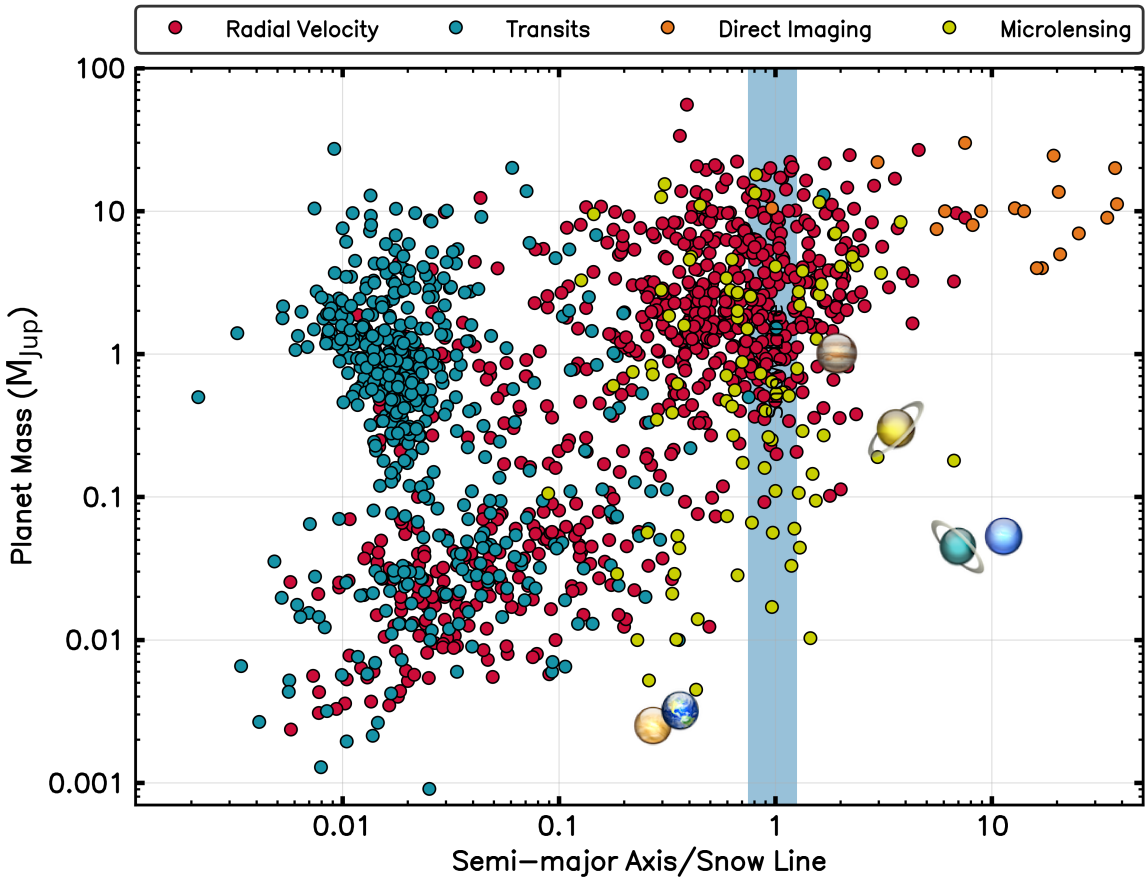

Figure 1.1: Detected Exoplanets as of May 25, 2020, with semi-major axis normalized to the snow line. The distribution of exoplanets discovered with four different detection methods (radial velocity, transits, direct imaging and microlensing) with respect to the snow line ($a_{snow} = 2.7AU(M/M_{sun})$, Kennedy & Kenyon (2008)). The location of the solar system planets down to the mass of Venus are marked. Note that microlensing (in yellow) is the method most able to probe the region near the snow line for Neptune - Earth masses. Data used in this plot are sourced from the NASA Exoplanet Archive.

radii that are incompatible with either model (Dodson-Robinson et al. 2009). Despite the strong continued work by theorists in the field, then, our understanding of planetary formation in the exoplanet era is at best incomplete. One way to improve these models is to observationally evaluate the distribution of exoplanets over as wide a range of properties (eg. mass and semi-major axes) as possible, and the method that is most sensitive to the region critical to planet formation is microlensing (see Fig. 4.1).

Gravitational microlensing is one of the major exoplanet detection methods and is sensitive to an area of host separation vs. planet mass parameter space mostly not accessible by

any other method. The other exoplanet detection methods include radial velocity, which relies on the Doppler "wobble" of the planet's stellar host due to the change in gravitational pull due to the planets orbit, and transits, which rely on the minuscule dip in brightness in the source star when the exoplanet passes in front of its host star. The first detection using transits was made in HD 209458 at the end of the 1990s (Charbonneau et al. 2000) and one advantage of this method is knowledge can be gained about its molecular composition because the detected light passes through the exoplanet atmosphere (Swain et al. 2008; Tinetti et al. 2010). The Kepler spacecraft has since yielded an enormous variety of over 2300 planetary systems detected using this method, and this continued even when the instrument moved into its second phase of operation ("K2") after the failure of two of the four gyroscopes in mid 2013.

Both the radial velocity and transit detection methods, however, necessarily rely on the light from the host star. The microlensing technique, originally intended to be used to search for Massive Compact Halo Objects (MACHOs), was also used to search for exoplanets around microlensed stars from the late 1990s. Relying on the chance alignment of two stars, denoted the "source" and "lens", the likelihood of one star being microlensed in a year is of the order of 2×10^{-6} (Peale 1998; Sumi et al. 2013; Mróz et al. 2019), and hence many stars need to be observed to get a usable quota of detections[2]. Microlensing surveys such as OGLE (the Optical Gravitational Lensing Experiment, Udalski (2003)) and MOA (Microlensing Observations in Astrophysics, Sako et al. (2008)) hence focus on the the dense star fields of the Milky Way galactic bulge. Since microlensing does not rely on flux from the host star, it means it is theoretically possible to use the technique to detect stars around dark stellar remnants such as black holes and white dwarfs (see Chapter 5).

As of mid-2020 around 100 planets have been detected using microlensing[3]. Though

[2] Estimates of the microlensing optical depth towards the galactic bulge vary between $0.2 - 4.0 \times 10^{-6}$ and depend on density distribution of the field.

[3] NASA Exoplanet Archive, https://exoplanetarchive.ipac.caltech.edu

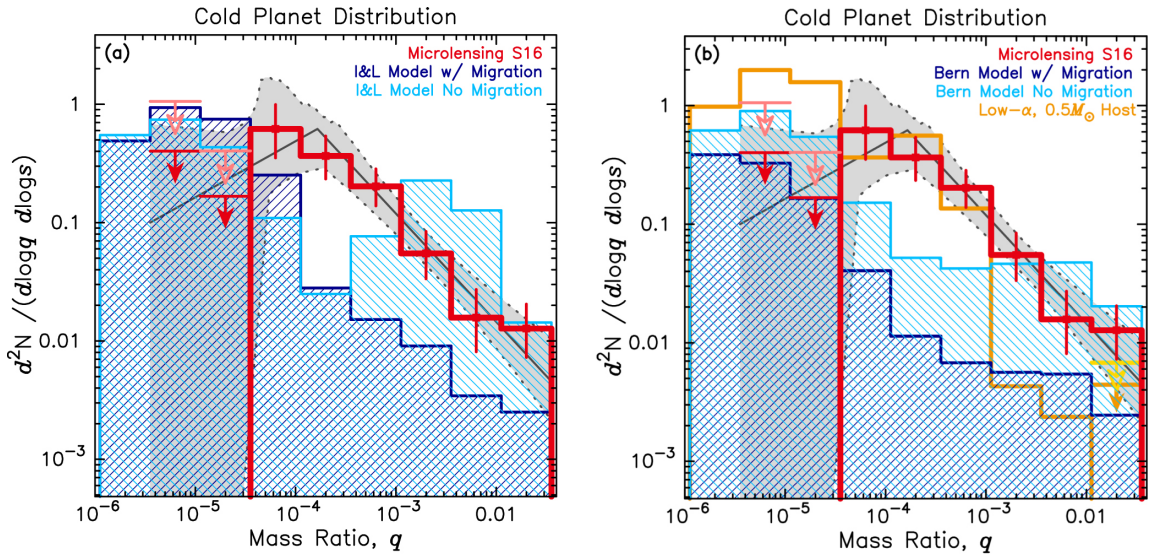

Figure 1.2: Comparing microlensing observations with mass-ratio predictions from core accretion theory Comparing predictions from two core-accretion models, with and without migration (on the left **(a)** Ida & Lin (2004), and on the right **(b)** Mordasini et al. (2009)) compared with a observed microlensing sample of planets in red. The best fit broken-power from the observations is shown in black with the 1σ region noted by the gray shaded region. Note that between the mass ratio of $\sim 10^{-4}$ and $\sim 10^{-3}$ that the theory underpredicts the observations by a factor of $\sim$10. [Figure from Suzuki et al. (2018)]

an order of magnitude fewer than those detected by either radial velocity or transits, planetary measurements from microlensing are particularly relevant for accounting for the dearth of planets in-between the masses of Neptune and Saturn due to the runaway gas accretion of hydrogen and helium onto bodies that reach masses of $\sim 10 M_\oplus$ (Ida & Lin 2004; Mordasini et al. 2009). While consistent with the prediction that ice giants should be more common than Jupiters, this is in conflict with planetary observations from microlensing which shows that core accretion underpredicts the number of planets by a ratio of $\sim$10 (Suzuki et al. 2016, 2018), Fig. 1.2. The mass-ratio function of planets below the snow line rises steeply towards lower masses before a strong break in the mass function at $q = 1.7 \times 10^{-4}$ (Suzuki et al. 2016) or $q = 0.55 \times 10^{-4}$ (Jung et al. 2019). The uncertainty in this value and conflict between these two studies is reflective of the slim statistics in this region: there are simply not enough planets in this sample to firmly characterize this break.

Together with a more complete sample, a major advance in our understanding will

come when we can describe this distribution in terms of planet masses, rather than planet-host mass-ratio. This is in no way a trivial task. A major limitation in achieving this is that transitioning form fitted microlensing light curve parameters to physical properties can be difficult. While we can determine the planet-host mass ratio, q, and the projected separation, s, in units of Einstein Radius, θ_E, with an accuracy of 5-10%, additional constraints are needed to determine physical properties such as mass and distance. This includes determining the angular size of the source, measuring parallax, or by obtaining high-angular resolution images of the event at later epochs in order to constrain the flux of the lens star and/or the relative lens-source proper motion. It is this latter technique that is the focus of this thesis.

Data has so far been obtained with the largest ground-based telescopes (Keck, Subaru, VLT, Magellan) and the Hubble Space Telescope (HST) on about 60 planetary microlensing events in an effort to constrain microlensing host and planet mass and distance. An overview of these studies and the theory behind them can be found in Chapter 2. In this thesis I present three studies of microlensing events augmented with data from the twin 10m Keck telescopes on Mauna Kea, Hawaii. Two of these contain data obtained as part of NASA Key Strategic Mission Support (KSMS) Keck proposal in support of the flagship Nancy Grace Roman Space Telescopes (or Roman Space Telescope, previously referred to as WFIRST - Wide-Field Infrared Survey Telescope) mission, which is scheduled to be launched in the mid 2020s. Designed to determine a method of finding accurate exoplanet masses ahead of the huge increase in microlensing detections that will come with RST, developing such a technique will be critical to our understanding of cold planet statistics and planet formation.

1.1 Thesis Structure

In Chapter 2 I introduce microlensing and review the method of obtaining high-angular resolution follow-up of microlensing events using the 10m Keck telescopes. I describe the selection of events and methods of data reduction, including a Python-centred pipeline led to process these raw telescope images. Finally I discuss current results from this program.

Chapter 3 is presented as the published paper in its original format, while 4 and 5 have been reformatted from their (soon to be) submitted versions. Details of author contributions and the studies' place in the broader context of this thesis are presented in the preface to each chapter. Chapter 3 concerns the stellar binary microlensing event MACHO-97-BLG-28, which I remodel using `PyLIMA` with additional data from the Mt. Stromlo 74" telescope, updated model estimates of stellar limb darkening, and blend fitting. My modelling slightly favours the conclusion that the event is a stellar M-dwarf binary. This paper was published in the Astrophysical Journal on February 10, 2020.

Chapter 4 concerns the super Earth event OGLE-2017-BLG-1434 which confirms the turnover in the cold-planet mass ratio function. Data was obtained from the Keck telescopes in 2019 and I show how this data was used to place constraints on the lens flux. This result was in agreement with the original study. I predict this event to be a close super-Earth at a distance of $860 \pm 50\,\mathrm{pc}$. This manuscript will shortly be submitted to the Astrophysical Journal.

Finally, Chapter 5 presents a study of a gas giant planet orbiting a stellar remnant, most likely a white dwarf. Using detection limit constraints of Keck photometry using the NIRC2 imager, as well as constraints from parallax and the object light curve, I show that this 1.3 Jupiter mass planet cannot have a main sequence host. It is instead most likely a white dwarf of 0.58 solar masses. This is the first such detection of a planet around a single white dwarf. This manuscript has been submitted to Nature. All of these results make use of AO data obtained from Keck in the period 2013-2019.

2

Adaptive Optics Follow-up of Microlensing Events

In this chapter I present background information on microlensing and the techniques used in the publications presented in this thesis. This includes the methods used to find mass-distance constraints on the lens stars (and hence their potential planetary companion), the rationale behind our Keck Key Strategic Mission Support proposal to follow-up microlensing events with adaptive optics photometry, and an overview of results from this program. Chapter 4 and 5 rely on data obtained in 2018 as a result of this proposal. Chap-

ter 3 also relies on Keck data, however this was taken from a previous observing campaign in 2013.

2.1 Microlensing

A gravitational lensing event occurs when the light from a background object, which can be anything from an entire galaxy cluster down to a single star, is bent by the gravity of foreground object. Microlensing is a subset of this phenomena that occurs with objects of sufficiently small mass that the lensing effect is visible on the order milliarcseconds, which means these events are unresolvable with current telescopes. Instead, we observe a combined 'blend' flux of the background source and foreground lens, together with other potential contaminant stars, as a single object that increases in magnification as the source and lens become more aligned. A rare and transient phenomenon that relies on the chance alignment of these bodies (Figure 2.1), microlensing events are observable as a time-varying magnification in brightness which results in light curves extending over typical event timescales of 20-80 days. Computationally demanding models are used to fit the data and hence decode the geometry and mass ratio of the lens systems, with second order factors such as parallax, finite source effects and measurements of the lens flux and relative proper motion, required to place constraints on the physical parameters of the lens system.

Our understanding of the microlensing phenomena has its theoretical roots in the work of Albert Einstein in the early 20th century. Einstein had considered the idea of gravitational lensing as early as 1912, three years before the publication of his General Theory of Relativity, but it wasn't until 1936 that he would publish on the subject (Einstein 1936). This was thanks to the encouragement of a Czech electrical engineer named Rudi W. Mandel, who was working as a busboy and dish-hand at the time, and wrote to Einstein repeatedly on the subject Renn (1997). Einstein's reluctance was born from the precise alignment

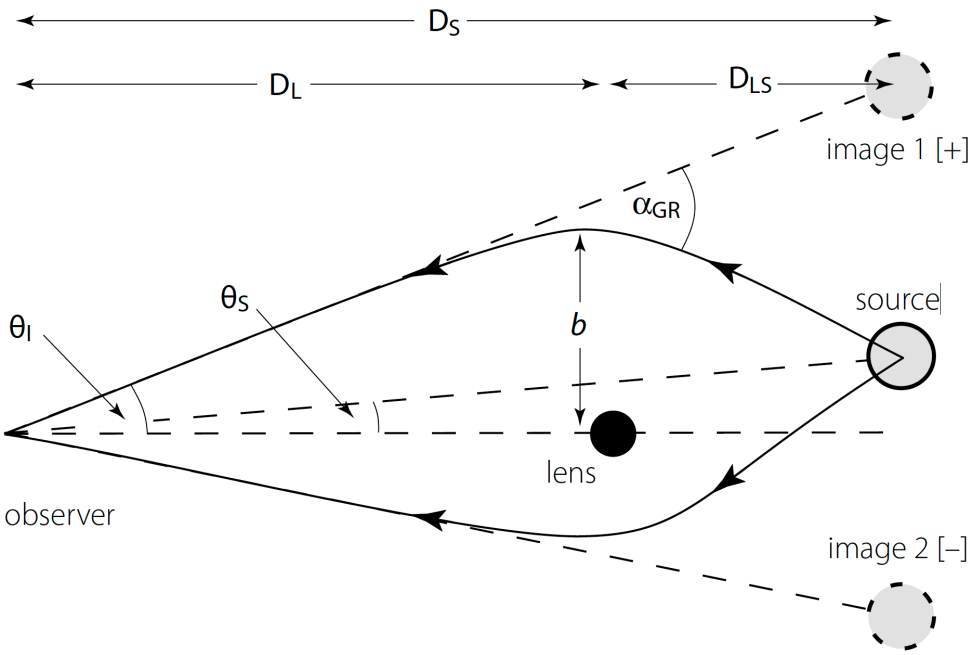

Figure 2.1: Microlensing Geometry. The light from a source at distance D_S is deflected by a lens at distance D_L and the resulting two images are displaced by $\theta_I = b/D_L$. From the observers perspective both images are blended on milliarcsecond scales and are seen as a single object. The light from source is magnified as a result over the course of the microlensing event [Figure from Perryman (2011)].

needed to observe the phenomena, and also an awareness of the milliarcsecond span of the event's angular radius. He would famously state that "there is no great chance of observing this phenomenon," and on that score he was correct, at least for the next 50 years.

Though there were sporadic investigations into microlensing following Einstein's letter (Liebes 1964; Refsdal & Bondi 1964), it wasn't until Paczyński's seminal search of the Large and Small Magellanic Clouds for dark matter MACHOs (MAssive Compact Halo Objects) that the practical application of the technique was realised (Paczyński 1986). Paczyński's premise was to see if the light from distant stars was magnified (or 'lensed') by these dark matter candidates. More recent observations have indicated that MACHOs are not a significant contributor to dark matter (Tisserand et al. 2007) but Paczyński's work was the watershed led to the detection of thousands of microlensing events in the following two decades. Notable studies of this period include those on the dark matter content of the

Milky Way (Alcock et al. 1996) and the distribution of mass towards the Galactic Bulge (Alcock et al. 1997; Udalski et al. 1994). To probe the dark matter halo, observations were directed towards the Small and Large Magellanic Clouds (Alcock et al. 1997) and some towards M31 (De Jong et al. 2003; Uglesich et al. 2004). Today the last window to baryonic dark matter could be from massive primordial black holes which formed shortly after the Big Bang. Adaptive optics observations and the mass measurement method described in this thesis could be used to probe such black hole candidates detected by microlensing.

The idea of looking for planetary companions around lens stars was described by Mao & Paczyński (1991). They described the characteristic light curves that can result when the lens/source separation was similar to the Einstein ring, which is the angular radius of the event when the source and lens are in perfect alignment. They estimated that planets may be detectable in 5-10% of microlensing events, which equates to "about two events per year per 10^7 Galactic bulge stars" (Mao & Paczyński 1991). The practical requirements for such surveys would in turn be described in Gould & Loeb (1992). They proposed a single survey telescope directed towards the Galactic bulge which could scan and alert observers of in-progress events. These events would then be followed-up using network of smaller telescopes with a cadence sufficient to detect the short-lived planetary perturbations in the light curves, of the order of 3-5 hours for an Earth sized planet and 1 day for a Jupiter mass planet. Though the technique of analyzing microlensing events has undergone much refinement since, this two-stage process is still the standard observational methodology in use today, though there is a move towards an all-in-one model such as the KMTNet survey (Korean Microlensing Telescope Network, Shin et al. (2016); Kim et al. (2016)) and the Roman Space Telescope (RST), NASA's planned Wide Field Infrared Survey Telescope satellite observatory (Spergel et al. 2015). It's the preparation for RST, scheduled for launch in the mid 2020s, that has facilitated the high-resolution follow-up observations used in this thesis.

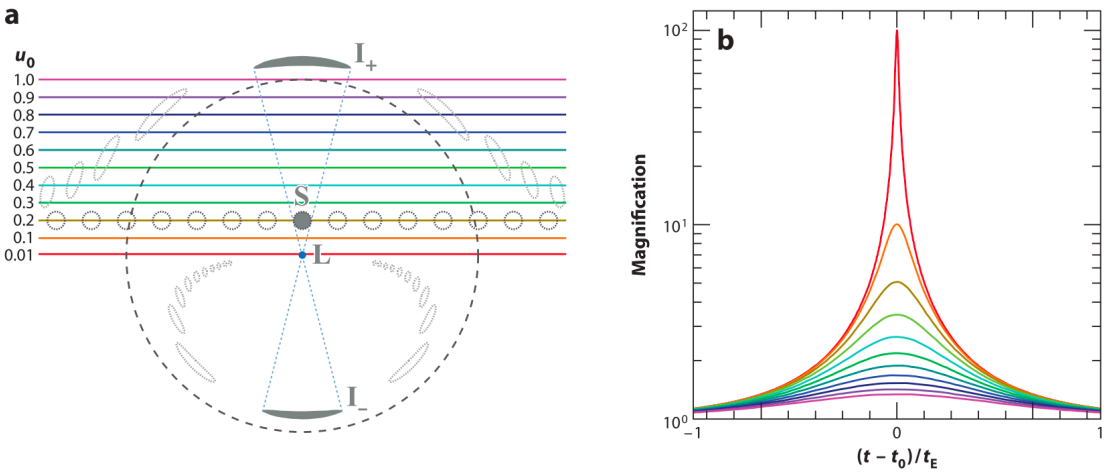

Figure 2.2: Magnification of a microlensing event with a varying impact parameter, u_0. (a) Example trajectories with ten different values for u_0. The dotted circle represents the Einstein Ring Radius, θ_E. The grey elongated circles on the inner and the outer of the Einstein ring represented the minor and major images, respectively, according to a source trajectory where $u_0 = 0.2$. As is custom in microlensing schematic representation, the source is represented as moving while the lens is stationary in the centre of the circle. **(b)** Magnification for the ten color-coded trajectories in panel (a). Time is shown relative to the point of maximum magnification and is described with respect to the characteristic timescale, t_E [Figure from Gaudi (2012); Paczyński (1996)].

2.1.1 Microlensing Basics

While the underlying physics of microlensing is based on general relativity, the complex differential geometry required to mathematically describe it is usually not required thanks to some applicable assumptions. The mathematics required can be reduced to algebra and trigonometry, which greatly simplifies its theoretical formalism for the most simple case of a point source, point lens. In this section I will describe some of the basis of microlensing as it pertains to practical analysis of light curves and adaptive-optics follow-up. For a more detailed look at the mathematical formulation of microlensing one can look at recent reviews on the subject such as Gaudi (2010) and Tsapras (2018), or physics text such as Schneider (1992).

In the simplest scenario one can consider a microlensing event containing a "point source point lens" (PSPL), where the lens is a single star and the finite size of the source is

ignored. In this instance there are three quantities needed to describe a microlensing event due to a single isolated lens. They are:

1. t_0, the time of maximum magnification
2. u_0, the impact parameter of the event at the time of maximum magnification (in units of Einstein ring radius), and
3. t_E, the Einstein timescale (time to cross the angular Einstein Ring Radius, θ_E)

The time of maximum magnification, t_0 can be seen in both the schematic in Figure 2.2 and the light curve from the microlensing event MOA-2010-BLG-477 (where MOA is the survey campaign, 2010 is the year of detection, BLG referring to its detection in the galactic bulge, and 477 the event number for that year) in Figure 2.3. The trajectory, in terms of the projected distance between the lens and source, is given by the impact parameter, u_0, and is defined in units of Einstein Ring Radius, θ_E (Figure 2.2). The Einstein Ring Radius θ_E is the characteristic length scale used to describe microlensing events, and is indicated in Figure 2.2 by the dotted circle. If the point source and point lens were perfectly aligned with an impact parameter $u_0 = 0$, the two images produced from the lensing event would be located on this circle. The majority of the time, however, there is some deviation from this PSPL case. To mathematically describe a microlensing event we use the thin lens approximation (valid because the distances to the lens and source are large compared to the path over which light from the source experiences lateral acceleration due to the lens) and the small-angle approximation. Doing so we can write what is commonly referred to the lens equation as:

$$\theta_S = \theta_I - \frac{D_{LS}}{D_S D_L} \frac{4GM_L}{c^2 \theta_I} \tag{2.1}$$

where D_{LS} is the distance between the lens and the source, D_S the distance to the lens, D_L the distances to the lens, θ_S is the angular position of the source, and θ_I is the angular

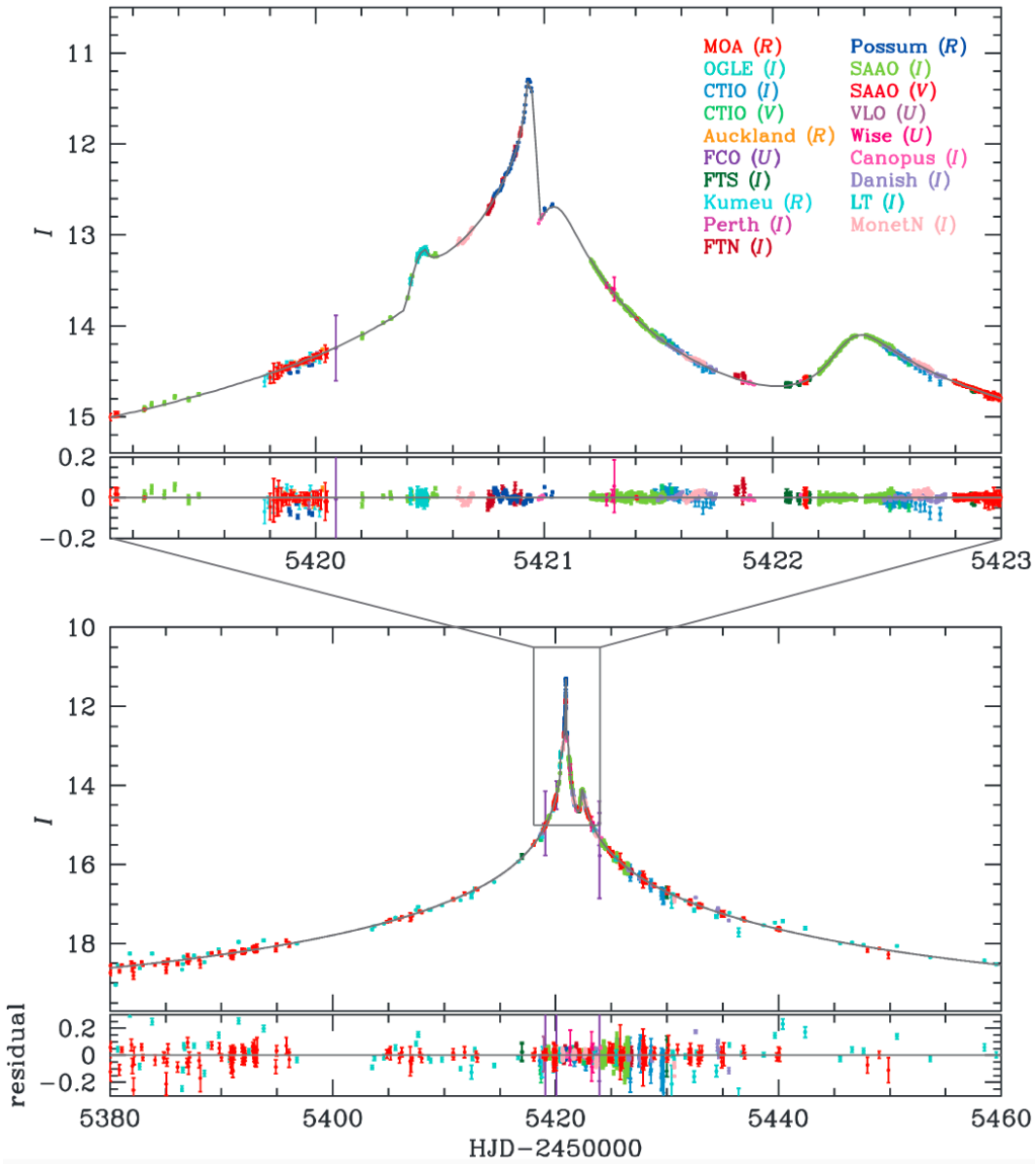

Figure 2.3: MOA-2010-BLG-477 Light Curve showing the sharp light curve features as a result of caustic crossings in a binary microlensing event. This light curve is the result of a binary microlensing event comprised of a Jupiter-mass planet and its white dwarf companion (see Chapter 5). The perturbations in the light curve are the result of the source trajectory across a *resonant* caustic (see Figure 2.4), which is comprised of a single closed curve and six cusp features (Bachelet et al. 2012). Note the contribution from the Optical Gravitational Lensing Experiment (OGLE) and Microlensing Observations in Astrophysics (MOA) survey telescopes together with high-cadence follow-up from other sites.

position of the lens, as in Figure 2.1. Using the definition of the Schwarzschild radius of the lens, $R_{Sch} \equiv 2GM/c^2$, an expression for the Einstein Ring Radius, $\theta_E = \sqrt{2R_{Sch}/D_{rel}}$ where $D_{rel} = D_{LS}/D_s D_L$, and defining $u = \theta_S/\theta_E$ and $y = \theta_I/\theta_E$, we can normalize the lens equation by θ_E and rewrite it to a form equivalent to the quadratic $y^2 - uy - 1 = 0$:

$$u = y - y^{-1} \tag{2.2}$$

This can hence be solved for the two solutions which describe the two images produced in the lensing event. The positive solution is always located outside the Einstein ring radius, while the negative solution is always located on the inside:

$$y_\pm = \frac{1}{2}\left(u \pm \sqrt{u^2+4}\right) \tag{2.3}$$

To describe the magnification of the images, which is simply the area of image compared to the area of the source, we define a polar coordinate system with the lens at the centre. Consider light from the source passing through an area element $dA = u\Delta\phi\Delta u$. Due to lensing this light will be projected onto an area $dA' = y\Delta\phi\Delta y$. The magnification of this images will hence be the ratio of these two areas:

$$A_\pm = \left|\frac{y_\pm \Delta\phi \Delta y_\pm}{u\Delta\phi\Delta u}\right| = \left|\frac{y_\pm}{u}\frac{dy_\pm}{du}\right| \tag{2.4}$$

where

$$\frac{dy_\pm}{du} = \frac{1}{2}\left(1 \pm \frac{u}{\sqrt{u^2+4}}\right) \tag{2.5}$$

From this we can define the total magnification, $A(u)$ of a microlensing event as:

$$A(u) = \frac{u^2+2}{u\sqrt{u^2+4}} \tag{2.6}$$

The magnification is a time variant quantity as a result of the relative motion of the source, lens and observer, and its this that results in the light curve such as in Figure 2.3. The magnification itself can influence the choice of which microlensing event to observe. High magnification microlensing events where $A_{max} > 100$ are rare but have almost complete sensitivity to planets which pass near the Einstein Ring (Griest & Safizadeh 1998). These events have the practical advantage that peak magnification can be predicted hours or days ahead of time, which means maximum observing resources can be directed to dense sampling of the peak and achieving a greater likelihood of detecting planetary perturbations. As such, observing tactics have skewed towards most longitudinally separated telescope facilities concentrating on dense sampling of high magnification events.

To begin to characterize the lens star, we can rewrite Equation 2.1 by setting $\theta_S = 0$ for when the source lies on the optical axis. This gives an expression for the Einstein Ring Radius, θ_E:

$$\theta_E = \sqrt{\frac{D_{LS}}{D_S D_L} \frac{4GM_L}{c^2}} \tag{2.7}$$

In the lens plane we can write this as:

$$R_E = \theta_E D_L = \sqrt{\frac{D_L D_{LS}}{D_S} \frac{4GM_L}{c^2}} \tag{2.8}$$

Since we assume a source distance of 8kpc, which is the distance to the bulge on the near side of the Galactic centre, this can be rewritten in a useful format:

$$\theta_E = 1.01 \text{ mas} \left(\frac{M_L}{M_\odot}\right)^{\frac{1}{2}} \left(\frac{D_L}{8 \text{ kpc}}\right)^{-\frac{1}{2}} \left(\frac{D_{LS}}{D_S}\right)^{\frac{1}{2}} \tag{2.9}$$

Similarly, we can also define the characteristic timescale of a microlensing event, t_E:

$$t_E = 1.01 \text{ yr} \left(\frac{M_L}{M_\odot}\right)^{\frac{1}{2}} \left(\frac{D_L}{8 \text{ kpc}}\right)^{-\frac{1}{2}} \left(\frac{D_{LS}}{D_S}\right)^{\frac{1}{2}} \left(\frac{1 \text{ mas } yr^{-1}}{\mu_{rel}}\right) \tag{2.10}$$

Binary Events

For binary lens events, which is the case where the lens is accompanied by another body, it is useful to consider the mapping of the magnification onto the source plane. This results in a set of divergence points called "caustics" where the magnification theoretically reaches infinity (Figure 2.4). These critical curves are fundamental to describing the magnification map of two or more microlensed bodies. The positions of the caustics are sensitive to both the mass ratio, q and the angular separation s, with the three topologies: wide, intermediate/resonant and close, shown in Figure 2.4. When the source trajectory crosses the caustics there are sharp changes in magnification (such as in the light curve for in Figure 2.3), which can make fitting of the light curve less ambiguous. It's this morphology of the light curve which indicates whether or not the event is a stellar binary (for example) or a planetary event.

There are there are three further quantities needed to describe the microlensing light curve for binary events in addition to t_0, u_0 and t_E. They are:

4. s, the projected binary separation (in units of θ_E)

5. q, the planet/star mass ratio, and

6. θ_S, the angle between the source trajectory and binary axis (see Figure 2.1)

To derive the theoretical formalism of such systems we consider the case of N point mass lenses (of which a binary event is the specific case where $N = 2$), and write the lens equation as

$$\boldsymbol{u} = \boldsymbol{y} - \sum_{i}^{N_l} \epsilon_i \frac{y - y_{m,i}}{|y - y_{m,i}|^2} \tag{2.11}$$

where $\boldsymbol{u} \equiv \boldsymbol{\beta}/\theta_{\mathbf{E}}$ is a dimensionless vector of the source position, $\boldsymbol{y} \equiv \theta/\theta_{\mathbf{E}}$ the dimensionless vector of the image position, $\boldsymbol{y}_{m,i}$ the position of lens mass i and $\epsilon_i \equiv m_i/M_{\rm tot}$ (Witt 1990; Gaudi 2012). This equation allows us to find the point of the source plane, $\boldsymbol{u}$, which

corresponds to the light ray incident on the lens plane, $\boldsymbol{y}$ (Tsapras 2018). It can be useful, however, to write this equation in complex co-ordinates (Witt 1990):

$$\zeta = z - \sum_{i}^{N_l} \frac{\epsilon_i}{\bar{z} - \bar{z}_{m,i}} \tag{2.12}$$

where the complex source and image positions are given by $\zeta = u_1 + iu_2$ and $z = y_1 + iy_2$. The determinant of the Jacobian of this relation is given by:

$$\det J = 1 - \frac{\partial \zeta}{\partial \bar{z}} \frac{\overline{\partial \zeta}}{\partial \bar{z}}, \frac{\partial \zeta}{\partial \tilde{z}} = \sum_{i}^{N_l} \frac{\epsilon_i}{\left(\bar{z} - \bar{z}_{m,i}\right)^2} \tag{2.13}$$

while the magnification, as in the single lens case, can be calculated using the Jacobian of the lens equation evaluated at image position j:

$$A_j = \left. \frac{1}{\det J} \right|_{\theta=\theta_j}, \quad \det J \equiv \left| \frac{\partial \left(\beta_1, \beta_2\right)}{\partial \left(\theta_1, \theta_2\right)} \right| \tag{2.14}$$

The path of the caustics can be calculated by determining the image positions where $\det J = 0$, which occurs when:

$$\left| \sum_{i}^{N_l} \frac{\epsilon_i}{\left(\bar{z} - \bar{z}_{w,i}\right)^2} \right|^2 = 1 \tag{2.15}$$

Solving the following for each value of $\phi = [0, 2\pi)$ (Witt 1990) will give the values of the critical curves:

$$\sum_{i}^{N_i} \frac{\epsilon_i}{\left(\bar{z} - \bar{z}_{m,i}\right)^2} = e^{i\phi} \tag{2.16}$$

Finding the source positions where $\det J = 0$ will hence determine the location of the caustics, such as those shown in Figure. 2.4. These closed curve caustics feature multiple concave folds that meet at sharp "cusps". Theoretically the magnification along caustics is infinite, though extended sources means that in reality it is always finite. The shape of the resulting light curve is depending on the trajectory of the source relative to these critical

curves. The fitting of the light curve then gives rise to the fitted light curve parameters.

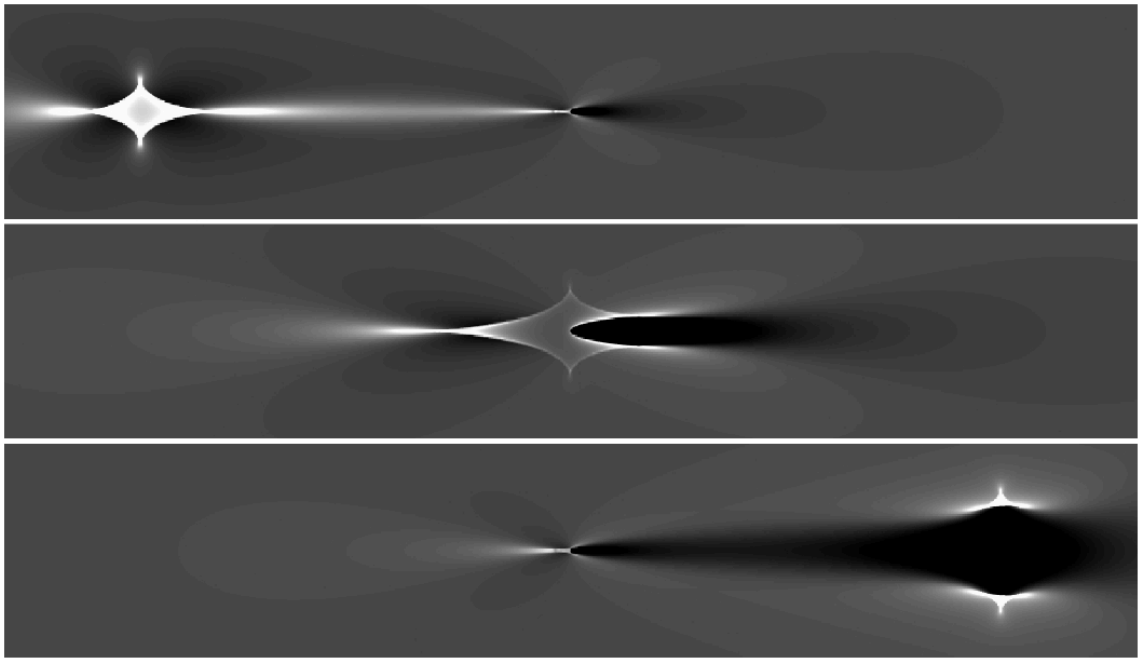

Figure 2.4: Magnification map for a planetary microlensing event as a function of source position. Example magnification map for a microlensing map indicating the three possible topologies: wide with s = 1.25 (top panel), intermediate/resonant with s = 1.0 (middle panel), and close with s = 0.8 (bottom panel). In all cases the mass ratio is q=0.0001. The white and black areas denote positive and negative deviation from the point source point lens (PSPL) magnification, respectively [Image from Gaudi (2012)].

2.2 Mass-Distance Relations

If we are to determine the mass and distance of a lens star in a microlensing event from the fitted light curve parameters we might use a Bayesian analysis with priors from a model of the Milky Way galaxy such as Sumi et al. (2011) as discussed in Bennett et al. (2014). Such a process can usually achieve an accuracy of 30-40%. Using additional constraints as described in the next section, however, we can restrict this to 5-10%. The three mass-distance relations I use in this thesis in order to place constraints on the mass and distance of the microlensing lens star and its companion(s) are described below.

2.2.1 Finite Size of the Source

The Point-Source approximation breaks down when the size of the planetary perturbation becomes significant compared to the angular size of the source, ie. when $\theta_E \sim \theta_*$, or when $u_0 \lesssim 3\rho$ where ρ is the normalised source radius. The use of the ρ parameter is required to accurately model the microlensing light curve when finite source effects become significant. ρ is defined as:

$$\rho = \frac{\theta_*}{\theta_E} \tag{2.17}$$

where θ_* is the angular size of the source. Finite source effects are usually observable for high magnification events when the source passes near or over the lens (for binaries, near or over the caustics) and are revealed by the sharp features in the light curve that occur in most binary microlensing events. Since we often know the magnitude and color of the source we can use an infrared surface brightness relation such as that from Kervella et al. (2004) that relates $(V-H, H)$ to θ_E. Using this to estimate the size of the angular Einstein ring, we arrive at the first of our relationships which relate the mass, M_L and distance D_L of the lens:

$$M_L = \frac{\theta_E^2}{\kappa \pi_{rel}} \tag{2.18}$$

where the relative parallax, $\pi_{\rm rel} = \mathrm{AU}\left(\frac{1}{D_L} - \frac{1}{D_S}\right)$ and $\kappa = 8.144\ \mathrm{mas\ M}_\odot^{-1}$. With the only unknowns in this equation being M_L and D_L, we can use this to place a constraint on the mass-distance of the lens.

2.2.2 Microlensing Parallax

Microlens parallax occurs when the co-spatial assumption that the observer, lens and source are moving with the same velocity breaks down. There are three different ways this can effect can be observed and subsequently used to provide constraints on the lens mass

and distance. The first is orbital parallax which is detectable for long-time scale events with a duration significant compared to that of a year, usually around a month (Muraki et al. 2011). The acceleration of the Earth during this period results in a non-uniform and/or non-rectilinear trajectory of the lens and source which causes measurable deviations in the event light curve (Gould & Loeb 1992). The second is terrestrial parallax which causes changes in the observed magnification when observing at spatially separated observing sites (Gould 1994; Gould et al. 2009). The third occurs when observers are separated by a significant fraction of an AU, such as with satellites such as the now-defunct Spitzer space-telescope. Care must be taken with these data though, as systematic errors can be a problem (**?**), and the solutions are still degenerate with the orbital motion of the planetary companion. This "microlens parallax" determined by one of more of these three ways is distinct from the relative parallax due to the lens and source distances as defined in the previous section.

The resulting mass-distance relation, once again with D_L and M_L being our only unknowns, is:

$$M_L = \frac{\pi_{rel}}{\kappa \boldsymbol{\pi}_E^2} \tag{2.19}$$

The difficulty when trying to measure the parallax vector, $\boldsymbol{\pi}_E$, is that it is often degenerate with orbital motion of the planet (Gould 1994; Batista et al. 2011). This means that it is usually only robustly measured in the direction perpendicular to the Earth-Sun acceleration measured instantaneously at the time of the event. An independent measurement of the proper motion of the lens, however, by using adaptive optics observations to determine its location, makes its possible to to resolve this degeneracy, since $\boldsymbol{\pi}_E$ is parallel to the proper motion, $\boldsymbol{\mu}_{rel}$. A notable example, and the first result from our recent Keck proposal is shown in Bhattacharya et al. (2018), where the lack of constraint in the $\pi_{E,N}$ direction is broken by measuring the proper motion in the heliocentric reference frame, $\boldsymbol{\mu}_{rel,H}$, using Hubble Space Telescope (HST) and Keck photometry to determine centroid shifts in the

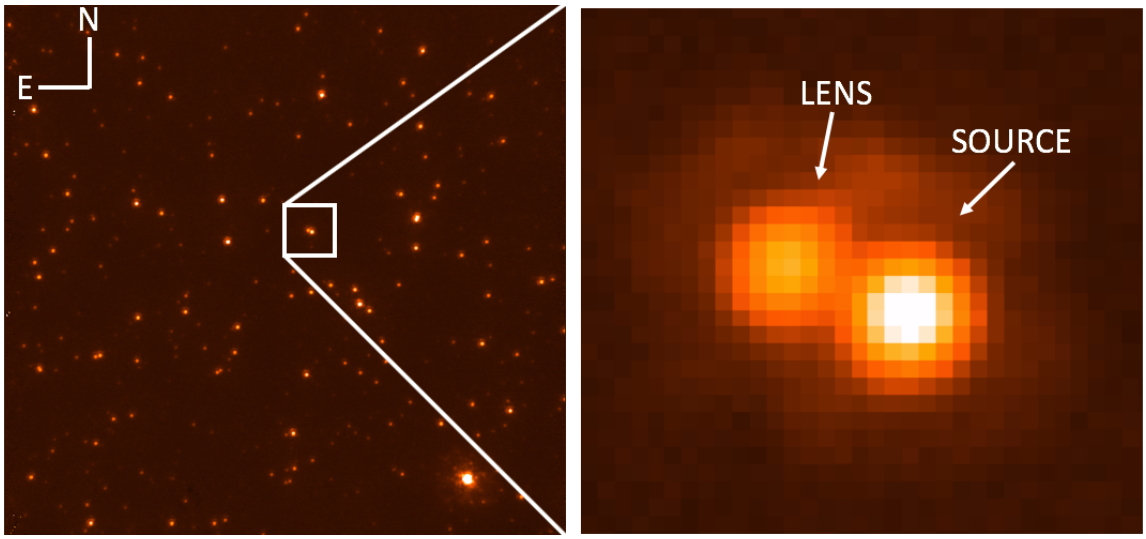

Figure 2.5: K-band NIRC2/Keck image of MOA-2013-BLG-220. Panel **(A)** shows a full $10'' \times 10''$ frame from the narrow camera. Panel **(B)** is a zoom of panel (a) and shows the clear separation between the lens and source (Vandorou et al. 2020).

lens and source stars. That $\boldsymbol{\mu}_{rel}$ is parallel to the parallax $\boldsymbol{\pi}_E$ will be relevant in predicting the possible location of a dark lens in Chapter 5.

2.2.3 Measuring the Lens Flux and Constraining Proper Motion

Using the typical 1-2m telescopes of microlensing surveys and follow-up telescopes used to populate data points on the event light curve, the light from the source and lens are observed as a blend in a single point-spread function (PSF), often with other unrelated stars. At the 1-2 arcsecond seeing commonly achievable at these observing sites it is not possible to uniquely differentiate the light from the source from the lens and other sub-arcsecond blend stars. However, high angular resolution imaging from large ground based facilities like Keck, Subaru and VLT, as well at imaging from the Hubble Space Telescope (HST) are capable of reaching resolutions on the 50-100mas level, and can hence be used to resolve blend fluxes given sufficient time following maximum magnification. While resolving these objects is ideal (eg. MOA-2013-BLG-220 as in Figure 2.5), a centroid shift can also be sufficient to determine the lens flux *and* constrain the lens-source proper motion

(as shown in Bhattacharya et al. (2018)). With a typical lens-source relative proper motion of the order between 4-12 mas/yr, often only a few years following are required before a centroid-shift in the associated point-spread function (PSF) of the source is detectable. Even if they are not resolved one can use adaptive optics observations to isolate the lens and source from other blend stars, and then use the predicted baseline source magnitude to estimate the lens flux. An example of this method can be seen in the super-Earth event OGLE-2017-BLG-1434 in Chapter 4.

Combining our lens flux measurement with empirical mass-luminosity relations or stellar isochrones (eg. Bertelli et al. (2008)) we can write a third mass-distance relationship:

$$m_L(\lambda) \;=\; 10 \,+\, 5log(D_L/1\text{ kpc}) \,+\, A_L(\lambda) \,+\, M_{isochrone}(\lambda, M_L, age, [Fe/H]) \quad (2.20)$$

where $m_L(\lambda)$ is the apparent magnitude of the lens, D_L is the distance to the lens, $A_L(\lambda)$ is the extinction to the lens in band λ, and M_{iso} is an absolute magnitude derived from stellar isochrones.

While further details of AO observations and the subsequent analysis are detailed in the following section, the three mass-distances relationships described here are critical to a high-resolution microlensing follow-up program. Direct examples of their use can be found in the Chapter 3, 4 and 5 of this thesis.

2.3 Adaptive Optics Follow-up

Prior to the NASA Keck observations (PI: Bennett) used in this thesis which began in 2018, high-angular resolution observations have previously been obtained with Subaru, Keck, Magellan, VLT and the Hubble Space Telescope (Bennett et al. 2006; Batista et al. 2015; Beaulieu et al. 2018). About 60 planetary events have been observed. Published results from these programs can be found in Figure 2.7. Some of these studies involve the

detection of excess flux at the position of the source. This flux, assuming it was observed shortly after the end of the microlensing event when the lens and source have not yet separated, must include the lens flux. While it is likely that such flux is dominated by the lens, as is assumed in Batista et al. (2014) and Fukui et al. (2015), it possible that this flux could also be due to an unrelated star, which was shown in the case of MOA-2008-BLG-310 and comparing predictions of the lens–source relative proper motion, μ_{rel} and imaging from HST (Bhattacharya et al. 2017). To properly account for this we must use a Bayesian analysis using priors assuming stellar binary distributions and a stellar luminosity function (Koshimoto et al. 2017), though this is not required when either lens-source proper motion or parallax from the microlens model are consistent with the measured flux (Bennett et al. 2015; Gaudi et al. 2008; Beaulieu et al. 2016).

The most recent coordinated campaign to obtain high-resolution follow-up comes began with the 2018A Keck proposal (PI: Bennett) which was designed as a systematic study of more than 100 microlensing events aimed at determining host star and planet masses and their distances in the Milky Way. This program was specifically pitched as a proposal in support of the Roman Space Telescopes (RST, then named WFIRST, Spergel et al. (2015)). It's planned that RST will increase microlensing planet detections by an order of magnitude. To cope with this huge influx of data, not only does the (comparatively small) microlensing community need better, more automated methods to model and study event light-curves, we need more clearly definied techniques to measure the masses of these planets and their hosts.

The initial proposal was for 10 half-nights, split between laser-guide star OSIRIS (OH-Suppressing Infra-Red Imaging Spectrograph) observations and those with the near infrared imager, NIRC2. In practice, most of the observations were taken on Keck II with NIRC2 simply due to telescope allocation. We observed for 15-half nights in 2018-19, with an additional 4 nights lost due to the Mauna Kea protests and one night completely

lost due to weather. Data were acquired on 60 events, with event choice dictated by those that could potentially yield the resolution of the lens and source or high-quality lens flux measurements. To start with this was based on events in the "Suzuki sample" used to create Figure 1.2 (Suzuki et al. 2016).

A number of studies from this program have been or are soon to be published. The first was Bhattacharya et al. (2018), which constrained the lens-source relative proper motion of OGLE-2012-BLG-0950Lb using simultaneous data from Keck and HST. Both MOA 2013-BLG-220L (Vandorou et al. 2020) and OGLE-2005-BLG-071L (Bennett et al. 2020) show a clear separation of the lens and source, while in Blackman et al. (2020) (presented in Chapter 3), I show that in the case of the stellar binary MACHO 97-BLG-28 that this was not possible. The next two results from our observing program are presented in Chapter 4 (OGLE-2017-BLG-1434) and 5 (MOA-2010-BLG-477). OGLE-2017-BLG-1434 (Blackman 2020b, in prep) shows a high quality lens flux measurement with Keck AO data obtained only a year after maximum magnification. These data, unlike other events (Vandorou et al. 2020) are in good agreement with the discovery paper (Udalski et al. 2018).

The most exciting result comes in Chapter 5 with the discovery of the first single white dwarf with a gas giant companion (MOA-2010-BLG-477, Blackman (2020c), in prep). Since microlensing does not rely on light from the light from the host star like other detection methods such as radial velocity and transits, it is sensitive to free-floating planets and stellar remnants, including black holes. If this time since maximum magnification is sufficient that the lens and source are no longer perfectly aligned, it is possible to leverage the prediction of lens-source relative proper motion to asses the position of the lens. Alternatively, if no flux excess is detected at the position of the source, it may be possible to place limits on the expected flux of the lens. MOA-2011-BLG-262, for example, has a statistically compatible source+lens flux and predicted source flux, implying a potential

dark lens (Bennett et al. 2014). For MOA-2010-BLG-477, the lack of a lens detection at the position indicated by the predicted relative proper motion strongly suggests that the lens star is a white dwarf. A full study of this event, soon to be submitted to the journal Science, can be found in Chapter 5

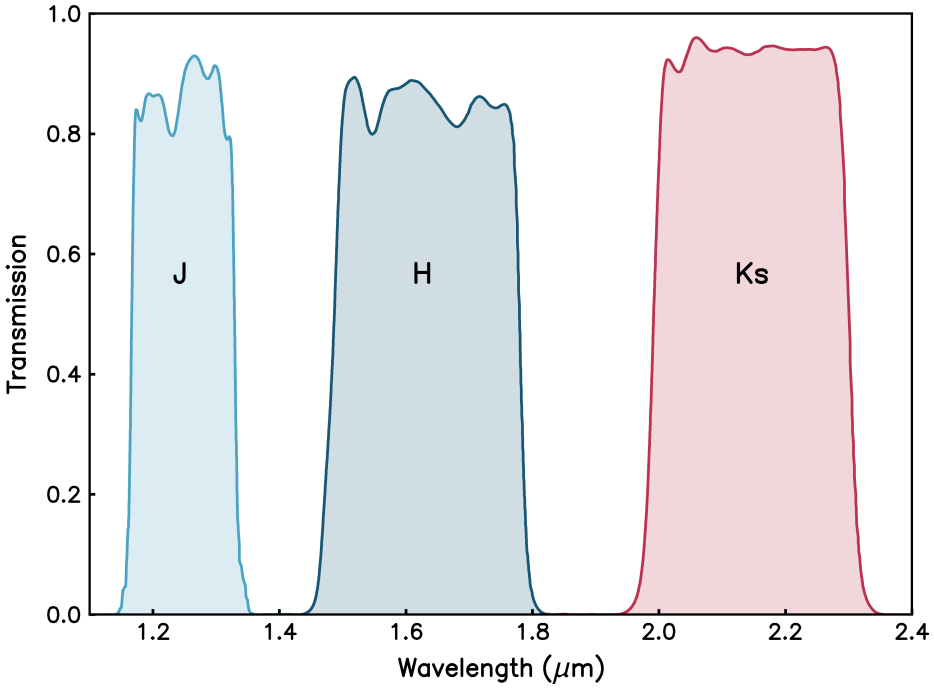

Figure 2.6: Filter transmission curves for NIRC2. NIRC2 is a near-infrared imager installed behind the AO bench on the Left Nasmyth Platform of Keck II. We use the J, H and K_s bands.

2.3.1 Observing Strategy and results

We observe in the near-infrared, in JHK$_S$-bands (Figure 2.6). Typically a K_s-wide is taken first, since the shorter wavelength bands are more affected by extinction. Since 99% of our targets lie in the galactic bulge, the targets are only observable for half nights in the best case (in the 2018A season, this meant the last half of the night 16 May-7 June, and 6-31 July the first night). While laser guide-star (LGS) is preferable, sometimes natural

guide star (NGS) targets are needed for instances where there is sufficiently bright and/or close tip-tilts stars or due to one of the regular laser-outage periods due to safety/security concerns. In the initial proposal, half of all targets were observable with NGS. Under the best conditions with FWHM $\sim$ 50 mas, we prioritize targets where lens-source centroid shifts are predicted to be measurable. When the image FWHM is > 100 we instead shift to lens flux measurements.

In Table. 2.7 I present an overview of published events that use data from this program and previous adaptive optics follow-up proposals. Details of the data reduction process (including flat-fielding etc) are discussed in later chapters as they arise. Details of my (and Aikaterini Vandorou's) code to perform basic reduction operations on raw images from Keck can be found in Appendix A.

Name	Observatory	Bands	Year	Distance (kpc) Initial	Distance (kpc) with HR	Mass ($M_\odot$) Initial	Mass ($M_\odot$) with HR	References
This Thesis								
MACHO-97-BLG-28	Keck/NIRC2	JK	2013	$4-8$	7.0 ± 1.0	$0.09-0.81$	$0.24^{+0.28}_{-0.12}$	Albrow et al. 1999 Chapter 3
OGLE-2017-BLG-1434	Keck/NIRC2	K	2018	0.86 ± 0.09	0.86 ± 0.05	0.234 ± 0.26	0.234 ± 0.012	Udalski et al. 2018 Chapter 4
MOA-2010-BLG-477	Keck/NIRC2	HK	2015 2016 2018	2.3 ± 0.6	1.88 ± 0.44	$0.13-1.0$	0.58 ± 0.16	Bachelet et al. 2012 Chapter 5
with candidate Co-Authorship								
OGLE-2014-BLG-124	Keck/NIRC2	HK	2016	4.23 ± 0.6	3.5 ± 0.2	0.65 ± 0.22	0.90 ± 0.05	Udalski et al. 2015 Beaulieu et al. 2018
OGLE-2012-BLG-950	Keck/NIRC2 HST/WFC3	H VI*	2018		2.19 ± 0.23		0.58 ± 0.04	Koshimoto et al. 2016 Bhattacharya et al. 2018
OGLE-2005-BLG-071	Keck/NIRC2	K	2019	$1.5-5$	3.46 ± 0.33	$0.08-0.5$	0.426 ± 0.037	Udalski et al. 2005 Dong et al. 2009 Bennett et al. 2020
MOA-2013-BLG-220	Keck/NIRC2	K	2015 2019	$1.6-6.5$	6.72 ± 0.59	$0.05-0.8$	0.88 ± 0.05	Yee et al. 2014 Vandorou et al. 2020
MOA-2007-BLG-400	Keck/NIRC2	HK	2018	$5.8^{+0.8}_{-0.7}$	6.89 ± 0.75	$0.30^{+0.19}_{-0.12}$	0.721 ± 0.044	Dong et al. 2009 Bhattacharya (in prep)
MOA-2009-BLG-319	Keck/NIRC2	HK	2015 2018	$6.1^{+1.1}_{-1.2}$	6.9 ± 0.3	$0.38^{+0.34}_{-0.18}$	0.82 ± 0.05	Miyake et al. 2011 Terry (in prep)

Name	Observatory	Bands	Year	Distance (kpc) Initial	Distance (kpc) with HR	Mass ($M_\odot$) Initial	Mass ($M_\odot$) with HR	References
OGLE-2003-BLG-235	Keck/NIRC2	JK	2018	$5.2^{+0.2}_{-2.9}$	5.2 ± 0.5	$0.36^{+0.03}_{-0.28}$	0.56 ± 0.04	Bond et al. 2004 Bennett et al. 2006 Beaulieu (in prep)
Other Observations with HR follow-up								
OGLE-2013-BLG-132	Keck/NIRC2	JHK	2013	$3.9^{+1.5}_{-1.3}$	3.45 ± 0.75	$0.54^{+0.30}_{-0.23}$	0.50 ± 0.08	Mróz et al. 2017 Beaulieu (in prep)
OGLE-2012-BLG-026	Keck/NIRC2 Subaru/IRCS	H	2012	4.08 ± 0.4	4.0 ± 0.3	0.82 ± 0.13	1.06 ± 0.05	Han et al. 2013 Beaulieu et al. 2016
MOA-2011-BLG-293	Keck/NIRC2	K	2012	7.15 ± 0.94	7.72 ± 0.44	$0.59^{+0.35}_{-0.29}$	0.86 ± 0.06	Yee et al. 2012 Batista et al. 2014
MOA-2007-BLG-192	VLT/NACO	JHK	2007	1.0 ± 0.4	$0.66^{+0.1}_{-0.07}$	$0.06^{+0.028}_{-0.021}$	$0.084^{+0.015}_{-0.012}$	Bennett et al. 2008 Kubas et al. 2012
OGLE-2005-BLG-169	HST/WFC3 Keck/NIRC2	H	2011 2013	$2.7^{+1.6}_{-1.3}$	4.2 ± 0.2	$0.49^{+0.23}_{-0.29}$	0.69 ± 0.02	Gould et al. 2006 Batista et al. 2015 Bennett et al. 2015
Other Observations with HR follow-up only								
MOA-2016-BLG-227	Keck/NIRC2	H	2016		6.5 ± 1.0		$0.29^{+0.23}_{-0.15}$	Koshimoto et al. 2017
OGLE-2013-BLG-605	Keck/NIRC2	H	2015		$3.74^{+0.68}_{-0.55}$		$0.201^{+0.03}_{-0.095}$	Sumi et al. 2016
OGLE-2012-BLG-563	Subaru/IRCS	JHK	2012		$1.3^{+0.6}_{-0.8}$		$0.34^{+0.12}_{-0.20}$	Fukui et al. 2015
OGLE-2012-BLG-006	Keck/NIRC2	J	2013		$5.3^{+0.8}_{-1.3}$		$0.49^{+0.27}_{-0.23}$	Poleski et al. 2017

Name	Observatory	Bands	Year	Distance (kpc) Initial	Distance (kpc) with HR	Mass ($M_\odot$) Initial	Mass ($M_\odot$) with HR	References
MOA-2008-BLG-310	HST/WFC3	VI*	2012		7.7 ± 1.1		0.21 ± 0.14	Janczak et al. 2010 Bhattacharya et al. 2017
OGLE-2007-BLG-368	Keck/NIRC2	HK	2007		$5.9^{+0.9}_{-1.4}$		$0.64^{+0.21}_{-0.26}$	Sumi et al. 2010
OGLE-2007-BLG-387	VLT/NACO	H	2010		7.2 ± 0.8		$0.11^{+0.21}_{-0.06}$	Batista et al. 2011
OGLE-2007-BLG-349	HST/WFPC2	VI*	2007 2008		2.74 ± 0.38		0.41 ± 0.07 0.30 ± 0.07	Bennett et al. 2016
OGLE-2006-BLG-109	Keck/NIRC2	HK	2007		$1.51^{+0.11}_{-0.12}$		$0.51^{+0.05}_{-0.04}$	Gaudi et al. 2008 Bennett et al. 2010

Table 2.7: Published Microlensing Events with High-Resolution Observations. This is an updated version of the table presented in Beaulieu et al. (2018) with more information and publications added as of May 25, 2020. *HST bands F814W & F555W which are analogous to VI.

The published portion of chapter 3 has been removed for copyright or proprietary reasons.

It is the following published article:
Blackman, J. W., Beaulieu, J. P., Cole, A. A., Vandorou, A. et al., 2020. Confirmation of the stellar binary microlensing event, Macho 97-BLG-28, Astrophysical journal, 890(87), 1-7

3

MACHO-97-BLG-28

Confirmation of a Stellar Binary

In this chapter I present my paper on the microlensing event MACHO 97-BLG-28 which was published in the Astrophysical Journal on February 10, 2020. Below I offer some introductory comments regarding the context of this paper, followed by a statement of author contributions. The paper is presented in its original format as published in the journal.

3.1 Background & Context

In the early 1990s a project was conceived to search for microlensing events caused by massive compact halo objects (MACHOs) in the halo of the Milky Way (Alcock et al. 1996) in an effort to search for dark matter. From July 1992 the resulting MACHO collaboration traced the brightness of stars in the Large Magellanic Cloud (LMC), Small Magellanic Cloud (SMC) and the Milky way bulge in an effort to detect the telltale increase in magnification that could be the result of microlensing. Some of these events were later followed-up by the PLANET (Probing Lensing Anomalies NETwork) collaboration, of which the University of Tasmania was part. They used a longitudinally distributed network of telescopes in the southern hemisphere aimed at obtaining densely sampled photometric light curve of microlensing events. The ultimate goal was to find anomalies in the light curves implying the existence of a binary lens with planetary-mass companions. No exoplanet-mass binary detections were made from this program, however 21 examples of binary systems were found in the first six years of MACHO, of which 3 were found in 1997. One of these was MACHO 97-BLG-28.

The discovery paper on this object (Albrow et al. 1999) noted that the event contained the first observed cusp caustic-crossing and was the first time that limb-darkening coefficients had been determined by microlensing. When adaptive optics follow-up programs were discussed in the early 2010s, the large time interval of over 15 years since the event reached maximum magnification meant that it would be an ideal test candidate for Keck observations in 2013 (PI: V. Batista). With a relative lens-source proper motion prediction from the discovery paper of $\mu_{rel} = 4.09 \pm 0.55$ mas yr^{-1} the lens and source had a predicted separation of 66 ± 9 mas in 2013. Given ideal conditions at Keck, typically of the order of 50 mas Full-Width Half Maximum (FWHM) using the NIRC2 imager, it should have been possible to at least determine the centroid shift between the two stars, if not outright resolve them. However, my modelling of the light curve and new estimates

of the relative lens source proper motion results in smaller predictions for the separation of $\mu_{rel} = 2.8 \pm 0.5$ mas yr^{-1}. As such, in the following paper I show that it was not possible resolve the lens and source for this event. I remodel the event using additional data from the Mt. Stromlo 74" telescope, model estimates of stellar limb darkening, and fitting of the blend separately for each telescope and passband. I then offer revised estimates of the lens mass and distance which slightly favours the conclusion that the event is a stellar M-dwarf binary.

To model this event I make use of the open-source microlensing modelling package pyLIMA ("python Lightcurve Identification and Microlensing Analysis") written primarily by Etienne Bachelet (Bachelet et al. 2017). pyLIMA contains a number of modules. The input data from the microlensing event including the photometric data from the telescopes are entered in the *Events* and *Telescopes* modules, as part of a python class. The Microlmodels module allows the user to select the type of model desired, eg. a Point-Source Point-Lens (ie. Paczynski) model or a model such as Finite-Source Point-Lens (FSPL) which takes into account second order effects such as parallax and the lens orbital motion. This class calls upon the Microlfits model which defines the fitting method. The three techniques available in pyLIMA are the Levenberg–Marquardt (LM) algorithm (Levenberg 1944; Marquardt 1963), the Differential Evolution (DE) method (Storn & Price 1997) and a Monte Carlo Markov Chain (MCMC) using the emcee algorithm (Foreman-Mackey et al. 2013), the latter of which can be used to generate posterior probability distributions.

When modelling MACHO 97-BLG-28 we first utilize the global optimizing Differential Evolution method to determine the best uniform-source binary lens (USBL) model. This does not take into account the finite size of the source, however the resulting estimates will be close enough to the subsequent Finite-Source Binary Lens model (FSBL) determined via a MCMC that it can be used as a first guess in order to speed up computation

time. In accordance with Yoo et al. (2004) and Cassan et al. (2006) we describe the magnification of an extended source with a linear limb-darkening law (Milne 1921; An et al. 2002). Full details of the implementation of pyLIMA's models can be found in Bachelet et al. (2017) as well as the code's documentation (https://github.com/ebachelet/pyLIMA).

3.2 Author Contributions

- Observations were made at the Keck Observatory on Mauna Kea, Hawaii as part of a proposal led by Virginie Batista.
- All data-reduction and light-curve fitting was performed by Joshua Blackman using `Sextractor`, `Swarp`, `PyLIMA` and `Python`. Assistance with `PyLIMA` was provided by Etienne Bachelet.
- Analysis was performed by Joshua Blackman alongside discussion with Jean-Philippe Beaulieu, Andrew Cole and David Bennett.
- The Markov-Chain Monte Carlo used to create Figure 4 was written and provided by Naoki Koshimoto.
- The remaining figures and text was written and created by Joshua Blackman with suggestions and corrections provided by Andrew Cole and Jean-Philippe Beaulieu.

4

OGLE-2017-BLG-1434

Confirmation of a Cold Super-Earth

In this chapter I present my paper on the microlensing event OGLE-2017-BLG-1434 that is shortly to be submitted to AJ. Below I offer some introductory comments regarding the context of this paper, followed by a statement of author contributions. The paper has been modified from its original format.

4.1 Background & Context

The first exoplanets ever detected (around pulsar PSR B1257+12) were super-Earths (Wolszczan & Frail 1992), though it was not until 2005 that the first such planet was detected orbiting a main sequence star. This latter was discovered using high cadence radial velocity monitoring around star GJ 876 with Keck, and was estimated to be a $\sim 7.5 M_{\oplus}$ mass planet which was at the time the lowest mass exoplanet found around a main sequence star (Rivera et al. 2005). This system is similar to that of OGLE-2017-BLG-1434 in terms of containing a low-mass host star ($0.32 M_{\odot}$ for GJ 876 vs. $0.23 M_{\odot}$ for OGLE-2017-BLG-1434) and hence being analogous to a scaled ice giant system.

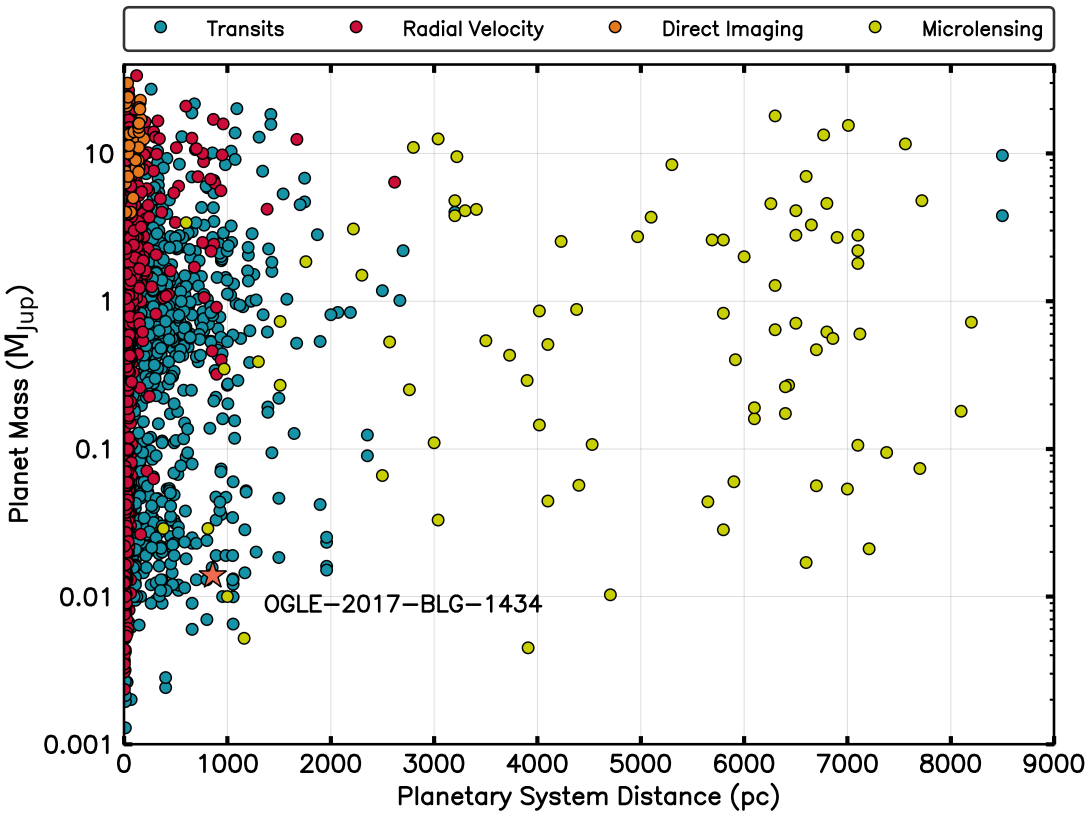

Figure 4.1: Distances to discovered exoplanets The distance distribution of exoplanets discovered with the four major detection methods (radial velocity, transits, direct imaging and microlensing). Note that the majority of non-microlensing detected exoplanets lie within 2 kpc. The position of OGLE-2017-BLG-1434 is marked with an orange star.

As discussed in Chapter 2, one of the primary goals of current microlensing observations is to complete the statistical sample of planets in the region at and beyond the snow line. Ideally, we want this sample to span as broad a range of properties as possible. This includes both the masses and distances of the planets themselves, but also of their host star properties (mass, age, metallicity), and their location the galactic plane. Following the first study to measure the planet mass-ratio function (Sumi et al. 2010), Suzuki et al. (2016) presented a statistical review of planets detected with the MOA-II survey between 2007 and 2012. Suzuki et al. (2016) characterize the exoplanet mass-ratio function as a broken power low with a break at $q = 1.7 \times 10^{-4}$. While a subsequent study fit this break to instead occur at $q = 0.55 \times 10^{-4}$ (Jung et al. 2019), both argue for this break due to the high sensitivity of current exoplanet surveys to low-mass ratio planets compared to the low number of planets detected. Even then, numbers are few, and more low ratio detections and confirmations will be able to confirm and/or refute this turnover. Once such object is discussed in the following paper: the super-Earth OGLE-2017-BLG-1434 (Udalski et al. 2018).

In this study I follow the method demonstrated in other microlensing follow-up studies that utilize Keck observations (Beaulieu et al. 2018; Bhattacharya et al. 2018; Bennett et al. 2020). While in some cases the lens and source star can be resolved (Vandorou et al. 2020), observations of OGLE-2017-BLG-1434 were taken too soon after maximum magnification for this to be possible. We can however still obtain a measurement of the blend flux at the position of the source, and hence place constraints on the lens mass and distance. We use the NIRC2 1-5 μm near-infrared imager located at the left Nasmyth platform on the Keck II telescope. This is the most accessible (due to allocation of telescope time in accordance with collaborator affiliation) instrument for this task which is capable of achieving $\sim$50 mas resolution images. Since resolving the source and lens is not yet possible, only wide frame images with a pixel scale of 0.039686 arcsec/pixel are needed. This means

we can calibrate the photometry directly with images from the Vista Variables in the Via Lactea (VVV) survey (Minniti et al. 2010), as there are sufficient stars within the frame to do so[1]. We use the pipeline presented in Appendix A, co-written by the author, to perform standard image reduction (eg. dark frames, flat fielding, sky subtraction). Standard methods are then used (see Beaulieu et al. (2018)) to calibrate the data and correct for extinction. We then follow the Bayesian approach of Koshimoto et al. (2020) to determine the lens star masses and distances. Details of the Markov Chain Monte Carlo method used to create Figure 4. can be found in Section 3 of Koshimoto et al. (2020).

4.2 Author Contributions

- Observations were made by Joshua Blackman at the Keck Observatory on Mauna Kea, Hawaii in August 2018 as part of a proposal led by David Bennett.
- All data-reduction and light-curve fitting was performed by Joshua Blackman using `Sextractor`, `Swarp`, and a `Python` pipeline written by Joshua Blackman (80%) and Aikaterini Vandorou (20%).
- Analysis was performed by Joshua Blackman alongside discussion with Jean-Philippe Beaulieu and Andrew Cole.
- The Markov-Chain Monte Carlo used to create Figure 4 was written and provided by Naoki Koshimoto.
- The figures and text in the manuscript were written and created by Joshua Blackman with suggestions and corrections provided by Andrew Cole, Jean-Philippe Beaulieu and David Bennett.

[1] Calibrating narrow frames directly to VVV is problematic as the stellar overlap is often only a handful of stars. In such a case (as in Chapter 5) wide frames would be used for calibration in conjunction with stellar flux-ratios determined from the narrow frames.

Confirmation of the cold Super-Earth Planet in the microlensing event OGLE-2017-BLG-1434 using Keck Adaptive Optics

ABSTRACT

The microlensing event OGLE-2017-BLG-1434 features a cold super-Earth planet which is one of eight microlensing planets with a planet-host star mass ratio $q < 1 \times 10^{-4}$. We provide an additional mass-distance constraint on the lens host using near-infrared adaptive optics photometry from Keck/NIRC2. We are able to determine a flux excess of $K_L = 16.96 \pm 0.11$ which most likely comes entirely from the lens star. Combining this with constraints from the large Einstein ring radius, $\Theta_E = 1.40 \pm 0.09$ mas and OGLE parallax we confirm this event as a super-Earth with mass $m_p = 4.43 \pm 0.25 M_\oplus$. This system lies at a distance of $D_L = 0.86 \pm 0.05\,\mathrm{kpc}$ from Earth lens star has a mass of $M_L = 0.234 \pm 0.012 M_\odot$. This system suggests that Neptune mass-ratio planets are common around M-dwarfs.

4.3 Introduction

The core accretion theory of planet formation (Pollack et al. 1996) predicts a planetary desert at intermediate planet/host mass ratios of $1 < q/10^{-4} < 4$ (Suzuki et al. 2016). This is due to runaway gas accretion which involves the rapid accumulation of hydrogen and helium gas onto protoplanetary cores as they reach masses of $\sim 10 M_\oplus$. This results in a dearth of intermediate-mass giant planets between Saturn mass planets at $\sim 95 M_\oplus$ and failed gas giants at $\sim 10 M_\oplus$. The predicted lack of planets with these masses is however in conflict with planet demographics determined from microlensing observations (Suzuki et al. 2016, 2018).

Suzuki et al. (2016) compiled a sample of 30 planetary microlensing events from the MOA (Microlensing Observations in Astrophysics) survey observed between 2007 and

2012 and compared that with population synthesis models (Suzuki et al. 2018). They show that these models underestimate the number of planets with $1 < q/10^{-4} < 4$ by a factor of ten. They estimate the mass ratio distribution of exoplanets to be a broken power law with a break occurring at $q \sim 1.75 \times 10^{-4}$. A subsequent study used 15 low mass-ratio microlensing events and estimated this break to be instead at $q \sim 0.55 \times 10^{-4}$ (Jung et al. 2019). While the distribution at higher mass ratios is a well-sampled as a decreasing power-law, there are only a eight planets with mass ratios with $q < \times 10^{-4}$, while is why arriving to robust statistical conclusions in this region of parameter space is difficult.

OGLE-2017-BLG-1434, discussed in this paper, is the most recently discovered of these eight planets. It is a cold super Earth planet with mass ratio $q = 0.572 \times 10^{-4}$ (Udalski et al. 2018). Well measured microlens parallax meant that the physical parameters could be comparatively well measured, with the mass of the planet and its stellar host determined to be $m_p = 4.4 \pm 0.5 M_\oplus$ and $M_L = 0.23 \pm 0.03 M_\odot$, respectively. However, as in typical microlensing events a Bayesian analysis with constraints from the Einstein radius crossing time and measurable secondary effects (eg. due to the finite size of the source) are required in combination with a galactic model (eg, Sumi et al. (2011); Bennett et al. (2014)) to obtain estimates of these physical parameters. Without secondary constraints these estimates usually have an accuracy of 30-40%.

This first of these constraints can be derived from the sharp light curve features of many binary microlensing events. This enables one to measure the finite angular source radius (Beaulieu 2018) and hence a relationship between the lens mass and distance:

$$M_L = \frac{\theta_E^2}{\kappa \pi_{rel}} \tag{4.1}$$

where θ_E is the Einstein radius, π_{rel} the relative parallax and $\kappa = 4G/c^2 \mathrm{AU} = 8.144 \text{ mas } M_\odot^{-1}$. A second constraint on the lens mass and distance can be found by measuring the microlensing parallax, π_E. This can be determined via detection of the Earth's orbital motion

or between two spatially separated observing sites:

$$M_L = \frac{\pi_{rel}}{\kappa \pi_E^2} \tag{4.2}$$

Space-based parallax from observatories in Low Earth Orbit (e.g. Spitzer) and beyond are ideal in constraining π_E, though systematic errors may be a problem (Koshimoto & Bennett 2020), and the solutions are still degenerate with the orbital motion of the planetary companion. Finally, a third mass-distance relation can be obtained by measuring the flux of the lensing system using high-angular resolution observations from 8-10 metre class telescopes. This makes it possible to decouple the source and lens contributions from that of other blend stars. The relation that follows is:

$$m_L(\lambda) \quad = \quad 10 \; + \; 5log(D_L/1 \text{ kpc}) \; + \; A_L(\lambda) \; + \; M_{iso}(\lambda, M_L, age, [Fe/H]) \tag{4.3}$$

where $m_L(\lambda)$ is the apparent magnitude of the lens, D_L is the distance to the lens, $A_L(\lambda)$ is the extinction to the lens in band λ, and M_{iso} is an absolute magnitude derived from stellar isochrones. It's this relationship which we use in this paper to better quantify the mass and distance of OGLE-2017-BLG-1434.

We supplement the discovery paper of this event with the addition of high-angular resolution data obtained using the NIRC2 imager on the Keck II telescope on Mauna Kea, Hawaii. We obtained follow-up photometry in August 2018 as part of a NASA Keck Key Strategic Mission Support (KSMS) proposal in support of the Nancy Grace Roman Space Telescope (formerly WFIRST, Spergel et al. (2015)). This program is designed to acquire adaptive optics data of microlensing events in order to constrain the lens flux and/or the source-lens relative proper motion, and hence determine accurate estimates of the planet and host masses. Results from this program can be found in a number of studies (Beaulieu et al. 2016; Bhattacharya et al. 2018; Beaulieu et al. 2018; Vandorou

et al. 2020; Bennett et al. 2020; Bhattacharya et al. 2020; Terry et al. 2020). We use this photometry to measure the lens apparent magnitude $m_L(\lambda)$ from Eq. 4.3 and hence determine a relationship between D_L and M_L. The finite source size, ground parallax and this newly obtained adaptive optics data, combined with theoretical isochrones, allows us to refine the estimate of the mass-distance relationship and confirm this event as a cold super Earth, $m_p = 4.43 \pm 0.25 M_\oplus$, very nearby for a microlensing planet at a distance of $D_L = 0.86 \pm 0.05$ kpc.

4.4 The cold super-Earth OGLE-2017-BLG-1434

OGLE-2017-BLG-1434 was detected by the OGLE Early Warning System at UT19:33 on 25 Jul 2017 using the OGLE 1.3m telescope at Las Campanas. Located at $(RA, Dec)_{J2000} = (17^h53^m07^s.29^s, 30^\circ14'44.6'')$, complementary follow-up data was taken with telescopes from the Korea Microlensing Telescope Network (KMTNet, Kim et al. (2016)) and the MiNDSTEp collaboration at the 1.54m Danish Telescope at La Silla, Chile. The majority of the observations were taken in I-band with V-band data obtained to determine source colors. The resultant light curve was similar to that of a traditional point-lens with the addition of deviations near the event peak. Udalski et al. (2018) determined the source brightness from the fitted light curve and used red clump extinction estimates from Bensby et al. (2013) and Nataf et al. (2013) to derive an angular source size of $\theta_* = 0.657 \pm 0.041$ μas. This results in an Einstein ring radius of $\theta_E = 1.40 \pm 0.09$ mas and a relatively large lens-source relative proper motion, $\mu = 8.1 \pm 0.5$ mas yr^{-1}. This large Einstein ring radius indicates that the lens must either be very close or very massive. The long timescale of the event ($t_E \sim 63$ days) suggests the presence of microlens parallax, though Udalski et al. (2018)'s models were unable to decouple parallax from orbital motion. Udalski et al. (2018) finds two degenerate ($\pm u_0$) models with parameters which are statistically indistinguishable within 1σ.

With a year having elapsed since the peak magnification of OGLE-2017-BLG-1434, the relative source-lens proper motion is such that we would not expect to be able to resolve these blended components with data at the best achievable resolution of Keck/NIRC2 of ~ 50mas. We can, however, compare the predicted source magnitude from the light-curve model with the measured flux of the object at the position of the source, and attempt to decouple and characterize the excess flux.

4.4.1 Keck Observations

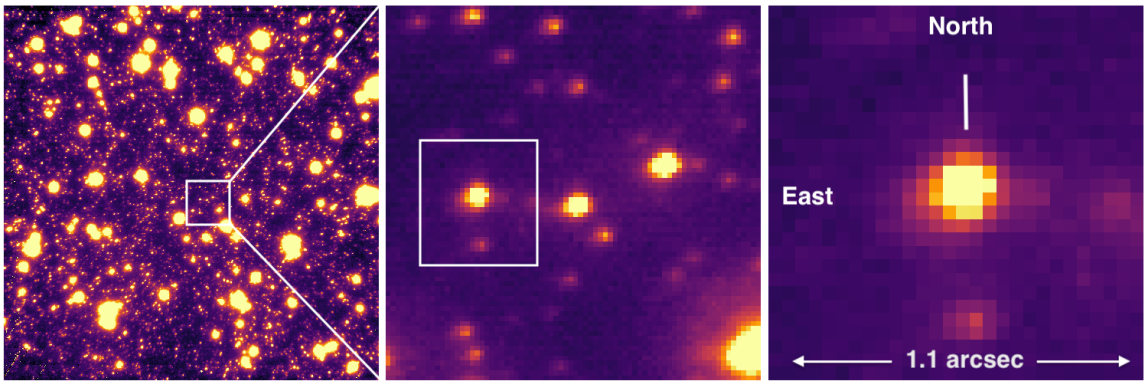

Figure 4.2: K-band images of OGLE-2017-BLG-1434 obtained on August 7, 2018 with Keck/NIRC2. On the far left is an image taken with the wide camera with a 40 arcsec field of view. On the right are two enlargements of this frame showing the position of the source/lens blend, indicated with a white line.

We observed OGLE-2017-BLG-1434 with Keck/NIRC2 on August 7, 2018 (HJD: 2458337.80080). 29 images were obtained in the short K_s band using the wide camera. For simplicity in the rest of this paper we will drop the subscript and refer to the magnitudes simply as K. The wide camera has a plate scale of 0.03968 arcsec pixel^{-1} and a field of view of 40 arcseconds. The best 15 of these images were stacked using SWARP (Bertin & Emmanuel 2010) and calibration performed by cross-matching with the VVV catalog, following the process described in Blackman et al. (2020) and Vandorou et al. (2020). The mean full-width half-maximum (FWHM) is 120 mas along the North axis and 90 mas along the east, indicating an elongation of the point spread function (PSF). This elongation is not severe enough to affect our photometry. The resulting stacked image can be

seen in the left panel of Fig. 4.2. To determine the location of the source we use precise astrometry determined from the OGLE-III survey image. The OGLE image coordinates measured during magnification were (X,Y) = (1829.25, 3196.66) (Private communication, Udalski, 5/12/18) with the source having an OGLE ID of 198963. This places the object at $(RA, Dec)_{J2000} = (17^h53^m07s.312^s, 3014'44.37'')$ in our stacked image (Fig. 4.2). Photometry was performed on this image using SExtractor (Bertin & Arnouts 1996). We find the magnitude of the object at the location of the source to be:

$$K_{blend} = 16.61 \pm 0.07 \tag{4.4}$$

where the blend is defined here as the total flux of the object.

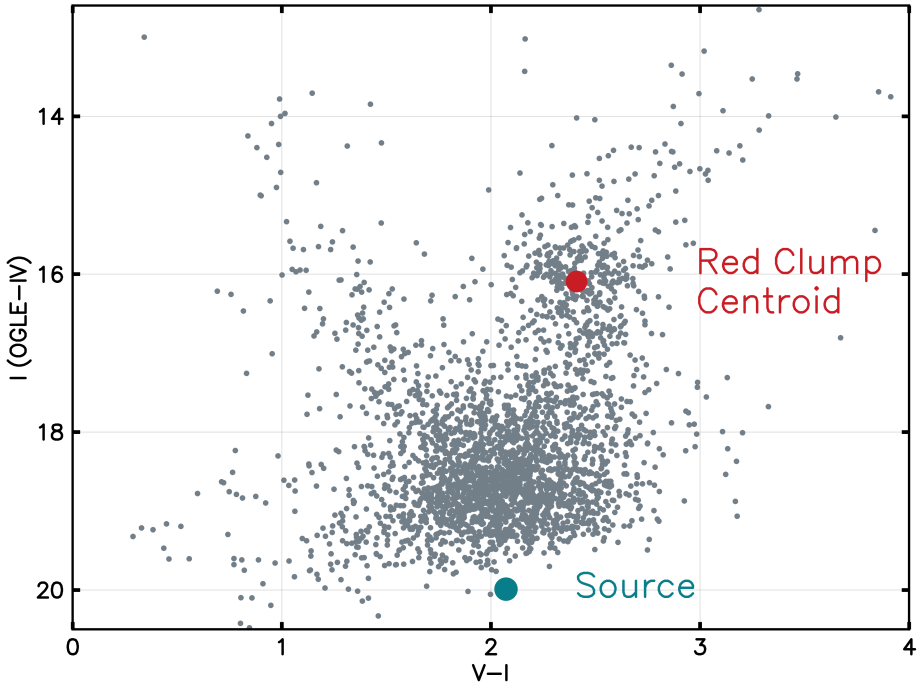

Figure 4.3: OGLE-IV calibrated color-magnitude diagram in V and I. The red circle marks the centroid of the red giant clump while the blue circle indicates the position of the source. The centroid of the red clump is located at $[(V-I)_{RC}, I_{RC}] = (2.41, 16.09)$.

4.4.2 Extinction Estimates

Udalski et al. (2018) determines the intrinsic source color and magnitude to be: $[(V-I)_{S0}, I_{S0}] = (0.732, 18.45) \pm (0.025, 0.063)$. Following the color relations of Bessell & Brett (1988) we can interpolate to find the V-K color, $(V-K)_{S0} = 1.59^{+0.05}_{-0.06}$, and hence the predicted intrinsic K-magnitude of the source, $K_{S0} = 17.59 \pm 0.09$. In order to compare this with our measured K magnitude, we must re-redden this using an estimate of the extinction on the path towards the source. We find $A_K = 0.259 \pm 0.021$ using the OGLE extinction calculator[2] to estimate the K-band extinction at galactic coordinates $(l, b) = (0.28, 2.07)$. This value is derived from a natural neighbour interpolation of good points from Table 3 in Nataf et al. (2013) and assuming $E(J-K_s)$ measurements from Gonzalez et al. (2012). We use the values $E(V-I) = 1.521 \pm 0.125$, $R_{JKVI} = 0.3195$ and the extinction law from Nishiyama et al. (2009) with the relationship $E(J-K_s) = R_{JKVI}E(V-I)$. The I-band extinction towards this part of the galactic bulge is estimated as $A_I = 1.801$.

To check our A_K estimate we calculate the extinction directly from the OGLE-III field (Fig. 4.3). Comparing this to the intrinsic brightness of the red clump, $[(V-I)_{RC0}, I_{RC0}] = (1.06, 14.46)$ (Nataf et al. 2013) gives $E(V-I) = 1.55$ which is well within the error given by the OGLE extinction calculator. Using the value of $A_K = 0.259 \pm 0.021$ we hence find a predicted source magnitude of $K_{\rm predict} = 17.85 \pm 0.09$. Subtracting this from Eq. 4.4 we find an excess flux of

$$K_{\rm excess} = 17.03 \pm 0.11 \tag{4.5}$$

We now re-correct for extinction but now only to the distance of the lens. The lens in Udalski et al. (2018) is predicted to be at a 0.86 ± 0.09 kpc, in front of more than half

[2] http://ogle.astrouw.edu.pl/cgi-ogle/getext.py

of the extinction along the 8 kpc line of sight towards the galactic bulge. We follow the procedure as in Bennett et al. (2015) and Beaulieu et al. (2018), using the relationship

$$A_{\mathrm{K_L}} = (1 - e^{-D_{\mathrm{L}}/\tau_{\mathrm{dust}}})/(1 - e^{-D_{\mathrm{S}}/\tau_{\mathrm{dust}}})A_{\mathrm{K_S}} \tag{4.6}$$

where the scale height of the dust towards the galactic bulge is $\tau_{dust} = (0.10 \pm 0.02\mathrm{kpc}) \sin b$ and $b = 2.07$ the galactic longitude. In our case we calculate $A_{\mathrm{K_L}} = 0.073$ adopting a source distance of $D_S = 8.0 \pm 0.5$ kpc as predicted by the OGLE extinction calculator. If the light from this excess is entirely from the lens, or from a combination of objects at the same distance of 0.86 kpc, we find a excess flux of

$$K_{0,\mathrm{excess}} = 16.96 \pm 0.11 \tag{4.7}$$

4.4.3 Lens Properties and Bayesian analysis

We detect an excess flux aligned to the source to better than the best 90mas FWHM of our final swarped Keck image. In order to determine whether this light is (a) entirely from the lens, (b) from a companion to the lens, (c) a companion to the source, or d) from an ambient star unrelated to either the lens or the source, we plot a mass-distance diagram assuming all the light is from the lens. Fig. 5.2 combines constraints from the Einstein Ring Radius, Θ_E, OGLE parallax and our flux measurement of $K_L = 16.96 \pm 0.11$ combined with theoretical isochrones or, in other words, Eq. 4.1, 4.2 and 4.3. We find values for the lens mass and distance consistent with that determined by Udalski et al. (2018), but with smaller uncertainties. The agreement between the model and our additional less flux constraints is such that this excess flux is most likely entirely from the lens.

To test this we perform a Bayesian analysis as described in Koshimoto et al. (2020). Using the galactic model prior from Bennett et al. (2014) and constraints from the large θ_E, the observed t_E and the measured flux excess of $K = 16.61 \pm 0.07$, we find the excess

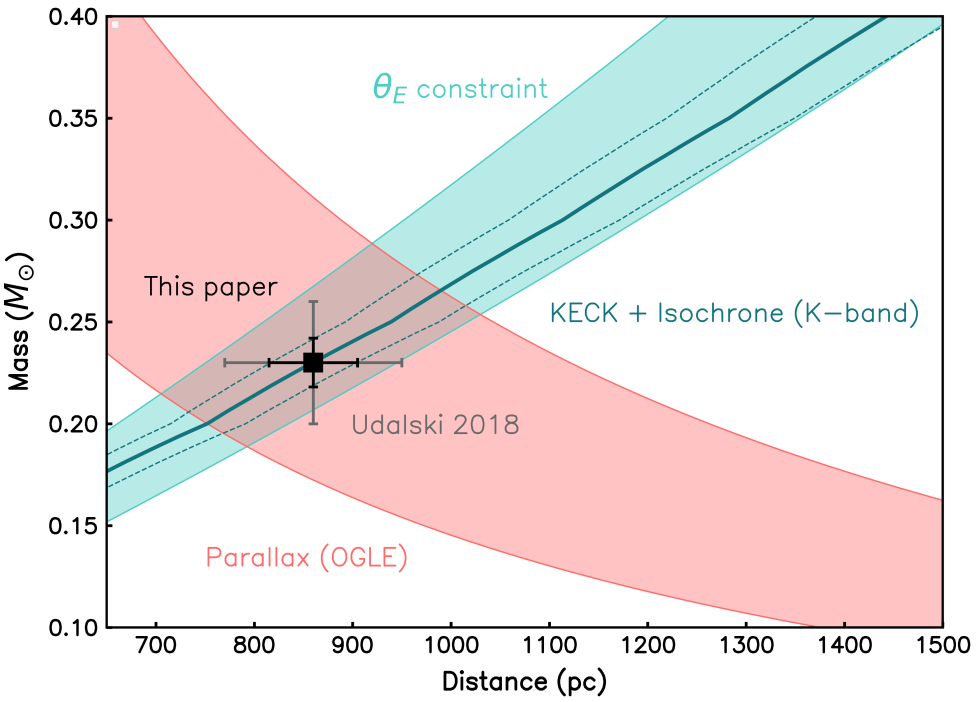

Figure 4.4: Mass-distance diagram showing constraints from the Einstein Ring Radius (θ_E, in blue), from OGLE parallax (in red) and our Keck measurement and K-band isochrones (Girardi et al. 2002), the solid and dotted blue lines. The original estimate from Udalski et al. (2018) is shown with the grey cross at the intersection of the θ_E and OGLE parallax constraints. This paper adds the constraint from lens flux + isochrones. Our estimate is plotted as the black cross.

to very likely be from the lens with a probability of 0.96. In this calculation we deliberately exclude priors from parallax $\boldsymbol{\pi}_{\rm E} = (\pi_{{\rm E},N}, \pi_{{\rm E},E})$. In this case the $\pi_{E,N}$ determined by the Udalski et al. (2018) models lie in the 3σ boundary while $\pi_{E,E}$ is slightly more likely and sits within the 2σ (see Figure 4). When using the θ_E and t_E constraints only without our Keck measurements, the large parallax determined by Udalski et al. (2018) is even less likely. In this case both components lie in the 3σ range.

The parallax estimates are hence consistent with the large θ_E and our Keck measurements, but not very likely. These measurements rely on the measuring the microlensing parallax, $\boldsymbol{\pi}_{\rm E}$, most often from the orbital motion of the Earth (Penny et al. 2016). The component of parallax perpendicular to the Earth's motion ($\pi_{{\rm E},N}$), is degenerate with blending and the orbital motion of the lens and source (the effect on the light curve from these qualities mimics that from orbital parallax, meaning that they are difficult to disentangle

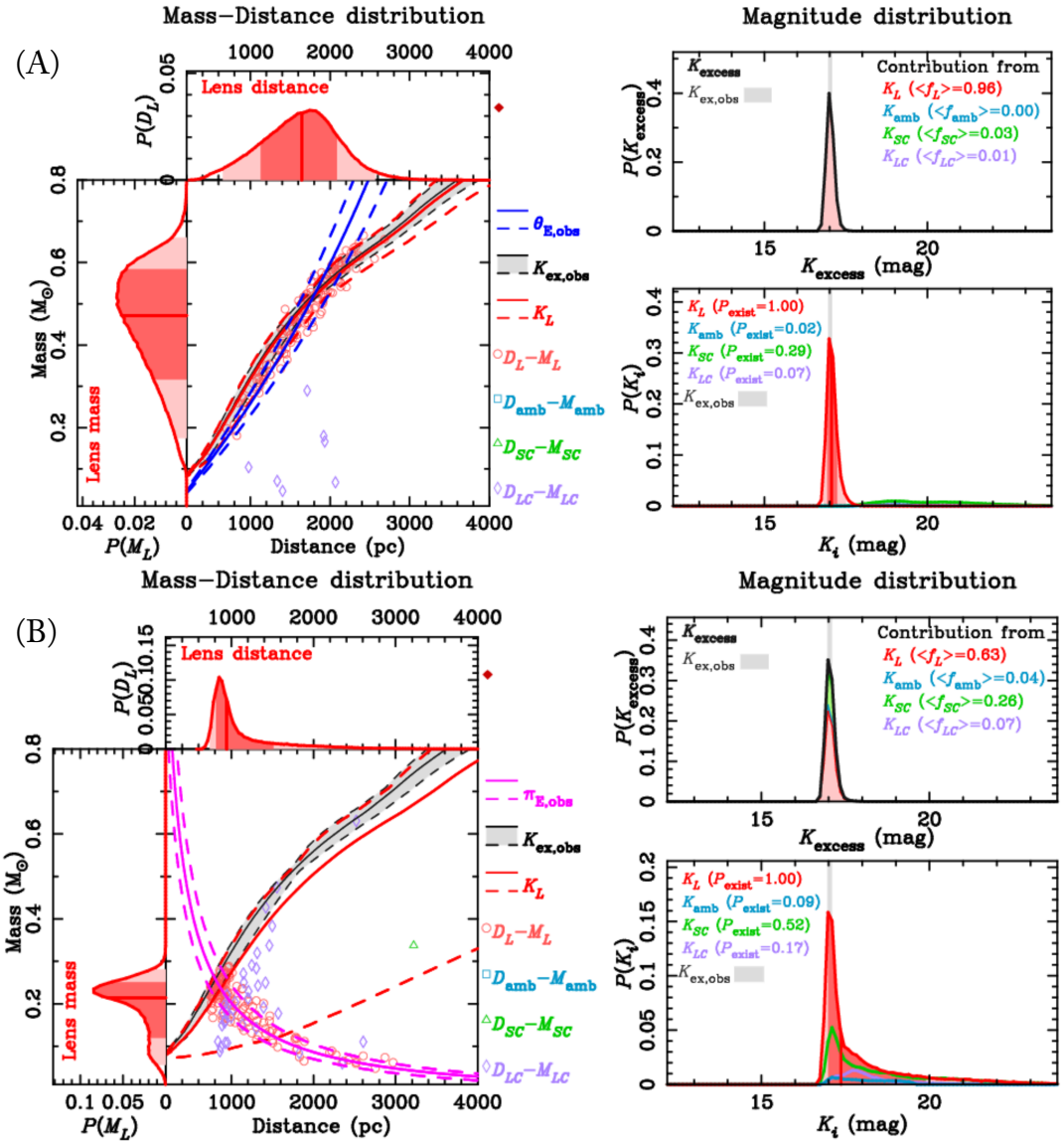

Figure 4.5: Posterior probability distributions showing the predicted mass-distance and magnitude distributions for OGLE-2017-BLG-1434. (A) The mass-distance distributions calculated using a Bayesian analysis with a galactic model prior and constraints from the measured t_E, θ_E and Keck excess flux. The left panel shows 1, 2 and 3σ histogram distributions of the lens mass and distance, with constraints shown for the Einstein ring radius (θ_E) and excess flux $K_{\rm ex}$. The right panel shows the probability of contributions from the lens (K_L), an ambient star ($K_{\rm amb}$), a companion to the source (K_{SC}) and a companion to the lens (K_{LC}). The upper right plot shows the $K_{\rm ex}$ probability distribution, while the lower right shows the probability distributions of each component (K_L, $K_{\rm amb}$, K_{SC}, K_{LC}). In this case the excess flux is most likely from the lens ($K_L = 0.96$). Figure (B) shows the distributions calculated in the same manner as (A), but without the θ_E constraint and including that from parallax, $\pi_{\rm E}$.

from one another). Caution, therefore, must be had when trusting $\boldsymbol{\pi}_{\rm E}$ measurements, in particular for close targets. Penny et al. (2016) cited six planetary events with $D_L < 2\,{\rm kpc}$ of which two could be plausibly be moved to farther distances: OGLE-2013-BLG-0341 and OGLE-2013-BLG-0723. Since that publication OGLE-2013-BLG-0723 has been revealed to be a binary event with no evidence of a planet, while 0341 may have photometry contaminated with systematic errors. In the case of MOA-2007-BLG-192 (Kubas et al. 2012), the detection of a source excess using AO imaging is also consistent with an unrelated source contaminant, rather than solely the lens detection that was claimed.

Parameter	Value	with Keck AO	Udalski et al. (2018)
Lens Distance	D_L (kpc)	0.86 ± 0.05	0.86 ± 0.09
Lens Mass	M_L $(M_\odot)$	0.234 ± 0.012	0.234 ± 0.026
Planet Mass	m_p $(M_\oplus)$	4.43 ± 0.25	4.4 ± 0.5
2D star-planet separation	$a_\perp$ (AU)	1.18 ± 0.10	1.18 ± 0.14

Table 4.6: Table of Physical Parameters of OGLE-2017-BLG-1434

Our Bayesian analysis predicts the system to be a $m_p = 4.43 \pm 0.25\ M_\oplus$ planet orbiting a $M_L = 0.234 \pm 0.012\ M_\odot$ star at a distance of 0.86 ± 0.05 kpc. The updated physical parameters of the lens and its companion calculated using this extra constraint are shown in Table 4.6. The contaminant analysis of (Koshimoto et al. 2020) employed here shows no tension between the reported parallax of Udalski et al. (2018) and our Keck measurements, however the values of parallax determined from the light-curve model (eg. $\boldsymbol{\pi}_{\rm E} = (\pi_{{\rm E},N}, \pi_{{\rm E},E}) = (0.586 \pm 0.081, 0.472 \pm 0.013$ for a parallax+orbital motion fit where $u_0 > 0$) are unlikely and could be the results of systematic errors in the photometry. Excluding the parallax constraints we find that the excess flux at the position of the source is almost certainly the lens (with a probability of 0.96, Figure 4, panel (a)). If we include the parallax (Figure 4, panel (b)) the excess flux is still likely to be the lens ($K_L(<f_L> = 0.63$), but could also be a companion to the source ($K_{SC}(<f_{SC}> = 0.26$).

4.5 Discussion & Conclusion

We obtain Keck follow-up photometry of the microlensing event OGLE-2017-BLG-1434 which is consistent with the physical interpretation of Udalski et al. (2018) of the system being a super-Earth planet orbiting an M-dwarf. When applying the additional constraint on the lens mass and distance from our lens flux measurement we reduced the uncertainty in the lens parameters (mass, distance, planetary mass) by half. As such we can now describe the system as a super Earth at a distance of $0.86 \pm 0.05\,\mathrm{kpc}$, quite nearby, for a microlensing planet. The system is however at a greater distance than the majority of radial velocity and transit-detected planets. The planet and its host star had an instantaneous 2D separation of $a_\perp = 1.18 \pm 0.10$, which places a lower limit on its perihelion distance. When calculating this using the relationship $a_\perp = s\theta_E D_L$ this value is in agreement with that from Udalski et al. (2018), but with an error reduced by 28%. Comparing this to the snow line, defined as $a_{snow} = 2.7\mathrm{AU}\ (M/M_\odot)$, the planet lies at $1.9 \pm 0.2\ \mathrm{a_{snow}}$, while the stellar lens host has a mass of $0.234 \pm 0.012\ \mathrm{M_\odot}$.

This planet joins a list of only 5 others planets detected by microlensing at a distance of less than 1 kpc, assuming no systematic errors in the photometry (as discussed in Section 4.4.3). Of the 100 or so planets so far detected using microlensing, the median distance of these systems, almost all in the direction of the galactic centre, is ~ 5.7 kpc[3]. With a metallicity gradient in the Milky Way disk of -0.05 ± 0.01 dex/kpc (Shaver et al. 1983), this means the lens star is ~ 0.25 dex less metal rich than the usual microlensing host, closer to that of most planetary hosts detected by transits or radial velocity.

While OGLE-2017-BLG-1434 is one of five microlensing planets with a mass ratio of $q \leqslant 0.6 \times 10^{-4}$ and one of 11 planets with a mass between $1 - 10 M_\oplus$, it lies right on the break of the exoplanet mass-ratio power-law according to Jung et al. (2019), which is smooth and decreasing at mass ratios higher than this inflection point, and increasing

[3] https://exoplanetarchive.ipac.caltech.edu/

below. The slope at these smaller mass ratios is not well well constrained with Jung et al. (2019) citing a ∼3.6 times sharper break at the inflection point of the mass-ratio function than Suzuki et al. (2016). The main limitation to determining the slope and shape of the low-q mass-ratio function is simply the lack of statistics in this region. However, the confirmation of this planet does imply that scaled ice-giant systems with Neptune mass ratios such as this are common, in particular compared to those with $q < 0.4 \times 10^{-4}$ which, barring a gulf in microlensing sensitivity in this portion of parameters space (Udalski et al. 2018), has so far yielded no detections.

Lens flux measurements such as those presented here require high-resolution imaging from the largest ground based telescopes (or from the Hubble Space Telescope), however the time cost for each event is low (30-40 mins excluding calibration overhead). While determining the centroid shift or, better, resolving the lens and source is an ideal outcome (Vandorou et al. 2020), that opportunity requires sufficient time between the event peak and the follow-up observations, often between 5-10 years. Especially for events with limited secondary light-curve effects and physical parameters only determined to 30-40%, single band near infrared follow-up photometry as shown here is a time cheap way of tightening mass and distance constraints on microlensing systems.

4.6 Acknowledgements

This work was supported by the University of Tasmania through the UTAS Foundation and the endowed Warren Chair in Astronomy. It was also supported by ANR COLD-WORLDS (ANR-18-CE31-0002) at Le Centre National de la Recherche Scientifique (CNRS) in Paris and the Laboratoire d'astrophysique de Bordeaux. DPB and AB were supported by NASA through grant NASA-80NSSC18K0274. Data presented in this work was obtained at the W. M. Keck Observatory from telescope time allocated to the National Aeronautics and Space Administration through the agencies scientific partner-

ship with the California Institute of Technology and the University of California. These Keck Telescope observations and analysis were supported by a NASA Keck PI Data Award, administered by the NASA Exoplanet Science Institute. The Observatory was made possible by the generous financial support of the W. M. Keck Foundation. This research has made use of the NASA Exoplanet Archive, which is operated by the California Institute of Technology, under contract with the National Aeronautics and Space Administration under the Exoplanet Exploration Program.

5

MOA-2010-BLG-477Lb

A Planetary Survivor of Its Host Star's Demise

In this chapter I present my paper on the microlensing event MOA-2010-BLG-477Lb submitted to the journal Nature. This paper presents the discovery of the first single white dwarf star orbited by a gas giant planet using Adaptive Optics (AO) observations from Keck. Below I offer some introductory comments regarding the context of this paper,

followed by a statement of author contributions. The paper is modified from its journal format to be more consistent with the rest of the thesis. Note that compared to the other two papers presented here, the main text in Section 5.3 is written in a more general style to suit the style of the journal.

5.1 Background & Context

While a concerted effort was made in the late 20th century to search for planets around other Sun-like stars, the first discovered exoplanet actually orbited a neutron star. This seminal discovery of three planets around the millisecond pulsar PSR B1257+12 (Wolszczan & Frail 1992) heralded the era of exoplanet discovery, and yet almost all planets discovered since then orbited stellar objects on the main-sequence. With over 90% of main-sequence exoplanet hosts predicted to become white dwarfs (WDs), understanding post main-sequence planet evolution will be critical to understanding the future planetary landscape of the Milky Way.

Many observations of post-main sequence objects have been made, with ∼100 planets detected around sub-giants and ∼40 white dwarfs containing pollution in their protoplanetary discs implying the presence of planetesimals (Farihi 2016). Of these there are two candidates for single WDs hosting planets. The first is Wd 0806-661,b (Luhman et al. 2011) which is interpreted to either be a giant $7M_{\rm Jup}$ planet or a sub-brown dwarf. It exists at a large 2500AU orbit and is a strong candidate for the coolest known brown dwarf. The second candidate, WD 1145+017 (Gänsicke et al. 2019b), has dust disk chemistry unlike any other debris so far detected around WD (including hydrogen, oxygen and sulfur), which the authors' interpret as a giant planet orbiting the WD at $15R_{\odot}$.

While these possibilities are tantalizing, the main problem with outright detection of planets orbiting white dwarfs is the faintness of the host. As already mentioned, microlensing has the advantage that it does not depend on the brightness of the host and is therefore

sensitive to planets around white dwarfs, free-floating planets and black hole candidates. The microlensing event MOA 2011-BLG-262 (Bennett et al. 2014) found a measured blend flux of $H_b = 18.15 \pm 0.07$ which was compatible with the predicted source flux of $H_s = 18.22 \pm 0.04$. The possible lack of excess flux due to the lens is consistent to a dark lens with a brightness below the Keck detection limit. In this case this limit was determined to be $H_L \leqslant 21.06 \pm 1.0$. However, even if a dark lens were confirmed, the drawback in the lack of dependence on lens brightness is the inability to place constraints on the mass-distance of the lens beyond a magnitude upper limit.

The discovery paper of the high magnification event MOA 2010-BLG-477 reported the detection of a giant planet $m_p = 1.5^{-0.3}_{+0.8} M_{\rm Jup}$ at $\sim 2.3 \pm 0.6$ kpc (Bachelet et al. 2012). They note an unambiguous detection of microlens parallax and orbital motion. However, as is common with microlens light curve analyses, there is a degeneracy between these two quantities (Batista et al. 2011; Skowron et al. 2011), in particular with between component of $\boldsymbol{\pi}_E$ perpendicular to the projected position of the sun, $\boldsymbol{\pi}_{E,\perp}$ and the component of orbital motion perpendicular to the planet-star axis, ω. However, as we do in the paper to follow, we are able to place an upper limit on $\boldsymbol{\pi}_E$ using the measurement of the Einstein Ring Radius, θ_E from the light curve and using the relation:

$$\frac{M}{M_\odot} = \frac{\theta_E}{\kappa M_\odot \mathrm{mas}} \tag{5.1}$$

In the following sections we revise a Bayesian analysis using galactic model priors (Sumi et al. 2011) and find a lower mass limit on the host lens. Like the original study, however, we cannot place an upper limit on the lens mass (low $\boldsymbol{\pi}_E$) since the parallax contours pass through the origin.

The following study makes use of Keck data I and our collaborators obtained over three epochs. It's the combination of data over this three year period that allows us to draw the conclusion the this event contains dark lens and very likely the first single white dwarf de-

tected hosting a gas giant planet.

5.2 Author Contributions

- Observations were made at the Keck Observatory on Mauna Kea, Hawaii in 2015, 2016 and 2018 as part of proposals led by David Bennett.
- All data-reduction and light-curve fitting was performed by Joshua Blackman using `Sextractor`, `Swarp`, and a `Python` pipeline written by Joshua Blackman (80%) and Aikaterini Vandorou (20%).
- Analysis was performed by Joshua Blackman alongside substantial discussion with Jean-Philippe Beaulieu, David Bennett, Andrew Cole and Camilla Danielski.
- The Markov-Chain Monte Carlo estimates subsequently used by Joshua Blackman to create Figure 5.3, was written and performed by David Bennett.
- The point-spread function (PSF) fitting code used to create Figure 5.5 was written by Christophe Alard.
- The remaining figures and text were written and created by Joshua Blackman with suggestions and corrections provided by Jean-Philippe Beaulieu, Andrew Cole and David Bennett.

A Planetary Survivor of Its Host Star's Demise

ABSTRACT

Recent studies (Vanderburg et al. 2015; Manser et al. 2019) have shown that remnants of destroyed planets and debris-disk planetesimals can survive the volatile evolution of their host stars into white dwarfs (Villaver & Livio 2007; Duncan & Lissauer 1998). Approximately 50 of these stellar remnants are known to possess close-in disks (Gänsicke et al. 2019a), with observational evidence for accreted circumstellar debris (Zuckerman et al. 2010; Koester et al. 2014) and dust (Farihi 2016). Planets in Jupiter-like orbits (Mustill et al. 2018; Nordhaus & Spiegel 2013) around stars of 8 solar masses are expected to survive stellar evolution with only a shift to a wider orbit, however no such planets have yet been observed. We report on the discovery of a white dwarf star hosting a bound gas giant planet in the microlensing event MOA-2010-BLG-477Lb. Using near-infrared observations from the Keck Observatory we determine the system contains a $\sim$0.6 solar mass white dwarf host orbited by a $\sim$1.4 Jupiter mass planet with a similar orbital separation to Jupiter. This system is evidence that planets around white dwarfs can survive the giant and asymptotic giant phases of their host's evolution. Located at $\sim$2.0 kpc toward the center of our Galaxy, it likely represents an analog to the end stages of the Sun and Jupiter in our own Solar System.

5.3 Main Text

Most of the 4000 planets detected to date orbit main sequence stars, while some have been found around pulsars (Wolszczan & Frail 1992). Detection of planets orbiting white dwarfs remains challenging because of their low brightness, the low probability of transit detection due to their small radius (Xu et al. 2015), and a dearth of spectral lines which makes them difficult to detect with radial velocity measurements. Detection of intact plan-

etary bodies around white dwarfs are few and include a circumbinary pulsar companion (Sigurdsson et al. 2003) and a spectroscopic analysis of the circumstellar disk around a volatile-rich white dwarf (Gänsicke et al. 2019b). However planets and planetesimals in short period orbits around white dwarfs involve more complicated formation scenarios than that of planets in wider orbits. The detection of planets in wide orbits around white dwarfs would provide cleaner tests of planet formation near white dwarf progenitors.

Here we report on a system composed of a white dwarf hosting a gas giant planet in the microlensing event MOA-2010-BLG-477Lb (Bachelet et al. 2012). The gravitational microlensing technique used to detect this object is sensitive to cold planets down to the mass of Earth (Bennett & Rhie 1996). It can probe objects around all kinds of stars, including white dwarfs, as unlike other detection methods it does not rely on the light coming from the host. The modeling of microlensing light curves gives the planet-host mass-ratio q, and their projected separation s, with good precision in units of Einstein ring radius (the characteristic length scale used to describe microlensing events). Physical parameters can however often only be estimated using a Bayesian analysis that must assume stellar planet-hosting probability.

Fortunately there are three types of additional observations that can be used to place complementary constraints on the mass-distance of the lens host and its companion(s). The first involves determining the finite size of the source to measure the lens-source relative proper motion and the angular Einstein ring radius (Pejcha & Heyrovský 2009). The second is the microlensing parallax effect, which can detected from light curve perturbations due to the orbital motion of the Earth (Alcock et al. 1995) or observations from a satellite in heliocentric orbit (Dong et al. 2007). The third involves measuring the flux of the lens by using high angular resolution follow-up observations which separate the source and lens from unrelated stars on sub-arcsecond scales. In this last case a measurement of the amplitude and direction of the relative source-lens proper motion, typically between

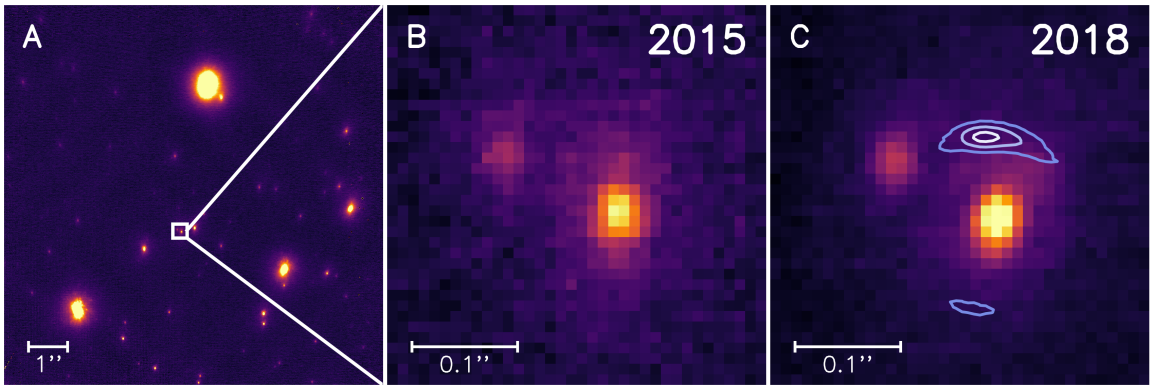

Figure 5.1: H-band adaptive optics imaging from the KECK observatory, with contours showing the predicted position of a main sequence lens. (**a**) A crop of a narrow-camera H-band image obtained with the NIRC2 imager in 2015 centered on MOA 2010-BLG-477 with an 8 arcsec field of view. (**b**) A 0.36 arcsec zoom of the same image. The bright object in the center is the source and a bright, very well aligned companion. To the north-east (the upper left) is an unrelated $H = 18.52 \pm 0.05$ star 123 mas from the source. (**c**) The field in 2018. The contours indicate the likely positions of a possible main sequence host (probability of 0.393, 0.865, 0.989 from light to dark blue) using constraints from microlensing parallax and lens-source relative proper motion.

$3 - 10$ milliarcsec/year, combined with the microlensing parallax information can provide direct mass measurements of the lens star and planet(s) (Bhattacharya et al. 2018).

We have performed follow-up adaptive optics observations with the NIRC2 imager on the Keck-II telescope on Mauna Kea in the period 2013-2019 on many of the planetary systems discovered by microlensing. The microlensing event MOA-2010-BLG-477Lb is a planetary event with a planet-host mass ratio of $q = (2.20 \pm 0.05) \times 10^{-3}$ and a large Einstein ring radius $\theta_E = 1.37 \pm 0.07$ mas, which implies a relatively massive or nearby host star. A Bayesian analysis assuming a main sequence host star predicts a host star with mass of $M_* = 0.67^{+0.33}_{-0.13} M_\odot$, orbited by a planet with mass $m_p = 1.5^{+0.8}_{-0.3}\ M_{\rm Jup}$, at a distance of $D = 2.3 \pm 0.6$ kpc if all stellar types are equally likely to host the planet. The source radius crossing time, measured from light curve finite source effects and the source magnitude and color (Boyajian et al. 2014) yields a lens-source relative proper motion of $\mu_{rel,G} = 10.66 \pm 0.55\,{\rm mas/yr}$. This prediction, presented here in the geocentric reference frame that moves with the Earth's velocity at the time of the event, allows us to estimate the future lens-source separation.

The target was observed with the Keck-II telescope's NIRC2 instrument on July 27, 2015, August 5, 2016 and May 23, 2018 in the H and K_s near-infrared bands ($1-2.4\,\mu$m) using laser guide star adaptive optics. Data were obtained using the NIRC2 wide camera for calibration and the narrow camera with a 10 arcsec field-of-view in an attempt to resolve the source and lens. In our images we note a $H = 18.52 \pm 0.05$ star located $\sim$123 mas to the north-east (upper-left in Fig. 5.1c) of the source. Given the large lens-source relative proper motion, a predicted separation of $53\,\mathrm{mas}$ means the lens star should be detectable under ideal observing conditions 4.96 years after the event peak in 2015. By 2018, this separation will have widened to $83\,\mathrm{mas}$. We find that the separation of the $\sim$123 mas star to the north east has actually decreased by $11.5\,\mathrm{mas}$ between 2015 and 2018, instead of the expected $30\,\mathrm{mas}$ increase. This indicates that this object is unrelated to the lens and the planetary system.

The predicted dereddened source magnitude of $H_s = 17.32 \pm 0.03$ and $K_s = 17.17 \pm 0.04$ was determined using data from the Cerro Tololo Inter-American Observatory (CTIO) and the Vista Variables in the Via Lactea (VVV) survey. This brightness is compatible with our NIRC2/KECK images and the flux-ratio between the unrelated $\sim$123 mas companion and the star at the position of the source. This is consistent with no excess flux within the point spread function (PSF) of the source star. To confirm this, we model the PSF with the addition of weak contributions from the wings of the unrelated companion, and find no significant structure in the residuals. Hence, with no evidence of a detectable lens in our Keck/NIRC2 images, the lens star — which must exist by virtue of the microlensing event — must have a brightness below the detection limit.

To determine this limit we define a detection to be above the noise at the 3σ level. This corresponds to a threshold of $\mathrm{H} < 21.1$, which means that any object brighter than this value should be detectable within our Keck narrow frames. The light curve of this event indicates a clear microlensing parallax signal due to the orbital motion of the Earth, but the

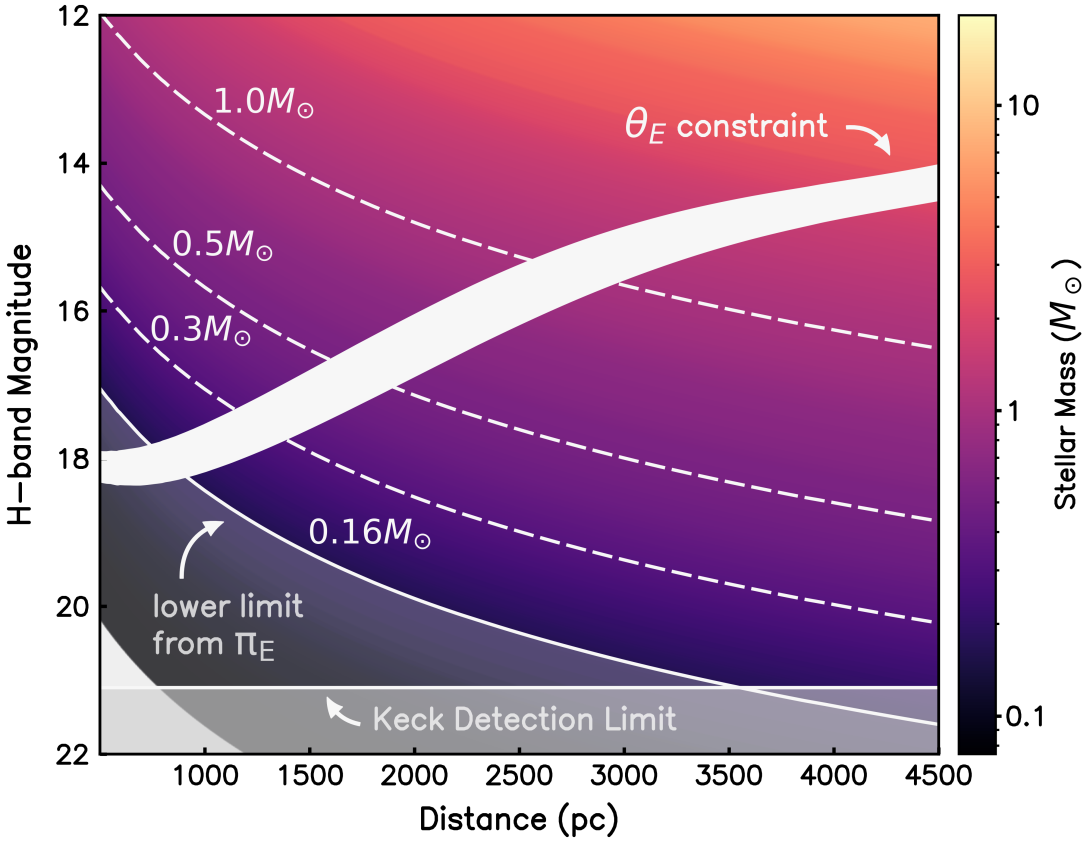

Figure 5.2: H-band brightness of possible main-sequence host lenses for the microlensing event MOA-2010-BLG-477Lb for varying stellar mass. In white is the Einstein ring radius, θ_E constraint derived from finite source effects in the event light curve. This constraint indicates that if the planet host star was main-sequence, it should be visible with Keck adaptive optics as the entire area lies above the detection threshold of our H-band images at H∼21.1. The mass-luminosity relations for different main-sequence lens masses are shown: $1.0M_\odot$, $0.5M_\odot$, $0.3M_\odot$, with $0.16M_\odot$ the mass lower limit derived from the microlens parallax, π_E. Our null detection in our Keck images implies that the exoplanet host must be a stellar remnant, most likely a white dwarf.

2-dimensional microlensing parallax vector, π_E, is not fully constrained. This implies that for each model in the microlensing discovery paper's (Bachelet et al. 2012) Markov Chain distribution, we can determine the lens mass $M_L = (c^2/4G)(\theta_E/\pi_E)$ (Gaudi 2012), where π_E is the length of the 2-dimensional microlensing parallax vector. We combine these light curve constraints with limits on the source and lens distances and velocities, together with an empirical mass-luminosity relation (Bennett et al. 2014), and using a Bayesian analysis find that a main-sequence lens star must have a brightness of $H < 18.10$ at 99.0% confidence. This is largely due to the light curve constraint on the angular Einstein ring radius,

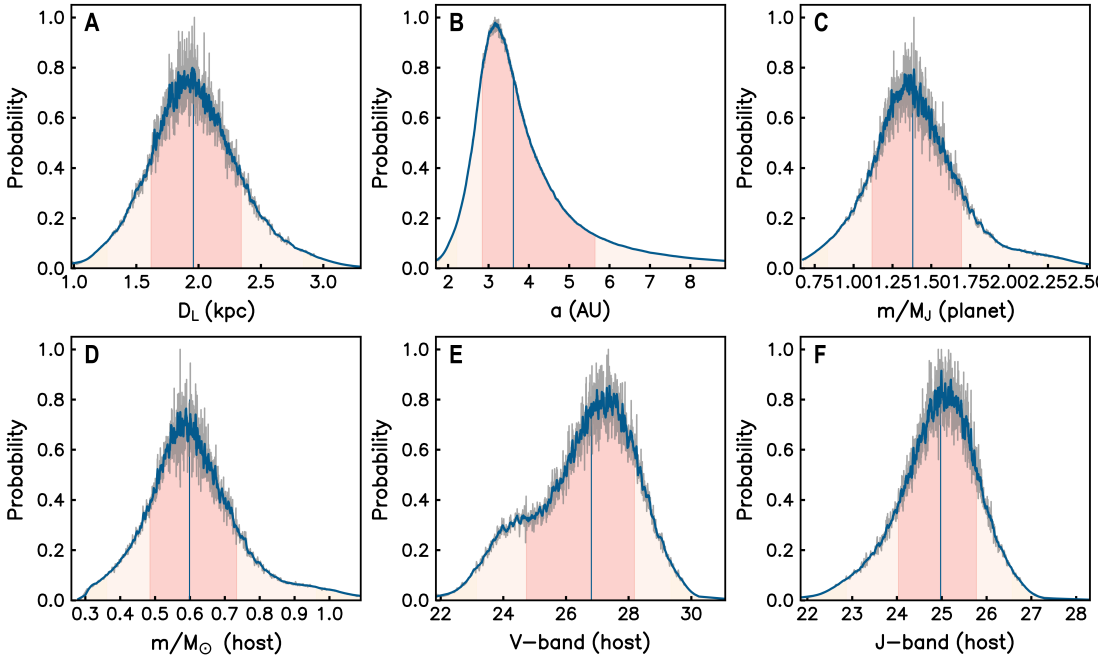

Figure 5.3: Probability distributions of system physical parameters derived from a Bayesian analysis. Presented here is the predicted distance to the host star/lens planetary system (**a**), 3d star-planet separation (**b**), mass of the planet (**c**), mass of the host star (**d**) and the predicted host star brightness in V and J-filters (**e** and **f**).

θ_E, derived from the source angular radius and crossing time.

The microlensing parallax and lens-source relative proper motion measurements constrain the location of a main sequence lens star to the interior of the contours in Fig. 5.1c. The predicted brightness of a main sequence lens as a function of lens distance can be seen in Fig. 5.2. Since all possible main-sequence lenses for the event are brighter than the Keck detection limit, and no such star is observed, the lens cannot be a main-sequence star. This same analysis also excludes brown dwarf lenses due to an upper limit on the microlensing parallax parameter, $\pi_E < 1.02$. The implied limit on the lens system mass is $M_L > 0.16 M_\odot$, and this rules out brown dwarf lenses. With main sequence stars and brown dwarfs ruled out, we conclude that the lens must be a stellar remnant: a white dwarf, neutron star or a black hole. Of these, a white dwarf is the most likely: 97% of stars in the Galaxy will end their lives as white dwarfs, and large companion planets are expected to survive the demise of their stellar hosts (Nordhaus & Spiegel 2013; Veras 2016).

Parameter	Units	Value	2σ range
White Dwarf Lens Distance	D_L (kpc)	1.96 ± 0.40	1.39–2.65
White Dwarf Lens Mass	M_L ($M_\odot$)	0.60 ± 0.14	0.40–0.87
Planet Mass	m_p (M_J)	1.38 ± 0.36	0.93–2.02
Source Star Distance	D_S (kpc)	7.9 ± 1.3	5.7-10
2D star-planet separation	$a_\perp$ (AU)	3.0 ± 0.6	2.18–3.98
3D star-planet separation	a (AU)	$3.6^{+2.0}_{-0.8}$	2.44–9.41
Mass Ratio	q (10^{-3})	2.20 ± 0.05	1.02-4.83
White Dwarf Host V_L	mag	26.81 ± 1.72	26.63–28.95
White Dwarf Host J_L	mag	24.98 ± 0.87	23.29–26.29

Table 5.4: Table of Physical Parameters for MOA 2010-BLG-477L,b

Compared with the predictions of planets and planetesimals orbiting white dwarfs, neutron star planets are rare. Only two detections have been made, and a study of 151 pulsars younger than 2 Myr yielded no planet detection with $m_p > 0.4 M_\oplus$ (Kerr et al. (2015), where the mass of the Earth is $M_\oplus = 5.97 \times 10^{24}$; kg). Meanwhile, post-supernova fallback accretion discs have been modelled to dissipate in < 0.1 Myr, meaning that gas giants are unlikely to form (Currie & Hansen 2007). The possibility of planets orbiting black holes is minor, though models of dust growth suggest planets could form in debris disks 0.1-100 pc around supermassive black holes (Wada et al. 2019). The slim possibility of a neutron star or black hole host star could be tested by deep follow-up observations with Hubble Space Telescope and the James Webb Space Telescope.

To estimate the properties of a white dwarf host, we use a complete sample of 130 white dwarfs within 20 pc (Giammichele et al. 2012), excluding unresolved double white dwarfs and double white dwarfs candidates identified by Toonen et al. (2017), and perform a Bayesian analysis with the Galactic model from (Bennett et al. 2014). This calculation was made under the assumption that all white dwarfs are equally likely to host planets. Our results are summarized in Fig. 5.3 and Table. 5.4. We find a likely white dwarf host mass $M = 0.60 \pm 0.14$ M$_\odot$, which sits at the peak of the single white dwarf mass distribution (i.e. 0.6 M$_\odot$). This implies a Jovian planet of mass $m_p = 1.38 \pm 0.36$ M$_J$ at a distance of

$D_L = 1.96 \pm 0.40\,\mathrm{kpc}$.

With a projected separation of $a_\perp = 3.0 \pm 0.6$ AU and an estimated 3-dimensional separation of $a = 3.6^{+2.0}_{-0.8}$ AU (assuming a random orientation), it is likely that the planet MOA-2010-BLG-477Lb formed at the same time as the host star and managed to survive the post-main-sequence evolution. The mass loss experienced by a star on the giant and asymptotic giant branches pushes the planet toward a wider orbit, but tidal forces can have the opposite effect when the star expands to radii 1 AU (Veras 2016). In rare cases, the tidal effect can nearly cancel the mass loss effect, leaving a giant planet orbiting at a separation as small as ~ 2 AU, but this requires a fine tuning of parameters to prevent the planet from being engulfed by the star. The vast majority of white dwarfs in the Galactic disk are thought to have formed from stars with initial masses of 1–2 $M_\odot$, and Jovian planets orbiting these stars are generally thought to move to orbital separations > 5 or 6 AU around the remnant white dwarfs (Mustill & Villaver 2012; Nordhaus & Spiegel 2013).

MOA-2010-BLG-477Lb is one of 30 planets (from 29 events) in recent statistical sample of microlensing events (Suzuki et al. 2016). Seven of these have a faint source and a large θ_E, which guarantees almost certain detection of a main sequence host star with our Keck follow-up imaging program. With 20% of microlensing events thought to be caused by white dwarfs, it is reasonable to expect that 1 or 2 of these 7 events would have a white dwarf primary lens. However, these 7 events are events with detected planets, and white dwarf planets are generally thought to have orbital separations considerably larger than the 3.0 ± 0.6 AU projected separation of MOA-2010-BLG-477Lb, where microlensing has the highest sensitivity. The reduced detection probability for white dwarf planets might be compensated for by a higher intrinsic planet occurrence for gas giant planets around massive stars (Ghezzi et al. 2018). A single detection of a white dwarf planet host does not allow us to make a definitive statement about planet occurrence rates for white dwarf hosts, however this will be possible with the advent of the Galactic Exoplanet Survey of the

Nancy Grace Roman Space Telescope (Penny et al. 2019), which should detect hundreds of such planets.

5.4 Methods

5.4.1 Observations

The microlensing event MOA 2010-BLG-477 was originally detected using the 1.8m telescope at Mt. John Observatory in New Zealand on August 2, 2010, and subsequently observed by more than 20 telescopes (Bachelet et al. 2012). In order to find the predicted magnitude of the source star we refer to the H-band light curve obtained by the μFUN 1.3 m SMARTS telescope at the Cerro Tololo Inter-American Observatory (CTIO). We calibrate the light curve according to data from the VVV (Vista Variables in the Via Lactea) survey. Using a single amplified CTIO H-band frame with an epoch corresponding to available VVV data, we cross identify between the two. We derive a source magnitude of $H_{CTIO,source} = 17.32 \pm 0.03$. Given the source color of $H-K = 0.07$, and using extinction corrections derived using the OGLE extinction calculator, $A_H = 0.21$ and $A_K = 0.13$, we find $K_{CTIO,source} = 17.17 \pm 0.04$.

Located at $(\alpha, \delta) = (18^h06^m07^s.47, -31^\circ27'16.17$, J2000.0), we observed the event using the NIRC2 instrument on the Keck II telescope located on Mauna Kea (Hawaii) with laser guide star adaptive optics (LGSAO). Seven dithered H-band images were obtained with the narrow camera on 2015 July 27 (HJD = 2457230.7), 4.96 years following the event peak. These images have a median full width at half maximum (FWHM) of 50 mas. During this same epoch we obtained 14 wide camera 95 mas K_s-band images and 10 narrow camera 50 mas H-band images. The event was observed twice more: in 2016 with 17 H-band 50 mas narrow images and two H-band 90 mas wide, and in 2018 with 16 50mas K_s-band narrow frames. These final 2018 observations were taken on 23 May 2018 (HJD= 2458262.4), 7.78 years after maximum magnification. The goal of these

observations was to determine the composition of the source-lens blend by obtaining a refined photometric and astrometric solution. We apply flat-field and dark-field corrections using standard techniques (Blackman et al. 2020; Beaulieu et al. 2016). The images were stacked using SWARP (Bertin & Emmanuel 2010). We identify the source+lens star as indicated in Fig. 5.1 and Fig. 5.1. Comparing this with the OGLE-III reference image of the BLG 176.8 field in Fig. 5.1 we see that the OGLE star is a blend of four dimmer stars, the second brightest of which is the source+lens star. The OGLE star (number 119416) has an I-band magnitude of $I = 17.446 \pm 0.052$, which is consistent with the value of $I = 17.443 \pm 0.031$ from DoPhot CTIO photometry (Bachelet et al. 2012).

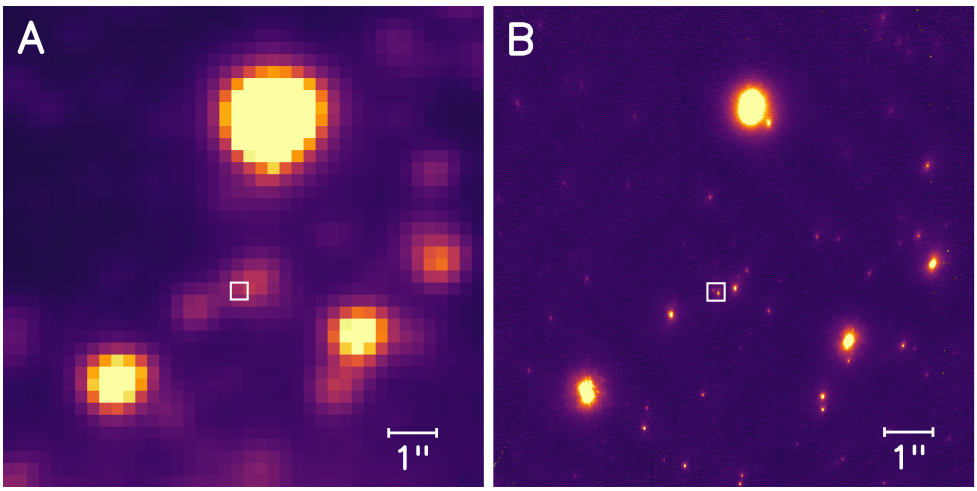

Figure 5.1: OGLE-III and Keck imaging of MOA-2010-BLG-477Lb. (**a**) OGLE-III image of the OGLE-BLG176.8 field (**b**) H-band image of the same field taken in 2015 with Keck/NIRC2 with the narrow camera.

We perform aperture photometry using SExtractor on the wide K-band frame from 2015, finding an K-band magnitude of the blend at the position of the source to be $K_{Blend} = 16.78 \pm 0.03$. The magnitude is the combination of the flux from the source, the lens and the 123mas star located to the north-east. Fortunately, data of this field was also captured as part of the VVV survey while the event was still magnified. Data were obtained from

the Vista telescope in JHK at the epochs:

$$\begin{aligned} \mathrm{H, MJD-OBS} &= 55423.15153784 \\ \mathrm{J, MJD-OBS} &= 55423.15769162 \\ \mathrm{K, MJD-OBS} &= 55423.15466181 \end{aligned} \tag{5.2}$$

The point spread function of the VVV image is a combination of the source, the lens, the 123 mas star to the north-east (upper left) and the star to the North-West (upper right). The amplification of this target was 19.27 in H at $\mathrm{MJD-OBS} = 55423.15153784$ where MJD = JD - 2400000.5. Using extinction corrections of $A_J = 0.38$, $A_H = 0.21$ and $A_K = 0.13$ we determine the amplified magnitude of the source star to be $J_0 = 14.12 \pm 0.01$, $H_0 = 13.79 \pm 0.01$ and $K_0 = 13.77 \pm 0.01$.

From the K-band VVV light curve we find a 12-15% modulation in brightness, greater than the predicted 6% from scatter. A periodogram indicates that the North-West star is a variable star with a period of 11-days. This detection cannot be of the north-east 123 mas star as it is too faint in the VVV data, nor can it be the star at the position of the source as we do not see it in the microlensing light-curve data. The existence of a variable star and the close 123 mas neighbour complicates our approach to the photometry. In analyzing our Keck image we instead compare the flux ratios between the star at the position of the source and the 123 mas companion, and compare that to a calibrated wide Keck frame and that determined by CTIO/VVV.

In our Keck wide image we crossmatch to stars in the VVV catalog (Minniti et al. 2010). Both the wide and narrow cameras on NIRC2 result in an image with dimensions of 1048 × 1048 pixels. The wide has a field of view (FOV) of 40 arcseconds while the narrow has a FOV of 10 arcseconds. The narrow images were taken in sequence with a dither of 0.7

arcseconds. The flux ratio of between the source star and the 123 mas companion is:

$$\begin{aligned} 2018, \mathrm{K} &= 0.42 \\ 2015, \mathrm{H} &= 0.33 \\ 2016, \mathrm{H} &= 0.34 \end{aligned} \tag{5.3}$$

Using the flux ratio from the 2018 K data and the predicted source K brightness of $K_s = 17.17 \pm 0.04$, we determine the sum of the source and the 123 mas companion to be $K = 16.79 \pm 0.04$, which is compatible with the the $K_{Blend} = 16.78 \pm 0.03$. determined from only the 2015 Keck wide co-added frame. This indicates that the there is no additional flux at the position of the source, and that all the photons from that object come from the source.

Bayesian Analysis Light Curve and Galactic Models

Our analysis makes use of the light curve models from the Markov Chain calculation of the MOA-2010-BLG-477Lb discovery paper (Bachelet et al. 2012). These models incorporated the effects of the orbital motion of the Earth which are responsible for the microlensing parallax effect, as well as the orbital motion of the planet. The microlensing parallax is a two-dimensional vector parallel to the lens-source relative proper motion, which means the distribution of microlensing parallax vectors from the light curve models constrains the direction of the lens-source relative proper motion. The amplitude of the lens-source relative proper motion vector is determined by finite source effects in the microlensing light curve. However, the direction and length of this lens-source relative proper motion vectors are not determined in the Heliocentric reference frame that is appropriate for high angular resolution Keck follow-up observations. The light curve models employ a Geocentric reference frame that moves with the velocity of the Earth at

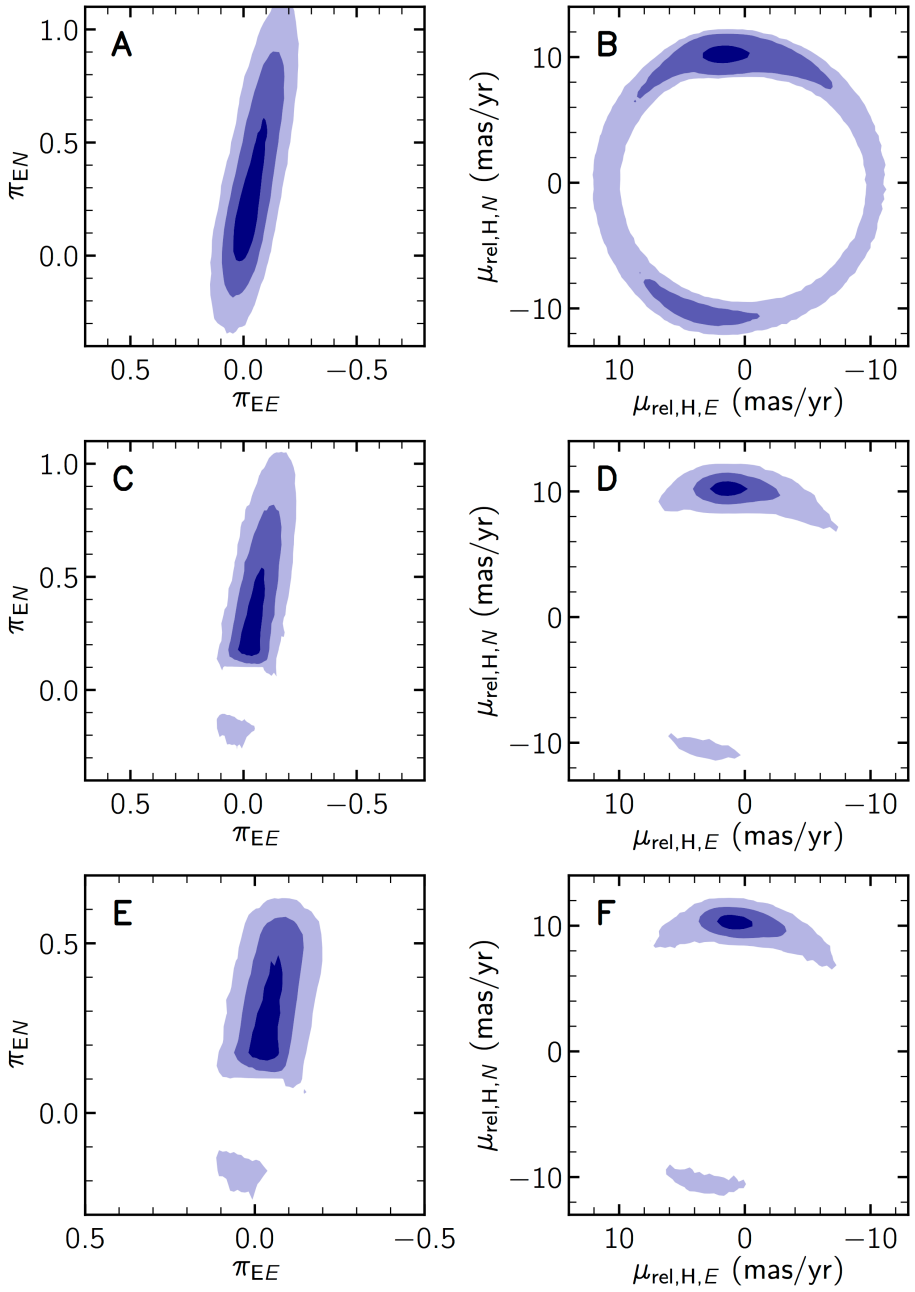

Figure 5.2: Predictions of the microlens parallax vector π_E and the corresponding predicted relative lens-source proper motion μ_{rel} for a main sequence and white dwarf lens. Based on a Markov-Chain Monte-Carlo (MCMC) analysis using Galactic model priors as in Bennett et al. (2014), the upper panels (**a**) and (**b**) show the unweighted predicted components of (π_{EN}, π_{EE}) and $(\mu_{rel,HN}, \mu_{rel,HE})$. The middle panels (**c**) and (**d**) show the weighted predictions for a main-sequence lens. The lower panels (**e**) and (**f**) show the weighted predictions for a white-dwarf lens. The three shades of blue from dark to light denote probabilities of of 0.393, 0.865, 0.989. When integrating over all parameters the limit of the 0.393 contour corresponds to the 1σ distribution of any chosen parameter.

the time of closest lens-source alignment. For MOA-2010-BLG-477Lb, this velocity is $\boldsymbol{v}_{\oplus N,E} = (-2.7933, 19.5634)\,\mathrm{km\,s^{-1}}$, and the transformation to the relative proper motion in the Heliocentric reference frame, $\boldsymbol{\mu}_{\rm rel,H}$, is given by

$$\boldsymbol{\mu}_{\rm rel,H} = \boldsymbol{\mu}_{\rm rel,G} + \frac{\boldsymbol{v}_{\oplus \rm N,E}}{\rm AU}\pi_{\rm rel}\ , \tag{5.4}$$

(Dong et al. 2007; Bhattacharya et al. 2018), where the relative parallax is given by $\pi_{\rm rel} = \mathrm{AU}/D_L - \mathrm{AU}/D_S$. This transformation from $\boldsymbol{\mu}_{\rm rel,G}$ to $\boldsymbol{\mu}_{\rm rel,H}$ cannot be computed with light curve parameters only as $\pi_{\rm rel}$ depends on the source and lens distances. Therefore, we most invoke a Galactic model to properly sample the source distance, D_S, values. We have used the Galactic model from Bennett et al. (2014) in our analysis. Once the source distance is selected, the lens distance can be determined from light curve parameters,

$$D_L = \frac{\rm AU}{\pi_{\rm E}\theta_{\rm E} + \mathrm{AU}/D_S}\ . \tag{5.5}$$

The Galactic model also provides weights for the density of stars at the distance to the lens, D_L, and by the probability of a star with a mass equal to the lens mass. This implicitly includes the assumption that all stars are equally likely to host the planet of the measured mass ratio and projected separation.

Fig. 5.2 shows how the Galactic model affects the distributions of the $\boldsymbol{\pi}_{\rm E}$ and $\boldsymbol{\mu}_{\rm rel,H}$ vectors. Panels 5.2A and 5.2B show the $\boldsymbol{\pi}_{\rm E}$ distribution from the light curve models in (Bachelet et al. 2012) and the implied $\boldsymbol{\mu}_{\rm rel,H}$ distribution, with the help of the D_S distribution from the (Bennett et al. 2014) Galactic model. The component of the $\boldsymbol{\pi}_{\rm E}$ parallel to the direction of the Earth's acceleration during the event is tightly constrained. This component is close to the East direction. The perpendicular component, which is largely in the North-South direction is very weakly constrained, and the distribution of $\boldsymbol{\pi}_{\rm E}$ values runs through the origin, where the magnitude of the microlensing parallax vector $\pi_{\rm E} = 0$,

which would correspond to an infinite lens mass. Panels C and D of Fig. 5.2 show the result when we apply the complete Galactic model including the mass function for main sequence stars. This removes the light curve models with small $\pi_{\rm E}$ values, and therefore, large masses. It was these low-$\pi_{\rm E}$, high-mass light curve models that allowed the $\boldsymbol{\pi}_{\rm E}$ vector to point in any direction. This was responsible for the ring distribution of $\boldsymbol{\mu}_{\rm rel,H}$, but with the high mass lens systems excluded, this ring is broken into two arcs to the North and South, with low-mass lens systems only allowed in the Northern arc. Our Keck observations have ruled out any main sequence stellar lenses in these arcs. Our model does assume that stars with masses above $1.1\,M_\odot$ have left the main sequence, but such stars would also be brighter than the source star, which are clearly ruled out over the full Fig. 5.2B ring.

With main sequence hosts ruled out, we can now turn our attention to white dwarf host stars for the MOA-2010-BLG-477Lb exoplanet. We can repeat the same calculation that we did for main sequence sources. This requires a mass-luminosity distribution for white dwarfs. We construct such a distribution from the 20 pc sample as in (Giammichele et al. 2012), excluding unresolved binary white dwarfs because these are likely to have unreliable parameters. The resulting white dwarf mass-luminosity relation, constructed using a multivariate Gaussian kernel density-estimation is shown in Fig. 5.3. The results of a repeat of the Bayesian analysis with the main sequence mass function replaced by our white dwarf mass function, from Fig. 5.3, is shown in Fig. 5.2 panels D and E. The results are quite similar to the main sequence case, but the exclusion of low-$\pi_{\rm E}$, high-mass light curve models is now somewhat stronger because the white dwarf mass function is strongly peaked around $M_L \sim 0.6 M_\odot$. This Bayesian analysis is also used to produce the lens system properties presented in Table 5.4. The contours from Fig. 5.2D are reproduced in Fig. 5.4C, where they replace the contours for the main sequence stars shown in Fig. 5.1C.

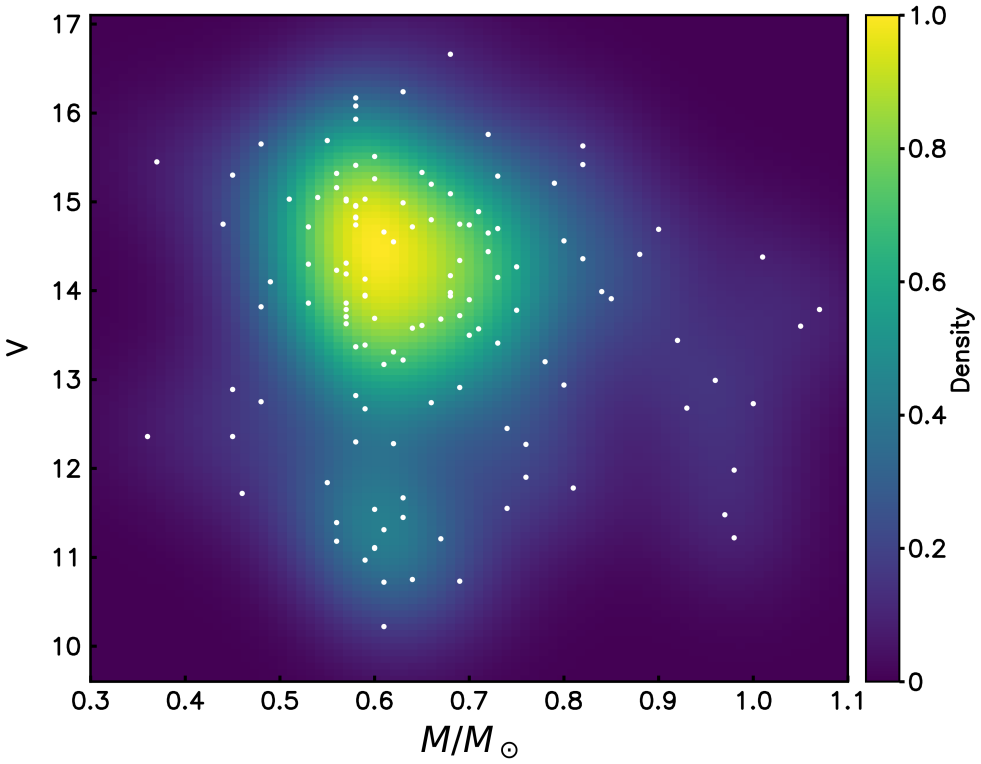

Figure 5.3: White Dwarf Mass-Luminosity distribution derived a sample of 130 white dwarfs from a homogeneous and complete sample of white dwarfs within 20pc of the Sun Giammichele et al. (2012). Two unresolved double-white dwarfs (DWD), eight unresolved DWD candidates and one unresolved binary white dwarf with a main-sequence companion have been removed from this sample (Toonen et al. 2017). 14 stars with distances $>$ 20 pc have also been removed. The white dots indicate the masses and V band magnitudes of the white dwarfs in this sample, and the color distribution indicates the smooth Gaussian multivariate kernel-density distribution that we have used in our analysis.

Detection Limits and Point Spread Function Deconvolution

We determine the detection threshold of our Keck images by estimating the flux of a point source and evaluating the normalized cross-product with the point-spread function (PSF). We obtain this quantity for all points in the subtracted image and construct a map of the amplitudes. In order to obtain an estimate of the fluctuations due to the noise we calculate the standard deviation in this map. We consider that these fluctuations are significant at the 3σ level and that this 3σ level is our detection limit. We then convert this 3σ limit to magnitude and obtain a minimum limit of detection of $H \simeq 21.1$.

While the relative proper motion indicates that the lens is distinct from the PSF of

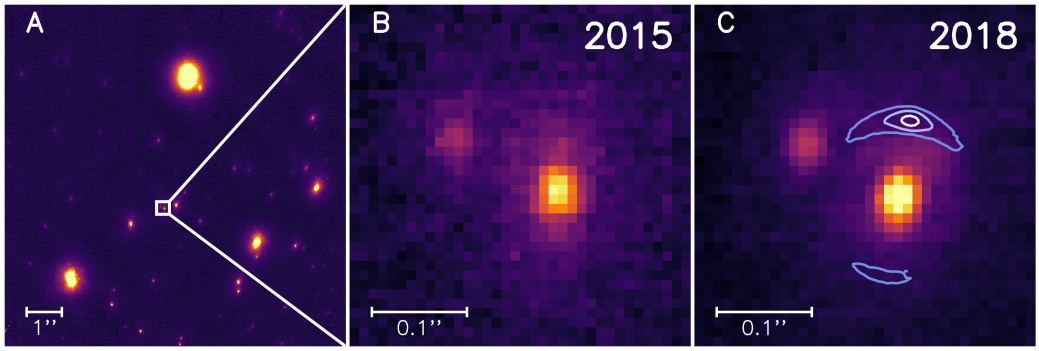

Figure 5.4: H-band adaptive optics imaging from the KECK observatory, with contours showing the predicted position of a white dwarf lens (analogous to Fig. 5.1) (**a**) A crop of a narrow-camera H-band image obtained with the NIRC2 imager in 2015 centered on MOA 2010-BLG-477 with an 8 arcsec field of view. (**b**) A 0.36 arcsec zoom of the same image.The bright object in the center is the source and a bright, very well aligned companion.To the north-east (the upper left) is an unrelated $H = 18.52 \pm 0.05$ star 123 mas from the source. (**c**) The field in 2018. The contours indicate the likely positions of the white dwarf host (probability of 0.393, 0.865, 0.989 from light to dark blue) using constraints from microlensing parallax and lens-source relative proper motion.

the source star, we then perform an analysis to determine if the star at the position of the source is consistent with a single object or if there is evidence of a two component system. To do this we make a numerical estimate of the PSF by stacking the brightest stars in the neighborhood of our target. The accurate position of each PSF is estimated by iterative Gaussian weighted centering. The PSFs are then interpolated, re-centered and stacked, and median solution obtained. In our H-band images the star of interest is quite close to the star to the north-east, which means it may receive some contribution from the PSF wings of its neighbour. To subtract any neighbour contributions we reconstruct the wings of the PSF of the more distant star as a single function of distance and subtract this weak contribution from the image. Then the best solution obtained is subtracted, leaving only the stars of interest. The result of this subtraction and the residuals are presented in Fig. 5.5.

When reconstructing a single star a common problem is to determine whether this star is a single PSF or a very close system of multiple PSFs. If the single PSF fit results in significant residuals, for example, it is clear that the fit of a binary system should be attempted. In this case constraints on the PSF can be used to find upper limits on allowed

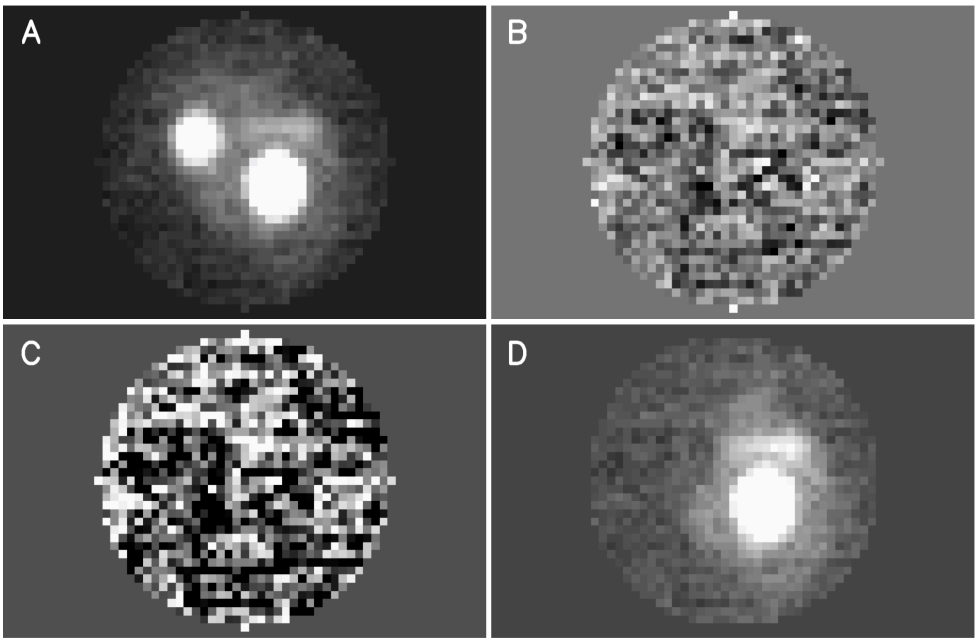

Figure 5.5: Keck Point Spread Function (PSF) fit and residuals. (**a**) Keck/NIRC2 H-band image from 2018. (**b**) Residuals after fitting the PSF of the object at source position (the brighter star to the lower right in panel A) and its unrelated companion. They show no structure or indication of a double object in either of the two stars. The lack of structure in the residuals indicates that the blend from the excess flux of the source companion (within the flux of the brightest star) is very well aligned with the source. (**c**) The residuals from panel B normalized to the Poisson noise. (**d**) Panel A but with the subtraction of the fitted PSF of the unrelated companion.

separations that are compatible with the data and noise. Our method to achieve this and to overcome the degeneracy created when the PSF components are very close are described below.

The image as shown in Fig. 5.5, I_C is the result of the convolution of the object data, I_0 with the PSF, ϕ. Let's consider the case where the un-convolved data I_0 is very narrow with respect to the PSF, which is typical in cases of two close-together stars. In this instance, we can write:

$$I_C(x, y) = \int \phi(x - u, y - v) I_0(u, v) du dv \tag{5.6}$$

Considering that the variations are small with respect to the variations of ϕ, we can

write ϕ as a local expansion in the local variables (u, v):

$$I_C(x,y) \simeq m_0\phi(x,y) - m_1\frac{\partial\phi}{\partial x} - m_2\frac{\partial\phi}{\partial y} + m_3\frac{\partial^2\phi}{\partial x^2} + m_4\frac{\partial^2\phi}{\partial x\partial y} + m_5\frac{\partial^2\phi}{\partial y^2} \tag{5.7}$$

where:

$$\begin{cases} m_0 = \int I_0(u,v)dudv \\ m_1 = \int I_0(u,v)u\ dudv \\ m_2 = \int I_0(u,v)v\ dudv \\ m_3 = \frac{1}{2}\int I_0(u,v)u^2dudv \\ m_4 = \int I_0(u,v)uv\ dudv \\ m_5 = \frac{1}{2}\int I_0(u,v)v^2dudv \end{cases} \tag{5.8}$$

The m_1 and m_2 coefficients represent the degrees of freedom related to the centered of the function I_0. To eliminate these degrees of freedom we make the center of flux of I_0 coincide with the origin of the coordinate system. In this case, $m_1 = 0$ and $m_2 = 0$. As such we are left with an expansion with 4 basis functions, the PSF and its 3 second order derivatives. The moments of the function I_0 are simply the 3 coefficients (m_3, m_4, m_5) normalized by the total flux (Note that provided that the PSF is normalized the total flux and the coefficient m_0 should be very similar).

We use the numerical model of the PSF to reconstruct the derivatives up to the second order. The derivatives are obtained by shifting the PSF model and taking the difference with the original PSF. The value of the shift is small with respect to the size of the PSF grid. We choose a value of 0.01, but also tested 0.1 and 0.001 and no significant changes were observed. In creating the PSF model we take an area around the object large enough to include the PSF wings but small enough to avoid including another object.

Data availability

The KECK Observatory data used in this study are freely available on the Keck Observatory Archive (https://koa.ipac.caltech.edu/cgi-bin/KOA/nph-KOAlogin).

Code availability

The KECK pipeline is available on Github (https://github.com/blackmanjw/KeckPipeline). The Bayesian analysis code of D.P. Bennett is subject to restricted availability.

Acknowledgements

Data presented in this work was obtained at the W. M. Keck Observatory from telescope time allocated to the National Aeronautics and Space Administration through the agencies scientific partnership with the California Institute of Technology and the University of California.

Funding

This work was supported by the University of Tasmania through the UTAS Foundation, ARC grant DP200101909 and the endowed Warren Chair in Astronomy. We acknowledge the support of ANR COLD WORLDS (ANR-18-CE31-0002) at the Institut d'astrophysique de Paris and the Laboratoire d'astrophysique de Bordeaux. EB gratefully acknowledges support from NASA grant 80NSSC19K0291. Work by N.K. is supported by JSPS KAKENHI Grant Number JP18J00897.

Author contributions

J.W.B. led the photometric and formal analysis and wrote the manuscript. J.W.B, V.B. and J.-P.B took and reduced the photometric data using a pipeline written by J.W.B.

and A.V. with contributions from J.-B.M. for magnitude calibrations. D.P.B., J.-P.B and A.A.C discussed conceptual and analysis approaches. D.P.B. was the PI of the KECK telescope proposal, led the planning of the observations, and conducted the light curve modeling and Bayesian analyses. C.D. provided insight into single and double white dwarf planetary systems. A.B. and E.B. assisted with proper motion calculations. A.B. and N.K assisted with observing on Keck. C.R. calculated the parallax, proper motion and lens prediction contours. C.A. worked on the PSF analysis and the determining of detection limits. D.P.B, J.-P.B, A.A.C and C.D. contributed to the review and editing of the manuscript.

Competing interests

The authors have no competing interests to declare.

6

Summary

High-angular resolution follow-up observations of microlensing events are powerful and time-effective way to obtain accurate mass measurements of exoplanets detected with microlensing. Throughout its brief history over the past 7 years more than 60 events have been observed with world class ground-based telescopes such as KECK, SUBARU, VLT and MAGELLAN and the studies presented here are an important step towards regularly obtaining accurate mass measurements of these exoplanets and their hosts, and preparing for the next generation of surveys.

Presented in this thesis are three studies, each focusing on a different aspect of this

technique. In Chapter 3, with the stellar binary MACHO-97-BLG-28, we look at the possibility of resolving the lens and the source 16 years after the event occurred using Keck photometry. I showed this was not possible for this event, and complimented these newly acquired AO data by remodelling the event using a contemporary light-curve analysis approach, arriving at new estimates of the mass and distance of lens and its binary companion. In Chapter 4, we measure the lens flux of OGLE-2017-BLG-1434, showing that with a minimal telescope time adaptive optics observations can be performed soon after a microlensing event in order to obtain a finer estimate of the lens mass and distance. And finally in Chapter 5, we exploit microlensing's independence from the lens star brightness and make the first discovery of a white dwarf with a gas giant companion using Keck AO imaging.

There are a number of future missions poised to take advantage of adaptive optics mass measurements of microlensing events. The ability of microlensing to determine the cold planet mass-ratio function in the region where core accretion predicts the most massive planets will form is the reason why microlensing has been selected as a nominal 23% share in the NASA's flagship Nancy Grace Roman Space Telescope (RST) mission. The Roman Space Telescope is designed to provide high cadence, continuous observations of microlensing events in the near-infrared (NIR) and will be sensitive to planets in the outer habitable zone region of FGK stars and objects down the mass of Ganymede. Since it will push the number of microlensing planets from < 100 to into the thousands, advancing our microlensing analysis methodology is critical to the success of the mission and to our knowledge of low-mass planets near and beyond the snow line of the protoplanetary disk. Paving the way for RST is the reason why the Key Strategic Mission Support Program was greenlit on Keck at the outset, and it's this motivator that made this thesis possible. Concurrent with the development of the mass-measurement method is the need for automated analysis tools to derive light-curve solutions and parameter uncertainties in order to maximize the

scientific yield of the telescope.

Much of the driver behind microlensing in the United States is based around RST, which has a planned launch date of 2025. There are a number of planned projects on adjacent projects aimed at wringing the most out of RST. Major ongoing microlensing surveys such as OGLE and MOA, for example, have however been conducted in the visible, where the level of extinction makes it difficult to observed directly towards the Galactic plane. In order to optimize the choice and cadence of microlensing fields for RST, the NASA UKRIT NIR survey has covered all potential RST fields, including those excluded from optical surveys due to extinction, with a cadence of one day. This data could be used to clarify the choice of RST fields by determining the microlensing event rate in the near IR in these fields, map the extinction of these fields, and search for planetary events within these data. Further, any of the planetary events discovered in the existing UKIRT data could be potential candidates for adaptive optics follow-up.

While with Keck we can explore microlensing stars to a detection limits of the order of H$\sim$21, RST will be able to extend this down to H$\sim$23. Despite the space telescope's power to obtain high resolution images of microlensing lens and source stars, it will still not be inherently possible to resolve them immediately upon the start of the RST microlensing survey. To obtain a second epoch a survey with the European Space Agency's Euclid spacecraft of the RST fields down to magnitude $\sim$25 in VIS, Y, J, H as soon as possible after launch in order to constrain source-lens relative proper motion (Bachelet & Penny 2019) and hence provide strong parallax constraints. A Euclid survey would only require 30-40 hours of observing time and would alleviate the need to wait 5+ years following the the launch of RST to achieve the same result. Detailed simulations of these potential Euclid/RST observations will be an important step to making such a proposal a reality.

Finally, the studies in this thesis present options for the future, in particular the white dwarf discussed in Chapter 5. Chapter 5 specifically offers up the possibility of a direct

detection of this object using the Hubble or James Webb space telescopes, which would confirm unequivocally the nature of the system and hence validate the methods used here to place limits on the object. The thousands of planetary microlensing events yielded from RST will likely contain at least some events with dark lenses and the resulting planetary statistics will aid our understanding of post-main sequence planetary evolution and abundance.

A

Keck Reduction Pipeline

In this section I present code that can be used to reduce raw Keck images obtained from the Keck Observatory. Images are available on the Observatory Archive (KOA: https://koa.ipac.caltech.edu/cgi-bin/KOA/nph-KOAlogin). I used this code to reduce the 2015, 2016 and 2018 photometry presented in this thesis. It is primarily designed to be used on raw, unprocessed *.fits files from the NIRC2 imager, but can also be used on images obtained by OSIRIS with little modification. It provides basic dark, flat field and sky corrections on Keck images, together with an algorithm to rename the source files and sort them into a useful directory structure. The code is currently not publicly available as it is not yet been adapted for use by a general user, however it is planned to be made available in

the future. The code archive is located at: https://github.com/blackmanjw/KeckPipeline. The majority of the code in this version was written by Joshua Blackman with some code and input from Katie Vandorou. Jean-Philippe Beaulieu provided advice on the goals and large scale structure of the project. Below is the readme file from the repository, followed by the source code for calib.py and tools.py.

A.1 KECKPipeline Readme

Authors :
Joshua Blackman, joshua.blackman@utas.edu.au
Aikaterini Vandorou, aikaterini.vandorou@utas.edu.au
Jean-Phillipe Beaulieu, beaulieu@iap.fr

This is a pipeline for performing calibration corrections on NIRC2 images obtained on the Keck II telescope.

A.1.1 Installation

Requirements `KECKPipeline` runs on `Python 3`. You will need pip3 or you can choose to manually install the packages. Required Python packages are listed in requirements.txt, and include:

astropy

pandas

They can be installed by running

```
pip install -r requirements.txt
```

This pipeline includes the sewpy Sextractor frontend for python in the folder /utilities/sewpy-master (https://github.com/megalut/sewpy). Install this package with the command: `python setup.py install --user` `KECKPipeline` utilises the `Swarp` and `Sextractor` packages

developed by Emmanuel Bertin. The source for these packages (and installation instructions) can be found on https://www.astromatic.net.

INSTALLATION Download the repository and place it in your desired position on your hard drive. Run `./configure`

```
make
../KeckPipeline/utilities/swarp-2.38.0/./
```

On a Mac you may need to install fftw which is a requirement for Sextractor. To get Sextractor working:

```
wget http://www.netlib.org/lapack/lapack-3.4.2.tgz
./configure --enable-threads
```

A.1.2 DOCUMENTATION

Rename Files

```
python3 calib.py -r --rename
```

How to run

```
python3 calib.py -r -s folder
```

where the -r (–rename) flag moves all raw data obtained from the KOA website (https://koa.ipac.caltech.edu/cgi-bin/KOA/nph-KOAlogin) from a source folder into a more convenient directory structure. The source folder can be specified using the '-s' flag. The resulting structure is shown in Figure A.1.

```
├── Darks
│   ├── 2018-08-05
│       ├── KDark30sec1.fits            # K Dark30sec 1 (Keck, Dark Type, Image Number)
│       └── KDark30sec2.fits
├── Flats
│   ├── 2018-08-05
│       ├── KNarrowLampOffKs1.fits      # K NarrowLampOff Ks 1 (Keck, Flat Type, Filter, Image Number)
│       ├── KNarrowLampOnKs1.fits
│       ├── KNarrowLampOffH1.fits
│       ├── KNarrowLampOffH2.fits
│       ├── KNarrowLampOnH1.fits
│       ├── KNarrowLampOnH2.fits
│       ├── KWideLampOnKs1.fits
│       └── KWideLampOnKs2.fits
├── Objects
│   └── ob151395
│       ├── 2018-08-05
│           ├── KOB151395Ks1.fits       # K ob151395 Ks 1 (Keck, Object Name, Filter, Image Number)
│           ├── KOB151395Ks2.fits       # where Object Name is the microlensing convention:
│           └── KOB151395Ks3.fits       # ob 15 1395 (telescope, year, event)
│       └── 2018-08-06
│           ├── KOB151395NKs1.fits      # As above except the "N" denotes this is an image taken
│           ├── KOB151395NKs2.fits      # with the NARROW camera. Images without this signifier are taken
│           └── KOB151395NKs3.fits      # with the WIDE camera.
│   └── mb10353
│       └── 2018-08-07
│           ├── KMB10353H1.fits
│           └── KMB10353H2.fits
├── Skys
│   ├── 2018-08-05
│       ├── KskyNarrowKs1.fits           # K skyNarrow Ks 1 (Keck, Sky Type, Filter, Image Number)
│       └── KskyNarrowKs2.fits
├── Source                               # Backup of Original KOA Download
├── calib.py
└── tools.py
```

Figure A.1: Keck Pipeline Raw Data Folder Structure

```
├── Darks
│   ├── 2018-08-05
│       ├── KDark30sec1.fits
│       ├── ...
│       └── KDark30sec10.fits
│   └── KDark30sec0805.fits             # Combined Dark frame with Date.
├── Flats
│   ├── 2018-08-05
│       ├── KNarrowLampOffKs1.fits
│       ├── ...
│       └── KWideLampOnKs2.fits
│   ├── KFlatKs0805.fits                # Combined Flats with Date. Images are for the wide camera unless
│   ├── KFlatH0805.fits                 # signified with an 'N'
│   └── KFlatNKs0805.fits
├── Objects
│   └── ob151395
│       ├── 2018-08-05
│           ├── Source
│               ├── KOB151395Ks1.fits
│               ├── ...
│               ├── KOB151395Ks10.fits
│               ├── cor_KOB151395Ks1.fits          # STEP 1: Individual Frames Corrected for Distortion
│               ├── ...
│               ├── cor_KOB151395Ks10.fits
│               ├── ast_cor_KOB151395Ks1.fits      # STEP 2: Astrometry Corrected Frames
│               ├── ...
│               └── ast_cor_KOB151395Ks10.fits
│           ├── coadd_ac_KOB151395Ks.fits         # STEP 3: Coadded master frame with SWARP
│           └── sex_cac_KOB151395Ks.tst            # STEP 4: Photometry TST File Obtained with SEXTRACTOR
├── Skys
│   ├── 2018-08-05
│       ├── KskyNarrowKs1.fits
│       ├── ...
│       └── KskyNarrowKs10.fits
│   ├── KSkyKs0805.fits                 # Combined SkyFlats with Date. Images are for the wide camera unless
│   ├── KSkyH0805.fits                  # signified with an 'N'
│   └── KSkyNKs0805.fits
├── Source
├── calib.py
└── tools.py
```

Figure A.2: Keck Pipeline Processed Data Folder Structure

A.2 Source Code

A.2.1 calib.py

```
from utilities.utilities import import_user_config
import tools

## This is the main executable to run the functions in tools.py
## Run the program as "python calib.py" with the appropriate flags below depending on what you want to
↪  do.
## Eg. To move files, use the -m flag.

if __name__ == "__main__":
    # Allow user to in CLI optionally overwrite the config values
    import argparse
    import textwrap

    parser = argparse.ArgumentParser(formatter_class=argparse.RawTextHelpFormatter,
                                     description=textwrap.dedent('''\
            '''))

    parser.add_argument('-c', '--config', type=str, nargs=1, help='usage -c /path/to/config.json')
    parser.add_argument('-l', '--list', type=str, nargs=1, help='usage -l file.list')
    parser.add_argument('-r', '--rename', action="store_true")
    parser.add_argument('-s', '--source', type=str, nargs=2, help='usage -c /path/to/config.json')
    parser.add_argument('-fs', '--flatsubtract', action="store_true")
    parser.add_argument('-dl', '--darklist', action="store_true")
    parser.add_argument('-fl', '--flatlist', action="store_true")
    parser.add_argument('-ds', '--darksubtract', action="store_true")
    parser.add_argument('-dc', '--darkcombine', action="store_true")
    parser.add_argument('-fc', '--flatcombine', action="store_true")
    parser.add_argument('-sky', '--skycombine', action="store_true")
```

```
28  parser.add_argument('-t', '--test', action="store_true")
29
30  args = parser.parse_args()
31  #print(args)
32  if args.config is None:
33      config = import_user_config('config/my_config.json')
34  else:
35      config = import_user_config(args.config[0])
36  if args.darkcombine:
37      config.update({'dark_combine': True})
38  if args.darksubtract:
39      config.update({'dark_subtract': True})
40  if args.darklist:
41      tools.darklist('Darks')
42  if args.source is None:
43      dir='Data'
44  else:
45      source_dir=args.source[0]
46      dest_dir = args.source[1]
47  if args.rename:
48      tools.rename(source_dir,dest_dir)
49  if args.flatlist:
50      tools.flatlist('Flats')
51  if args.darkcombine:
52      tools.darklist('Darks')
53      tools.darkcombine()
54  if args.flatcombine:
55      config.update({'flat_combine': True})
56      print('Please combine flats!!!')
57  if args.flatsubtract:
58      config.update({'flat_subtract': True})
59  if args.flatsubtract:
```

```
60        config.update({'move_data': True})
61        tools.movedata('2018-05-05',3)
62    if args.list:
63        config.update({'list': args.list[0]})
64    if args.test:
65        print('We Win!!!!!')
```

A.2.2 TOOLS.PY

```
1  ##########################################################################
2  #                KECK NIRC2 AO Reduction Tools                           #
3  #                                                                        #
4  #                  REVISION: 0.0.1                                       #
5  #                                                                        #
6  #                  Joshua Blackman                                       #
7  #                 Aikaterini Vandorou                                    #
8  #                 Univeristy of Tasmania                                 #
9  #                                                                        #
10 #                 Last Change: Oct 2018                                  #
11 ##########################################################################
12 #
13 #
14 # This is a pipeline to reduce AO images from the NIRC2 imager on KECK II.
15 #
16 #
17
18 import pandas as pd
19 import numpy as np
20 import shutil
21 from datetime import datetime, timedelta
22 from glob import glob
```

```
23 from ccdproc import ImageFileCollection
24 import warnings
25 from astropy.io import fits
26 import astropy.units as u
27 from astropy.nddata import CCDData
28 from astropy.io import fits
29 import ccdproc
30 from itertools import product
31 import os
32 from astropy.io.fits import getdata
33 import astromatic_wrapper as aw
34 import numpy as np
35 from distutils import dir_util
36 from photutils import make_source_mask
37 from astropy.stats import sigma_clipped_stats
38
39 warnings.filterwarnings("ignore")
40
41
42 # ------------------------------ USEFUL FUNCTIONS -----------------------------
43
44 def keep_going(text="Do you wish to continue? Answer Y or N."):
45     """
46         This function asks the user whether or not they want the script to proceed.
47         The user needs to type 'Y' (no quotes), else the script will abort.
48         Parameters
49         ----------
50         text: str
51         Modify text to present to the user. Default is 'Do you wish to continue? Answer Y or N."
52         """
53     answer = input(text)
54
```

```
55    if answer == 'Y':
56        print("The script is now running....")
57    else:
58        print("You have chosen to quit this program")
59        raise SystemExit
60
61
62  def swarp(files, output='output.fits', celestial_type='EQUATORIAL'):
63      """
64        Run SWARP!
65        Parameters
66        ----------
67       files: list
68          A list of files to swarp.
69        output: str
70          Path and filename for the combined output *.fits file.
71        celestial_type: str
72          Define celetial type as in the swarp config/config.swarp file.
73          Options are NAITVE, PIXEL, EQUATORIAL, GALACTIC, ECLIPTIC or
    ↪  SUPERGALACTIC.
74      """
75      kwargs = {
76        'code': 'SWarp',
77        'config': {
78            'SUBTRACT_BACK': 'N',
79            'IMAGEOUT_NAME': output,
80            'RESCALE_WEIGHTS': 'N',
81            'RESAMPLE': 'N',
82            'COMBINE_TYPE': 'MEDIAN',
83            'PIXEL_SCALE': '0',
84            'CELESTIAL_TYPE': celestial_type,
85            'INTERPOLATE': 'N',
```

```
86          'BLANK_BADPIXELS': 'N',
87          'COPY_KEYWORDS':
            ↪  'OBJECT,CAMNAME,FWINAME,ITIME,DATE-OBS,OBSDATE,FLSPECTR,HISTORY'
88        },
89        'temp_path': '.',
90        'config_file': 'config/config.swarp'
91    }
92
93    swarp = aw.api.Astromatic(**kwargs)
94    swarp.run(files)
95
96
97  def sex(files, output='output.cat', phot_aperture=10, back_size=256):
98      """
99        Run SExtractor!
100       Parameters
101       ----------
102       files: list
103           A list of files to SExtractor.
104       output: str
105           Path and filename for the catalog output  *.cat file.
106       phot_aperture:
107           Magnitude aperture diameter in pixels.
108       back_size:
109           Background mesh size in pixels.
110     """
111     kwargs = {
112       'code': 'SExtractor',
113       'config': {
114         'CATALOG_NAME': output,
115         'FILTER': 'N',
116         'CLEAN': 'Y',
```

```
117         'MASK_TYPE': 'CORRECT',
118         'PHOT_APERTURES': str(phot_aperture),
119         'DETECT_MINAREA': str(7),
120         'DETECT_THRESH': str(7),
121         'ANALYSIS_THRESH': str(7),
122         'BACK_SIZE': str(back_size),
123     },
124     # Output parameters
125     'params': ['NUMBER', 'BACKGROUND', 'XWIN_IMAGE', 'YWIN_IMAGE',
        ↪  'MAG_AUTO', 'FLUX_APER', 'FLUXERR_APER'],
126     'temp_path': '.',
127     'config_file': 'config/config.sex'
128 }
129
130 sex = aw.api.Astromatic(**kwargs)
131 sex.run(files)
132
133
134 from photutils import make_source_mask
135 from astropy.stats import sigma_clipped_stats
136
137 def backgroundestimate(file, size=10):
138     """
139     This function estimates the background of a fits images via iteration and masking of any sources.
140
141     Required imports: from photutils import make_source_mask
142                       from astropy.stats import sigma_clipped_stats
143     Parameters
144     ----------
145     file:
146         Path to fits file.
147     output:
```

```
148         The mean background count.
149     """
150     data=CCDData.read(file ,unit="adu")
151     mask=make_source_mask(data, snr=2, npixels=5, dilate_size=size)
152     mean, median, std = sigma_clipped_stats(data, sigma=3.0, mask=mask)
153     #print(mean)
154     return mean
155 
156 # ------------------------------ PIPELINE FUNCTIONS ------------------------------
157 
158 def rename(source_dir,dest_dir):
159     """
160         This function takes the downloaded files from the KOA website, renames them and sorts into folders
    ↪ named Objects, Darks, Flats and Skys.
161         Objects are sorted by object name (read from the fits header), then date. Calibration files are sorted by
    ↪ date.
162         This function will DELETE the original folder but backup the folder into a directory called Source.
163         Before proceeding the function will ask the user if they wish to proceed.
164         As with the other functions in tools.py, this function is run via calib.py.
165         This function can be run with "python3 calib.py -r -s <source_dir> <dest_dir>" where <soure_folder> is
    ↪ the path to your data you wish to move and rename.
166         Parameters
167         ----------
168         source_dir: str
169             Define the folder where the source files are located.
170         dest_dir: str
171             Define the output folder. The Object, Darks etc. folders will be created under this parent.
172         Returns
173         -------
174         data_headers
175             Table with columns showing input files, output files, object name and exposure time.
176     """
```

```
177 keep_going(text="This script will backup the original folder to dest_dir/Source/** and remove the
    ↪ original folder. It will make copies of the  original files and rename them in directories called
    ↪ Darks, Flats, etc. Do you wish to continue? Answer Y or N.")
178
179 ## Backup Original Source Folder
180 dir_util.copy_tree(source_dir, dest_dir + '/Source')
181
182 data = []
183 for file in os.listdir("./" + source_dir):  # put in your path directory
184     if file.endswith(".fits"):  # what does the file end with?
185         data.append(os.path.join(source_dir, file))
186
187 n = len(data)
188 obj, itime, filt, renamed, datemod, count, flatmod, mod = ([] for i in range(8))
189 for i in range(0, n):
190     header = fits.getheader(data[i])
191     Name, Date, Number, Ext = data[i].split(".")
192     obj.append(header['OBJECT'])
193     itime.append(header['ITIME'])
194     filt.append(header['FWINAME'])
195     mod.append((header['OBJECT'] + header['FWINAME']))
196     flatmod.append((header['OBJECT'] + header['FWINAME'] + Date))
197     datemod.append(datetime.strptime(Date, "%Y%m%d").date())
198     if flatmod[i] in flatmod:
199         count = flatmod.count(flatmod[i])
200     if ('Lamp' in obj[i] or 'Flat' in obj[i]):
201         renamed.append((dest_dir + '/Flats/' + str(datemod[i]) + '/' + 'K' + header['OBJECT'] +
        ↪ str(count) + ".fits"))
202         os.makedirs(os.path.dirname(dest_dir + '/Flats/' + str(datemod[i]) + '/'), exist_ok=True)
203     elif ('Dark' in obj[i]) or ('dark' in obj[i]):
204         renamed.append((dest_dir + '/Darks/' + str(datemod[i]) + '/' + 'K' + header['OBJECT'] +
        ↪ str(count) + ".fits"))
```

```
205             os.makedirs(os.path.dirname(dest_dir + '/Darks/' + str(datemod[i]) + '/'), exist_ok=True)
206         elif ('Sky' in obj[i]) or ('sky' in obj[i]):
207             renamed.append((dest_dir + '/Skys/' + str(datemod[i]) + '/' + 'K' + header['OBJECT'] +
                ↪  header['FWINAME'] + str(
208                 count) + ".fits"))
209             os.makedirs(os.path.dirname(dest_dir + '/Skys/' + str(datemod[i]) + '/'), exist_ok=True)
210         else:
211             renamed.append((dest_dir + '/Objects/' + header['OBJECT'].upper() + '/' + str(datemod[i])
                ↪  + '/' + 'K' + list(header['CAMNAME'])[0].title() + header['OBJECT'].upper() +
212                             header['FWINAME'] + str(
213                         count) + ".fits"))
214             os.makedirs(os.path.dirname(dest_dir + '/Objects/' + header['OBJECT'].upper() + '/' +
                ↪  str(datemod[i]) + '/'), exist_ok=True)
215         os.rename(data[i], renamed[i])
216
217     ## REMOVE LEFT OVER original Folders
218     shutil.rmtree(source_dir)
219
220     lists = [data, mod, datemod, itime, flatmod, renamed]
221     data_headers = pd.concat([pd.Series(x) for x in lists], axis=1)
222
223     return data_headers
224
225
226 # ----------------------------
227
228 def darkcombine(darks_dir='Darks/'):
229     """
230         This function combines Dark frames for each date and exposure time as per the filestructure created by
    ↪  "Rename".
231         Parameters
232         ----------
```

```
233     darks_dir: str
234         Define the folder where the dark files are located.
235     Returns
236     -------
237     ????
238 """
239 
240 # Make list of all Dark Directories
241 darkdir = glob(darks_dir + '*/')
242 print(darkdir)
243 
244 ## For each subdirectory in darkdir, combine the Dark Files (ATM only 30sec)
245 for d in darkdir:
246     keys = ['OBJECT', 'CAMNAME', 'FWINAME', 'ITIME', 'DATE-OBS']
247     images = ImageFileCollection(d, keywords=keys)
248 
249     matches5 = (images.summary['ITIME'] < 6)
250     dark5 = [d + x for x in images.summary['file'][matches5].tolist()]
251     if dark5:
252         swarp(dark5, output=darks_dir + 'Dark5sec' + d.split("-")[1] + d.split("-")[2][:-1] + '.fits',
        ↪ celestial_type='PIXEL')
253 
254     matches10 = (images.summary['ITIME'] == 10)
255     dark10 = [d + x for x in images.summary['file'][matches10].tolist()]
256     if dark10:
257         swarp(dark10, output=darks_dir + 'Dark10sec' + d.split("-")[1] + d.split("-")[2][:-1] + '.fits',
        ↪ celestial_type='PIXEL')
258 
259     matches15 = (images.summary['ITIME'] == 15)
260     dark15 = [d + x for x in images.summary['file'][matches15].tolist()]
261     if dark15:
```

```
262         swarp(dark15, output=darks_dir + 'Dark15sec' + d.split("-")[1] + d.split("-")[2][:-1] + '.fits',
            ↪ celestial_type='PIXEL')
263
264     matches30 = (images.summary['ITIME'] == 30)
265     dark30 = [d + x for x in images.summary['file'][matches30].tolist()]
266     if dark30:
267         swarp(dark30, output=darks_dir + 'Dark30sec' + d.split("-")[1] + d.split("-")[2][:-1] + '.fits',
            ↪ celestial_type='PIXEL')
268
269     matches60 = (images.summary['ITIME'] == 60)
270     dark60 = [d + x for x in images.summary['file'][matches60].tolist()]
271     if dark60:
272         swarp(dark60, output=darks_dir + 'Dark60sec' + d.split("-")[1] + d.split("-")[2][:-1] + '.fits',
            ↪ celestial_type='PIXEL')
273
274
275 # ----------------------------
276
277 def darksubtract(dir='Flats', master_dark='Darks/Dark60sec0807.fits'):
278     """
279         This function subtracts the darks from files in a give directory.
280         Parameters
281         ----------
282         ????
283         Returns
284         -------
285         ????
286     """
287     # master_dark = input("Which Master Dark in the /Darks/ folder (or otherwise) would you like to use?")
288
289     # if answer == 'Y':
290     #   print("The script is now running....")
```

```
291 # else:
292 #   print("You have chosen to quit this program")
293 #   raise SystemExit
294
295 if dir == "Flats":
296     dir = 'Flats/*/'
297 elif dir == "Skys":
298     dir = 'Skys/*/'
299 elif dir =="Objects":
300     dir = 'Objects/*/*/'
301
302 mdark = CCDData.read(master_dark, unit="adu")
303
304 for d in glob(dir):
305     keys = ['OBJECT', 'CAMNAME', 'FWINAME', 'ITIME', 'DATE-OBS', 'FLSPECTR',
    ↪  'HISTORY']
306     images = ImageFileCollection(d, keywords=keys, glob_exclude='d*', glob_include='*.fits')
307
308     directory = d + '/dark_subtracted'
309     if not os.path.exists(directory):
310         os.makedirs(directory)
311
312     # Read in all files from /FLATS/ subdirectories and subtract the master_dark. The output is stored in
    ↪  'dflat'.
313     for flat, fname in images.hdus(return_fname=True):
314         meta = flat.header
315         meta['FILENAME'] = fname
316         flat_exposure = flat.header['ITIME']
317         flats = CCDData(data=flat.data.astype('float32'), meta=meta, unit="adu")
318         dflat = (ccdproc.subtract_dark(flats, mdark, exposure_time='ITIME',
319                                        exposure_unit=u.second,
```

```
320                             add_keyword={'HISTORY': 'Dark Subtracted', 'OBSDATE':
                                ↪  flat.header['DATE-OBS'],
321                             'CRVAL1': meta['CRVAL1'], 'CRVAL2': meta['CRVAL2']},
322                             scale=True))
323         #print(dflat.meta['CRVAL1'])
324         dflat.wcs = None
325         dflat.write(directory + '/d' + fname, overwrite=True)
326         fits.writeto
327
328 # ----------------------------
329
330 def flatcombine(dir='Flats/*/dark_subtracted/'):
331     """
332         This function subtracts the darks from files in a give directory.
333         Parameters
334         ----------
335         ????
336         Returns
337         -------
338         ????
339     """
340
341     for d in glob(dir):
342
343         directory = "/".join(d.split('/')[0:2]) + '/swarped'
344         if not os.path.exists(directory):
345             os.makedirs(directory)
346
347         keys = ['OBJECT', 'CAMNAME', 'FWINAME', 'ITIME', 'OBSDATE', 'FLSPECTR',
         ↪  'HISTORY']
348         images = ImageFileCollection(d, keywords=keys, glob_include='d*.fits')
349
```

```
350     swarpfilter(d, dir, directory, images, keys, filter='H', lamp='on', camera='narrow',
351             done='Dark Subtracted', output='cKNarrowLampOnH', type='PIXEL')
352     swarpfilter(d, dir, directory, images, keys, filter='H', lamp='off', camera='narrow',
353             done='Dark Subtracted', output='cKNarrowLampOffH', type='PIXEL')
354     swarpfilter(d, dir, directory, images, keys, filter='H', lamp='on', camera='wide', done='Dark
        ↪ Subtracted',
355             output='cKWideLampOnH', type='PIXEL')
356     swarpfilter(d, dir, directory, images, keys, filter='H', lamp='off', camera='wide', done='Dark
        ↪ Subtracted',
357             output='cKWideLampOffH', type='PIXEL')
358     swarpfilter(d, dir, directory, images, keys, filter='Ks', lamp='on', camera='narrow', done='Dark
        ↪ Subtracted',
359             output='cKNarrowLampOnKs', type='PIXEL')
360     swarpfilter(d, dir, directory, images, keys, filter='Ks', lamp='off', camera='narrow', done='Dark
        ↪ Subtracted',
361             output='cKNarrowLampOffKs', type='PIXEL')
362     swarpfilter(d, dir, directory, images, keys, filter='Ks', lamp='on', camera='wide', done='Dark
        ↪ Subtracted',
363             output='cKWideLampOnKs', type='PIXEL')
364     swarpfilter(d, dir, directory, images, keys, filter='Ks', lamp='off', camera='wide', done='Dark
        ↪ Subtracted',
365             output='cKWideLampOffKs', type='PIXEL')
366     swarpfilter(d, dir, directory, images, keys, filter='J', lamp='on', camera='narrow', done='Dark
        ↪ Subtracted',
367             output='cNarrowLampOnJ', type='PIXEL')
368     swarpfilter(d, dir, directory, images, keys, filter='J', lamp='off', camera='narrow', done='Dark
        ↪ Subtracted',
369             output='cKNarrowLampOffJ', type='PIXEL')
370     swarpfilter(d, dir, directory, images, keys, filter='J', lamp='on', camera='wide', done='Dark
        ↪ Subtracted',
371             output='cKWideLampOnJ', type='PIXEL')
```

```
372     swarpfilter(d, dir, directory, images, keys, filter='J', lamp='off', camera='wide', done='Dark
        ↪ Subtracted',
373             output='cKWideLampOffJ', type='PIXEL')
374
375
376 # ----------------------------
377
378 def flatprocess(dir='Flats/*/swarped/'):
379     """
380     Parameters
381     ----------
382     ????
383     Returns
384     -------
385     ????
386     """
387     print(glob(dir))
388     for d in glob(dir):
389
390         keys = ['OBJECT', 'CAMNAME', 'FWINAME', 'ITIME', 'OBSDATE', 'FLSPECTR',
        ↪ 'HISTORY']
391         images = ImageFileCollection(d, keywords=keys, glob_include='c*.fits')
392         cameras = ['wide', 'narrow']
393         filters = ['Ks', 'H', 'J']
394         flats = []
395
396         for camera, filter in product(cameras, filters):
397
398             for hdu, fname in images.hdus(CAMNAME=camera, FWINAME=filter,
        ↪ return_fname=True):
399                 meta = hdu.header
400                 meta['filename'] = fname
```

```
401             flats.append(ccdproc.CCDData(data=hdu.data.astype('float32'), meta=meta, unit="adu"))
402         if flats:
403             MasterFlat = ccdproc.subtract_dark(flats[1], flats[0], exposure_time='ITIME',
404                                                exposure_unit=u.second,
405                                                add_keyword={'HISTORY2': 'Lamp Off Subtracted'},
406                                                scale=False)
407
408             # Normalize Flat
409             MasterFlat.data = MasterFlat / np.ma.average(MasterFlat)
410             MasterFlat.wcs = None
411             MasterFlat.write(
412                 'Flats/KFlat' + MasterFlat.meta['CAMNAME'].title() +
                    ↪ MasterFlat.meta['FWINAME'].title() +
413                 MasterFlat.meta['OBSDATE'].split("-")[1] +
                    ↪ MasterFlat.meta['OBSDATE'].split("-")[2] + '.fits',
414                 overwrite=True)
415             flats[:] = []
416
417
418 # ----------------------------
419
420 def flatcorrect(dir='Skys', flatdate='2018-08-07'):
421     """
422         Parameters
423         ----------
424         ????
425         Returns
426         -------
427         ????
428     """
429
430     if dir == "Skys":
```

```
431     dir = 'Skys/*/dark_subtracted/'
432 elif dir =="Objects":
433     dir = 'Objects/*/*/dark_subtracted/'
434 
435 keys = ['OBJECT', 'CAMNAME', 'FWINAME', 'ITIME', 'OBSDATE', 'FLSPECTR',
    ↪  'HISTORY']
436 flatfiles = ImageFileCollection('Flats', keywords=keys)
437 cameras = ['wide', 'narrow']
438 filters = ['Ks', 'H', 'J']
439 add_filters = {'OBSDATE': flatdate}
440 flats = {}
441 
442 ## IMPORT MASTER FLATS for chosen date in dictionary flats={}
443 
444 for camera, filter in product(cameras, filters):
445 
446     for hdu, fname in flatfiles.hdus(CAMNAME=camera, FWINAME=filter, return_fname=True,
    ↪  **add_filters):
447         meta = hdu.header
448         meta['filename'] = fname
449         flats[fname[:-5]] = ccdproc.CCDData(data=hdu.data.astype('float32'), meta=meta,
        ↪  unit="adu")
450 
451 ## APPLY FLAT CORRECTION TO IMAGES
452 
453 for d in glob(dir):
454 
455     if dir == "Skys/*/dark_subtracted/":
456         directory = "/".join(d.split('/')[0:2]) + '/flat_corrected'
457     elif dir =="Objects/*/*/dark_subtracted/":
458         directory = "/".join(d.split('/')[0:3]) + '/flat_corrected'
459 
```

```
460     if not os.path.exists(directory):
461         os.makedirs(directory)
462 
463     images = ImageFileCollection(d, keywords=keys, glob_include='d*.fits')
464     skys = []
465 
466     for camera, filter in product(cameras, filters):
467 
468         for hdu, fname in images.hdus(CAMNAME=camera, FWINAME=filter,
        ↪  return_fname=True):
469             meta = hdu.header
470             meta['filename'] = fname
471             sky = ccdproc.CCDData(data=hdu.data.astype('float32'), meta=meta, unit="adu")
472 
473             if (meta['CAMNAME'] == 'wide') and (meta['FWINAME'] == 'Ks'):
474                 cflat = ccdproc.flat_correct(sky,
475                                              flats['KFlatWideKs' + flatdate.split('-')[1] + flatdate.split('-')[2]])
476                 cflat.wcs = None
477                 cflat.write(directory + '/f' + fname, overwrite=True)
478             elif (meta['CAMNAME'] == 'narrow') and (meta['FWINAME'] == 'Ks'):
479                 cflat = ccdproc.flat_correct(sky, flats[
480                     'KFlatNarrowKs' + flatdate.split('-')[1] + flatdate.split('-')[2]])
481                 cflat.wcs = None
482                 cflat.write(directory + '/f' + fname, overwrite=True)
483             elif (meta['CAMNAME'] == 'wide') and (meta['FWINAME'] == 'H'):
484                 cflat = ccdproc.flat_correct(sky,
485                                              flats['KFlatWideH' + flatdate.split('-')[1] + flatdate.split('-')[2]])
486                 cflat.wcs = None
487                 cflat.write(directory + '/f' + fname, overwrite=True)
488             elif (meta['CAMNAME'] == 'narrow') and (meta['FWINAME'] == 'H'):
489                 cflat = ccdproc.flat_correct(sky, flats[
490                     'KFlatNarrowH' + flatdate.split('-')[1] + flatdate.split('-')[2]])
```

```
491                 cflat.wcs = None
492                 cflat.write(directory + '/f' + fname, overwrite=True)
493             elif (meta['CAMNAME'] == 'wide') and (meta['FWINAME'] == 'J'):
494                 cflat = ccdproc.flat_correct(sky,
495                                              flats['KFlatWideJ' + flatdate.split('-')[1] + flatdate.split('-')[2]])
496                 cflat.wcs = None
497                 cflat.write(directory + '/f' + fname, overwrite=True)
498             elif (meta['CAMNAME'] == 'narrow') and (meta['FWINAME'] == 'J'):
499                 cflat = ccdproc.flat_correct(sky, flats[
500                     'KFlatNarrowJ' + flatdate.split('-')[1] + flatdate.split('-')[2]])
501                 cflat.wcs = None
502                 cflat.write(directory + '/f' + fname, overwrite=True)
503
504
505 # ----------------------------
506
507 def skycombine(dir = 'Objects'):
508     """
509         This function combines the skys from files in a give directory, after they have been dark
510         subtracted and flat corrected.
511         Parameters
512         ----------
513         ????
514         Returns
515         -------
516         ????
517     """
518
519     if dir =="Objects":
520         dir = 'Objects/*/*/flat_corrected/'
521
522     for d in glob(dir):
```

```
523
524     directory = "/".join(d.split('/')[0:2]) + '/swarped'
525     if not os.path.exists(directory):
526         os.makedirs(directory)
527
528     keys = ['OBJECTS', 'ITIME', 'FWINAME', 'OBSDATE', 'CAMNAME', 'HISTORY',
        ↪  'FLSPECTR']
529     images = ImageFileCollection(d, keywords = keys, glob_include = 'f*.fits')
530
531     swarpfilter(d, dir, directory, images, keys, filter='H', lamp = '*', camera = 'narrow',
532             done='Dark Subtracted', output='cKSkyNarrowH', type='EQUATORIAL')
533     swarpfilter(d, dir, directory, images, keys, filter='H',lamp = '*', camera = 'wide',
534             done='Dark Subtracted', output='cKSkyWideH', type='EQUATORIAL')
535     swarpfilter(d, dir, directory, images, keys, filter='J',lamp = '*', camera = 'narrow',
536             done='Dark Subtracted', output='cKSkyNarrowJ', type='EQUATORIAL')
537     swarpfilter(d, dir, directory, images, keys, filter='J', lamp = '*',camera = 'wide',
538             done='Dark Subtracted', output='cKSkyWideJ', type='EQUATORIAL')
539     swarpfilter(d, dir, directory, images, keys, filter='Ks',lamp = '*', camera = 'narrow',
540             done='Dark Subtracted', output='cKSkyNarrowKs', type='EQUATORIAL')
541     swarpfilter(d, dir, directory, images, keys, filter='Ks',lamp = '*', camera = 'wide',
542             done='Dark Subtracted', output='cKSkyWideKs', type='EQUATORIAL')
543     swarpfilter(d, dir, directory, images, keys, filter='Lp',lamp = '*', camera = 'narrow',
544             done='Dark Subtracted', output='cKSkyNarrowLp', type='EQUATORIAL')
545     swarpfilter(d, dir, directory, images, keys, filter='Lp',lamp = '*', camera = 'wide',
546             done='Dark Subtracted', output='cKSkyNarrowLp', type='EQUATORIAL')
547
548
549 # -------------------------
550
551 def skycorrect(dir='Objects'):
552     """
553         This function applys the sky correction to the object files. This takes the form:
```

```
554
555     OBJECT - SKY (mean object background / mean sky background)
556
557     Parameters
558     ----------
559     dir: str
560         Target directory containing subdirectories for each object.
561     Returns
562     -------
563     ????
564 """
565
566 if dir =="Objects":
567     dir = 'Objects/OB05390/*/flat_corrected/'
568
569 keys = ['OBJECT', 'CAMNAME', 'FWINAME', 'ITIME', 'OBSDATE', 'FLSPECTR',
    ↪  'HISTORY']
570 cameras = ['wide', 'narrow']
571 filters = ['Ks']
572 skys = {}
573 objects = {}
574
575 ## Import MASTER SKYS from swarped directory for all date folders under Skys/*
576
577 for d in glob('Skys/*/swarped'):
578
579     files = ImageFileCollection(d, keywords=keys, glob_include='*.fits')
580
581     for camera, filter in product(cameras, filters):
582
583         for hdu, fname in files.hdus(CAMNAME=camera, FWINAME=filter,
        ↪  return_fname=True):
```

```
584             meta = hdu.header
585             meta['filename'] = fname
586             skys[fname[:-5]+ meta['OBSDATE'].split("-")[1] + meta['OBSDATE'].split("-")[2]] = (
587                 [ccdproc.CCDData(data=hdu.data.astype('float32'), meta=meta, unit="adu"),
588                  backgroundestimate(d + '/' + fname)])
589
590     ## APPLY SKY CORRECTION to Images
591     for d in glob(dir):
592
593         directory = "/".join(d.split('/')[0:3]) + '/sky_corrected'
594         if not os.path.exists(directory):
595             os.makedirs(directory)
596
597         images = ImageFileCollection(d, keywords=keys, glob_include='*.fits')
598
599         for camera, filter in product(cameras, filters):
600
601             for hdu, fname in images.hdus(CAMNAME=camera, FWINAME=filter,
    ↪    return_fname=True):
602                 meta = hdu.header
603                 meta['filename'] = fname
604                 objects[fname[:-5]+ meta['OBSDATE'].split("-")[1] + meta['OBSDATE'].split("-")[2]] =
    ↪    (
605                     [ccdproc.CCDData(data=hdu.data.astype('float32'), meta=meta, unit="adu"),
606                      backgroundestimate(d + '/' + fname)])
607
608                 science = objects[fname[:-5]+ meta['OBSDATE'].split("-")[1] +
609                                                 meta['OBSDATE'].split("-")[2]][0]
610                 sciback = objects[fname[:-5]+ meta['OBSDATE'].split("-")[1] +
611                                                meta['OBSDATE'].split("-")[2]][1]
612
613                 if (meta['CAMNAME'] == 'wide') and (meta['FWINAME'] == 'Ks'):
```

```
614
615             skymod = skys['cKSkyWideKs' + meta['OBSDATE'].split("-")[1] +
616                                     meta['OBSDATE'].split("-")[2]][0]
617             skyback = skys['cKSkyWideKs' + meta['OBSDATE'].split("-")[1] +
618                                     meta['OBSDATE'].split("-")[2]][1]
619
620             skymodm = ccdproc.gain_correct(skymod, sciback/skyback)
621
622             ## Correct Science Image buy subtracting scaled sky
623             sobject=ccdproc.subtract_dark(science, skymodm, exposure_time='ITIME',
624                                     exposure_unit=u.second,
625                                     add_keyword={'HISTORY_3': 'Sky Subtracted'}, scale=False)
626
627             ###Add 100ADU to each pixel to prevent negative values after sky subtraction
628             mod100 = CCDData(np.full((1024, 1024), 200.0, dtype='float32'), unit=u.adu)
629             sobject.data = np.add(sobject,mod100)
630             ###Write sky_corrected files
631             sobject.wcs = None
632             sobject.write(directory + '/s' + fname, overwrite=True)
633
634
635 # ---------------------------- REQUIRED FUNCTIONS ----------------------------
636
637 def swarpfilter(d, dir, directory, images, keys, filter, lamp, camera, done, output, type):
638     """
639         This function runs a swarp on a subset of images from an ImageFileCollection according to the chosen
    ↪  parameters
640         (Filter, Band, Camera etc.) This function is only used in other functions like flatcombine.
641     """
642     filt = images.files_filtered(FWINAME=filter, FLSPECTR=lamp, CAMNAME=camera,
    ↪  HISTORY=done)
643     files = [d + x for x in filt.tolist()]
```

```
644     print(files)
645     if files:
646         swarp(files, output=directory + '/' + output + '.fits', celestial_type=type)
```

References

Adams, A. D., Boyajian, T. S., & von Braun, K. 2018, MNRAS, 473, 3608

Albrow, M. D., Beaulieu, J.-P., Caldwell, J. A. R., et al. 1999, ApJ, 522, 1011

Alcock, C., Allsman, R. A., Alves, D., et al. 1995, ApJ, 454, 125

Alcock, C., Allsman, R. A., Alves, D., et al. 1996, ApJ, 463, L67

Alcock, C., Allsman, R. A., Alves, D., et al. 1997, ApJ, 486, 697

Alcock, C., Allsman, R. A., Alves, D. R., et al. 2000, ApJ, 542, 281

An, J. H., Albrow, M. D., Beaulieu, J., et al. 2002, ApJ, 572, 521

Andrae, R., Schulze-Hartung, T., & Melchior, P. 2010, arXiv:1012.3754

Bachelet, E., Norbury, M., Bozza, V., & Street, R. 2017, ApJ, 154, 203

Bachelet, E., & Penny, M. 2019, ApJ, 880, L32

Bachelet, E., Shin, I.-G., Han, C., et al. 2012, ApJ, 754, 73

Batista, V., Beaulieu, J.-P., Bennett, D. P., et al. 2015, ApJ, 808, 170

Batista, V., Gould, A., Dieters, S., et al. 2011, A&A, 529, 102

Batista, V., Beaulieu, J.-P., Gould, A., et al. 2013, ApJ, 780

Batista, V., Beaulieu, J. P., Gould, A., et al. 2014, ApJ, 780, 54

Beaulieu, J.-P. 2018, Universe, 4, 61

Beaulieu, J.-P., Bennett, D. P., Fouqué, P., et al. 2006, Nature, 439, 437

Beaulieu, J.-P., Bennett, D. P., Batista, V., et al. 2016, ApJ, 824, 83

Beaulieu, J.-P., Batista, V., Bennett, D. P., et al. 2018, ApJ, 155, 78

Bennett, D. P., Anderson, J., Bond, I. A., Udalski, A., & Gould, A. 2006, ApJ, 647, L171

Bennett, D. P., & Rhie, S. H. 1996, ApJ, 472, 660

Bennett, D. P., Bond, I. A., Udalski, A., et al. 2008, ApJ, 684, 663

Bennett, D. P., Rhie, S. H., Nikolaev, S., et al. 2010, ApJ, 713, 837

Bennett, D. P., Batista, V., Bond, I. A., et al. 2014, ApJ, 785, 155

Bennett, D. P., Bhattacharya, A., Anderson, J., et al. 2015, ApJ, 808, 169

Bennett, D. P., Rhie, S. H., Udalski, A., et al. 2016, ApJ, 152, 125

Bennett, D. P., Udalski, A., Bond, I. A., et al. 2018, ApJ, 156, 113

Bennett, D. P., Bhattacharya, A., Beaulieu, J.-P., et al. 2020, ApJ, 159, 68

Bensby, T., Yee, J., Feltzing, S., et al. 2013, A&A, 549, A147

Bertelli, G., Bressan, A., Chiosi, C., Fagotto, F., & Nasi, E. 1994, A&AS, 106, 275

Bertelli, G., Girardi, L., Marigo, P., & Nasi, E. 2008, A&A, 484, 815

Bertin, E., & Arnouts, S. 1996, A&AS, 117, 393

Bertin, E., & Emmanuel. 2010, Astrophysics Source Code Library, ascl:1010.068

Bessell, M. S. 1990, PASP, 102, 1181

Bessell, M. S., & Brett, J. M. 1988, PASP, 100, 1134

Bhattacharya, A., Bennett, D. P., Anderson, J., et al. 2017, ApJ, 154, 59

Bhattacharya, A., Beaulieu, J.-P., Bennett, D. P., et al. 2018, ApJ, 156, 289

Bhattacharya, A., Bennett, D. P., Beaulieu, J. P., et al. 2020, arXiv:2009.02329

Blackman, J. W., Beaulieu, J.-P., Cole, A. A., et al. 2020, ApJ, 890, 87

Bond, I. A., Udalski, A., Jaroszyski, M., et al. 2004, ApJ, 606, L155

Boss, A. P. 1997, Science, 276, 1836

Boyajian, T. S., Von Braun, K., Van Belle, G., et al. 2013, ApJ, 771, 40

Boyajian, T. S., Von Braun, K., Van Belle, G., et al. 2014, ApJ, 787, 92

Bressan, A., Marigo, P., Girardi, L., et al. 2012, MNRAS, 427, 127

Cameron, A. G. W. 1978, Earth Moon Planets, 18, 5

Cassan, A., Beaulieu, J. P., Fouqué, P., et al. 2006, A&A, 460, 277

Charbonneau, D., Brown, T. M., Latham, D. W., & Mayor, M. 2000, ApJ, 529, L45

Claret, A. 2000, A&A, 363, 1081

Currie, T., & Hansen, B. 2007, ApJ, 666, 1232

D'Angelo, G., Weidenschilling, S. J., Lissauer, J. J., & Bodenheimer, P. 2014, Icarus, 241, 298

De Jong, J. T. A., Kuijken, K. H., Crotts, A. P. S., et al. 2003, A&A, 417, 461

Dodson-Robinson, S. E., Veras, D., Ford, E. B., & Beichman, C. A. 2009, ApJ, 707, 79

Dong, S., Udalski, A., Gould, A., et al. 2007, ApJ, 664, 862

Dong, S., Gould, A., Udalski, A., et al. 2009, ApJ, 695, 970

Duncan, M. J., & Lissauer, J. J. 1998, Icarus, 134, 303

Einstein, A. 1936, Science, 84, 506

Farihi, J. 2016, New Astronomy Reviews, 71, 9

Fischer, D. A., & Valenti, J. 2005, ApJ, 622, 1102

Foreman-Mackey, D., Hogg, D. W., Lang, D., & Goodman, J. 2013, PASP, 125, 306

Fukui, A., Gould, A., Sumi, T., et al. 2015, ApJ, 809, 74

Gänsicke, B., Barstow, M., Bonsor, A., et al. 2019a, arXiv:1904.04839

Gänsicke, B. T., Schreiber, M. R., Toloza, O., et al. 2019b, Nature, 576, 61

Gaudi, B. S. 2010, arXiv:1002.0332

Gaudi, B. S. 2012, ARAAAJ, 50, 411

Gaudi, B. S., Bennett, D. P., Udalski, A., et al. 2008, Science, 319, 927

Ghezzi, L., Montet, B. T., & Johnson, J. A. 2018, ApJ, 860, 109

Giammichele, N., Bergeron, P., & Dufour, P. 2012, ApJS, 199, 29

Girardi, L., Bertelli, G., Bressan, A., et al. 2002, A&A, 391, 195

Gonzalez, O. A., Rejkuba, M., Zoccali, M., et al. 2012, A&A, 543, A13

Gould, A. 1994, ApJ, 421, L75

Gould, A., Udalski, A., An, D., et al. 2006, ApJ, 644, L37

Gould, A., Udalski, A., Monard, B., et al. 2009, ApJ, 698, L147

Gould, A. P., & Loeb. 1992, ApJ, 396, 104

Griest, K., & Safizadeh, N. 1998, ApJ, 500, 37

Han, C., Udalski, A., Choi, J.-Y., et al. 2013, ApJ, 762, L28

Ida, S., & Lin, D. N. C. 2004, ApJ, 616, 567

Janczak, J., Fukui, A., Dong, S., et al. 2010, ApJ, 711, 731

Jung, Y. K., Gould, A., Zang, W., et al. 2019, ApJ, 157, 72

Kennedy, G. M., & Kenyon, S. J. 2008, ApJ, 673, 502

Kerr, M., Johnston, S., Hobbs, G., & Shannon, R. M. 2015, ApJL, 809, L11

Kervella, P., Thevenin, F., Di Folco, E., & Segransan, D. 2004, A&A, 426, 297

Kim, S. L., Lee, C. U., Park, B. G., et al. 2016, J. Korean Astron. Soc., 49, 37

Koester, D., Gänsicke, B. T., & Farihi, J. 2014, A&A, 566, A34

Koshimoto, N., & Bennett, D. P. 2020, ApJ, 160, 177

Koshimoto, N., Bennett, D. P., & Suzuki, D. 2020, ApJ, 159, 268

Koshimoto, N., Udalski, A., Beaulieu, J. P., et al. 2016, ApJ, 153, 1

Koshimoto, N., Bennett, D. P., Penny, M. T., et al. 2017, ApJ, 154, 3

Kubas, D., Beaulieu, J. P., Bennett, D. P., et al. 2012, A&A, 540

Levenberg, K. 1944, QAM, 2, 164

Liebes, S. 1964, Physical Review, 133, B835

Lissauer, J. J. 1993, ARAAAJ, 31, 129

Lissauer, J. J. 1995, Icarus, 114, 217

Luhman, K. L., Burgasser, A. J., & Bochanski, J. J. 2011, ApJL, 730, 9

Manser, C. J., Gänsicke, B. T., Eggl, S., et al. 2019, Science, 364, 66

Mao, S., & Paczyński, B. 1991, ApJ, 374, L37

Marquardt, D. W. 1963, SIAM, 11, 431

Meyer, M. R., Amara, A., Reggiani, M., & Quanz, S. P. 2018, A&A, 612

Milne, E. A. 1921, MNRAS, 81, 361

Minniti, D., Lucas, P. W., Emerson, J. P., et al. 2010, New Astron, 15, 433

Miyake, N., Sumi, T., Dong, S., et al. 2011, ApJ, 728

Mordasini, C., Alibert, Y., Benz, W., & Naef, D. 2009, A&A, 501, 1161

Mróz, P., Han, C., Udalski, A., et al. 2017, ApJ, 153

Mróz, P., Udalski, A., Skowron, J., et al. 2019, AJSS, 244, 29

Muraki, Y., Han, C., Bennett, D. P., et al. 2011, ApJ, 741, 22

Mustill, A. J., & Villaver, E. 2012, ApJ, 761, 13

Mustill, A. J., Villaver, E., Veras, D., Gänsicke, B. T., & Bonsor, A. 2018, MNRAS, 476, 3939

Nataf, D. M., Gould, A., Fouqué, P., et al. 2013, ApJ, 769, 88

Nishiyama, S., Tamura, M., Hatano, H., et al. 2009, ApJ, 696, 1407

Nordhaus, J., & Spiegel, D. S. 2013, MNRAS, 432, 500

Paczyński, B. 1986, ApJ, 304, 5

Paczyński, B. 1996, ARAAAJ, 34, 419

Peale, S. J. 1998, ApJ, 509, 177

Pejcha, O., & Heyrovský, D. 2009, ApJ, 690, 1772

Penny, M. T., Henderson, C. B., & Clanton, C. 2016, ApJ, 830

Penny, M. T., Scott Gaudi, B., Kerins, E., et al. 2019, ApJS, 241, 3

Perryman, M. A. C. 2011, The Exoplanet Handbook

Poleski, R., Udalski, A., Bond, I. A., et al. 2017, A&A, 604, A103

Pollack, J. B., Hubickyj, O., Bodenheimer, P. H., et al. 1996, Icarus, 124, 62

Refsdal, S., & Bondi, H. 1964, MNRAS, 128, 295

Renn, J. 1997, Science, 275, 184

Rivera, E. J., Lissauer, J. J., Butler, R. P., et al. 2005, ApJ, 634, 625

Safronov, V. S. 1972, Evolution of the protoplanetary cloud and formation of the earth and planets.

Sako, T., Sekiguchi, T., Sasaki, M., et al. 2008, Exp. Astron., 22, 51

Santos, N. C., Israelian, G., & Mayor, M. 2004, A&A, 415, 1153

Schneider, P. 1992, Gravitational Lenses (Springer: Berlin/Heidelberg, Germany)

Shaver, P. A., McGee, R. X., Newton, L. M., Danks, A. C., & Pottasch, S. R. 1983, MNRAS, 204, 53

Shin, I. G., Ryu, Y. H., Udalski, A., et al. 2016, J. Korean Astron Soc, 49, 73

Sigurdsson, S., Richer, H. B., Hansen, B. M., Stairs, I. H., & Thorsett, S. E. 2003, Science, 301, 193

Skowron, J., Udalski, A., Gould, A., et al. 2011, ApJ, 738, 1

Southworth, J. 2015, Astrophysics Source Code Library, ascl:1511.016

Spergel, D., Gehrels, N., Baltay, C., et al. 2015, arXiv:1503.03757

Stanek, K. Z., & Garnavich, P. M. 1998, ApJ, 503, 131

Stetson, P. B. 1987, PASP, 99, 191

Storn, R., & Price, K. 1997, J Global Optim, 11, 341

Sumi, T., Bennett, D. P., Bond, I. A., et al. 2010, ApJ, 710, 1641

Sumi, T., Kamiya, K., Bennett, D. P., et al. 2011, Nature, 473, 349

Sumi, T., Bennett, D. P., Bond, I. A., et al. 2013, ApJ, 778, 150

Sumi, T., Udalski, A., Bennett, D. P., et al. 2016, ApJ, 825, 112

Suzuki, D., Bennett, D. P., Sumi, T., et al. 2016, ApJ, 833, 145

Suzuki, D., Bennett, D. P., Ida, S., et al. 2018, ApJ, 869, L34

Swain, M. R., Vasisht, G., & Tinetti, G. 2008, Nature, 452, 329

Terry, S. K., Bhattacharya, A., Bennett, D. P., et al. 2020, arXiv:2009.08461

Tinetti, G., Deroo, P., Swain, M. R., et al. 2010, ApJL, 712, 139

Tisserand, Guillou, L., Afonso, et al. 2007, A&A, 469, 387

Toonen, S., Hollands, M., Gänsicke, B. T., & Boekholt, T. 2017, A&A, 602, 16

Tsapras, Y. 2018, Geosci, 8, 365

Udalski, A. 2003, Acta Astronomica, 53, 291

Udalski, A., Szymanski, M., Kaluzny, J., et al. 1994, Acta Astronomica, 44, 227

Udalski, A., Jaroszyński, M., Paczyński, B., et al. 2005, ApJ, 628, L109

Udalski, A., Jung, Y. K., Han, C., et al. 2015, ApJ, 812, 47

Udalski, A., Ryu, Y. H., Sajadian, S., et al. 2018, Acta Astronomica, 68, 1

Uglesich, R. R., Crotts, A. P. S., Baltz, E. A., et al. 2004, ApJ, 612, 877

Vanderburg, A., Johnson, J. A., Rappaport, S., et al. 2015, Nature, 526, 546

Vandorou, A., Bennett, D. P., Beaulieu, J.-P., et al. 2020, ApJ, 160, 121

Veras, D. 2016, Royal Society Open Science, 3, 150571

Villaver, E., & Livio, M. 2007, ApJ, 661, 1192

Wada, K., Tsukamoto, Y., & Kokubo, E. 2019, ApJ, 886, 107

Witt, H. 1990, A&A, 236, 311

Wolszczan, A., & Frail, D. A. 1992, Nature, 355, 145

Xu, S., Ertel, S., Wahhaj, Z., et al. 2015, A&A, 579, 8

Yee, J. C., Suzuki, D., Abe, F., et al. 2012, ApJ, 755

Yee, J. C., Han, C., Gould, A., et al. 2014, ApJ, 790, 14

Yoo, J., DePoy, D. L., Gal-Yam, A., et al. 2004, ApJ, 603, 139

Zuckerman, B., Melis, C., Klein, B., Koester, D., & Jura, M. 2010, ApJ, 722, 725

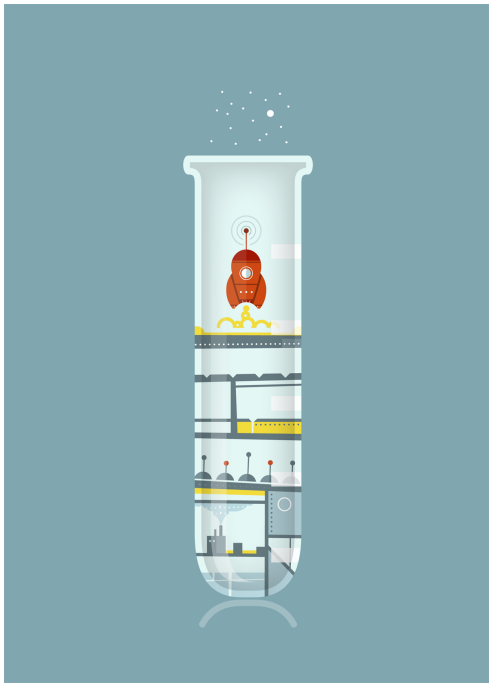

This thesis was typeset using LaTeX, originally developed by Leslie Lamport and based on Donald Knuth's TeX. A template similar to this can be used to format a PhD dissertation with this look & feel has been released under the permissive AGPL license, and can be found online at github.com/suchow/Dissertate or from its lead author, Jordan Suchow, at suchow@post.harvard.edu.